ISPC Conference

Statistics


ISPC24
24TH INTERNATIONAL SYMPOSIUM ON PLASMA CHEMISTRY
NAPLES (ITALY) JUNE 9-14, 2019


Naples
ISPC 24

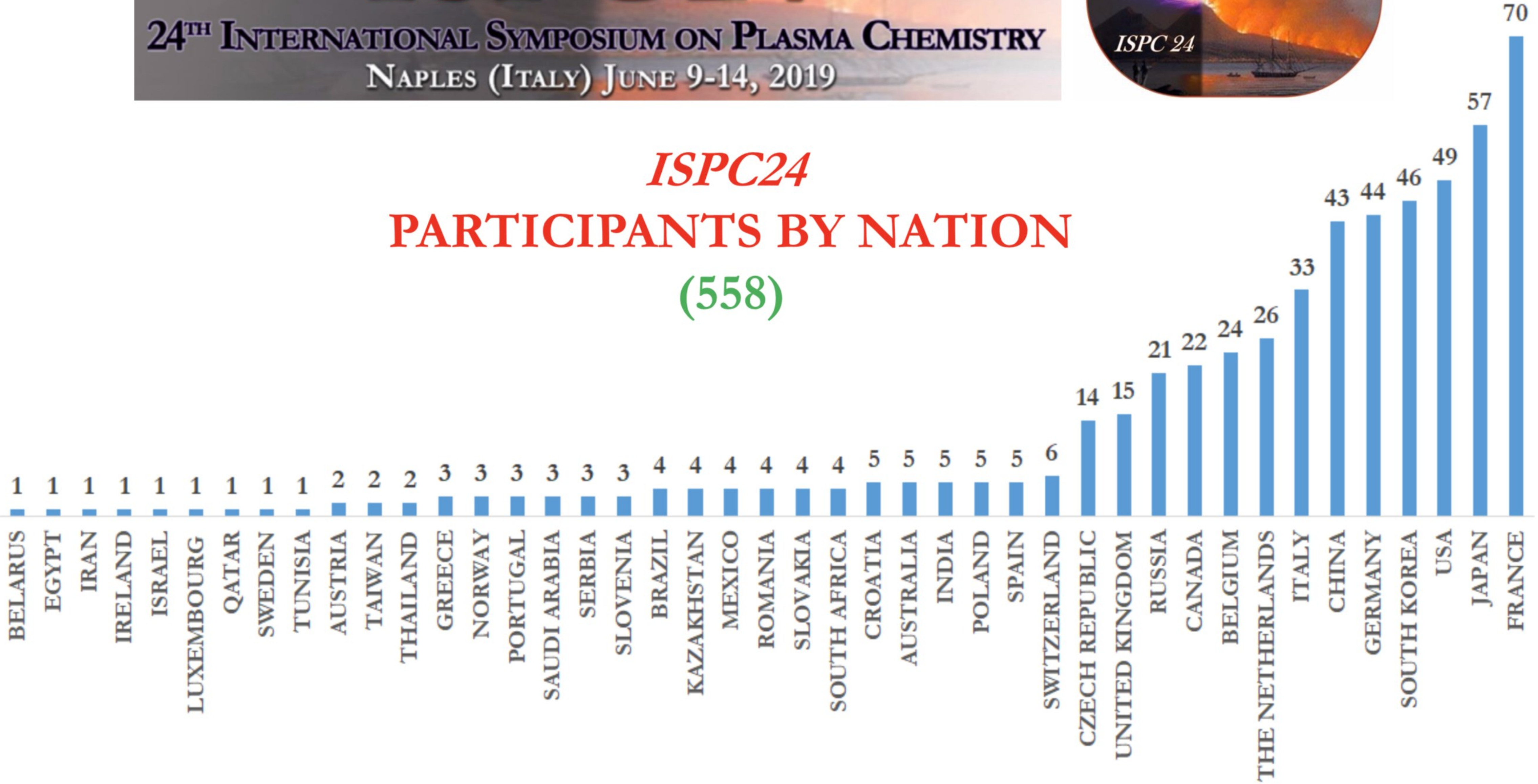
ISPC24
PARTICIPANTS BY NATION
(558)
BELARUS 1
EGYPT 1
IRAN 1
IRELAND 1
ISRAEL 1
LUXEMBOURG 1
QATAR 1
SWEDEN 1
TUNISIA 1
AUSTRIA 2
TAIWAN 2
THAILAND 2
GREECE 3
NORWAY 3
PORTUGAL 3
SAUDI ARABIA 3
SERBIA 3
SLOVENIA 3
BRAZIL 4
KAZAKHSTAN 4
MEXICO 4
ROMANIA 4
SLOVAKIA 4
SOUTH AFRICA 4
CROATIA 5
AUSTRALIA 5
INDIA 5
POLAND 5
SPAIN 5
SWITZERLAND 6
CZECH REPUBLIC 14
UNITED KINGDOM 15
RUSSIA 21
CANADA 22
BELGIUM 24
THE NETHERLANDS 26
ITALY 33
CHINA 43
GERMANY 44
SOUTH KOREA 46
USA 49
JAPAN 57
FRANCE 70

ISPC24

24TH INTERNATIONAL SYMPOSIUM ON PLASMA CHEMISTRY

NAPLES (ITALY) JUNE 9-14, 2019

Naples

ISPC 24

ISPC24
ABSTRACTS BY NATION
(558)

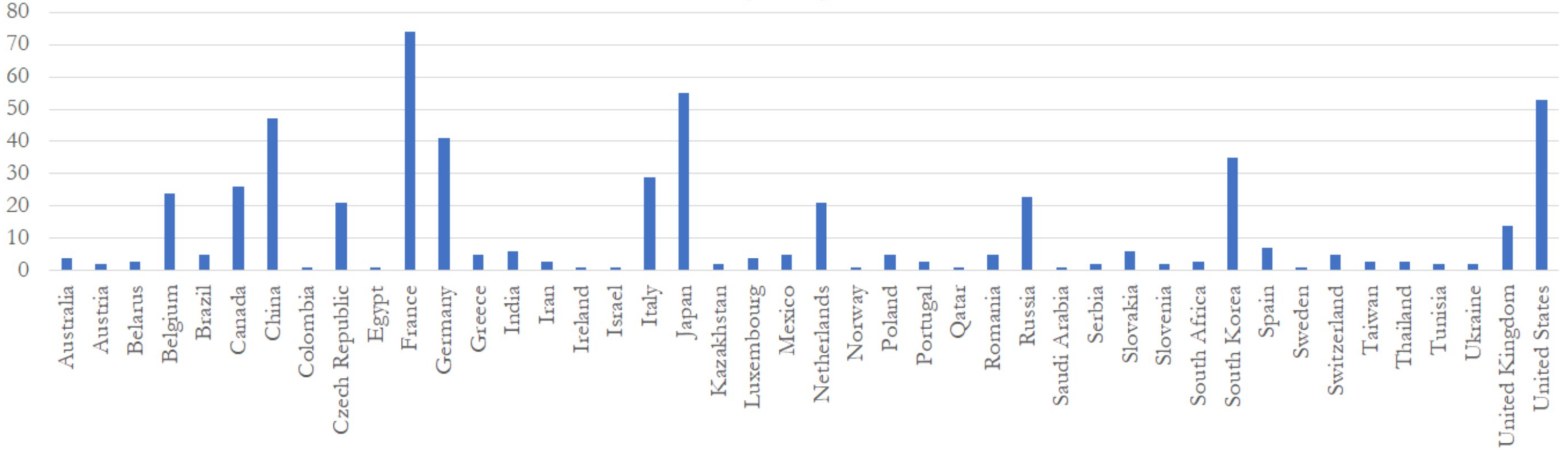

Statistics

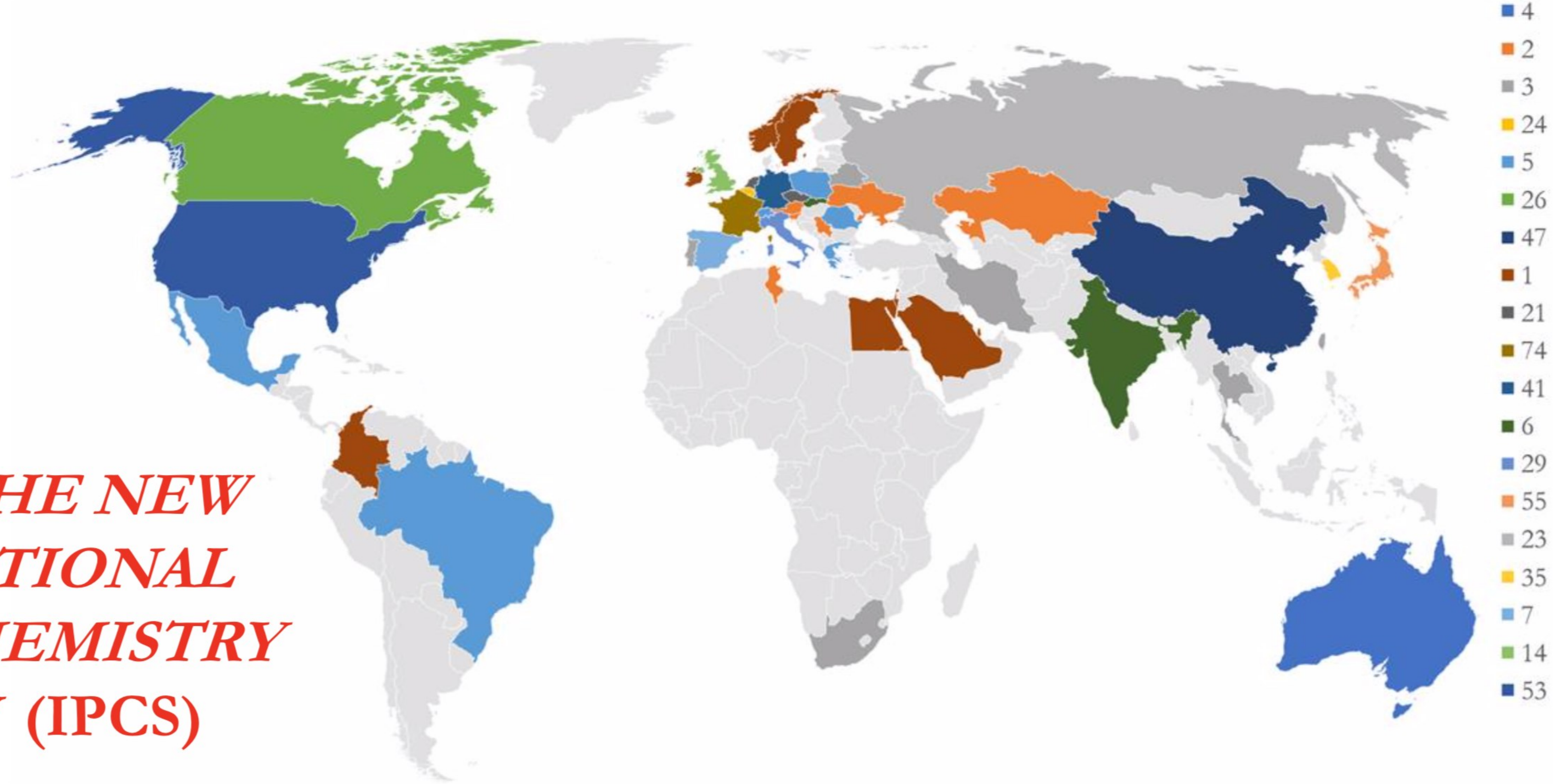

***<u>WE</u> ARE THE NEW INTERNATIONAL PLASMA CHEMISTRY SOCIETY* (IPCS)**

Statistics

27 IOC PEER- REVIEWERS

(1) Fundamentals, diagnostics and modelling in plasma chemistry

(2) Plasma sources design and characterization

(3) Plasma processing of nanomaterials and nanostructures: synthesis, modification and nanofabrication

(4) Plasma deposition of functional coatings and treatment of inorganic and organic materials

(5) Thermal plasma fundamentals and applications

(6) Plasma-assisted conversion, combustion, propulsion and aerodynamics

(7) Plasma medicine and plasma agriculture

(8) Plasma treatment of biomaterials

(9) Plasma in and in contact with liquids

(10) Plasmas for environmental applications and resource recovery

Abstract Assignation (Show Details)

Abstracts	Assigned	Unassigned
558	382	176

Referee Review (Show Details)

Assignations	Completed	In progress	To do
1145	1145	0	0

- Committee Dashboard -

		1	2	3	4	5	6	7	8	9	10
		1	1	0	0	2	0	0	0	2	0
		16	8	14	8	6	9	8	3	7	11
		20	7	28	10	23	11	32	4	3	11
		69	35	26	44	7	31	45	9	20	17
		0	0	1	2	1	2	0	0	0	0
		0	0	0	1	1	1	0	1	0	0
TOTALS	**558**	**106**	**51**	**69**	**65**	**40**	**54**	**85**	**17**	**32**	**39**

Metal vapour transport in tungsten-inert-gas welding
A.B. Murphy

Importance de la diffusion des vapeurs métalliques - TIG

Dans les applications TIG : les vapeurs métalliques viennent du weld pool - Electrodes en tungsten

Modèle: TIG dans Helium + vapeurs Fe / Cr

- Equations du modèle, utilisation des coefficients de diffusion combinés étendus à des mélanges ternaires
- But du modèle : montrer que la diffusion joue un rôle important

Résultats : Bon accord entre calculs et mesures radialement (basé sur l'émission des raies Cr à 520.8nm)
Sans vapeurs T_{max}=21000K, avec vapeurs T_{max}=13000K, **la diffusion sous effet du champ électrique** est un processus dominant (for upward transport of metal vapor). On observe des vapeurs Cr proche de la cathode, déposées dans des régions où $T>T_{boil}$

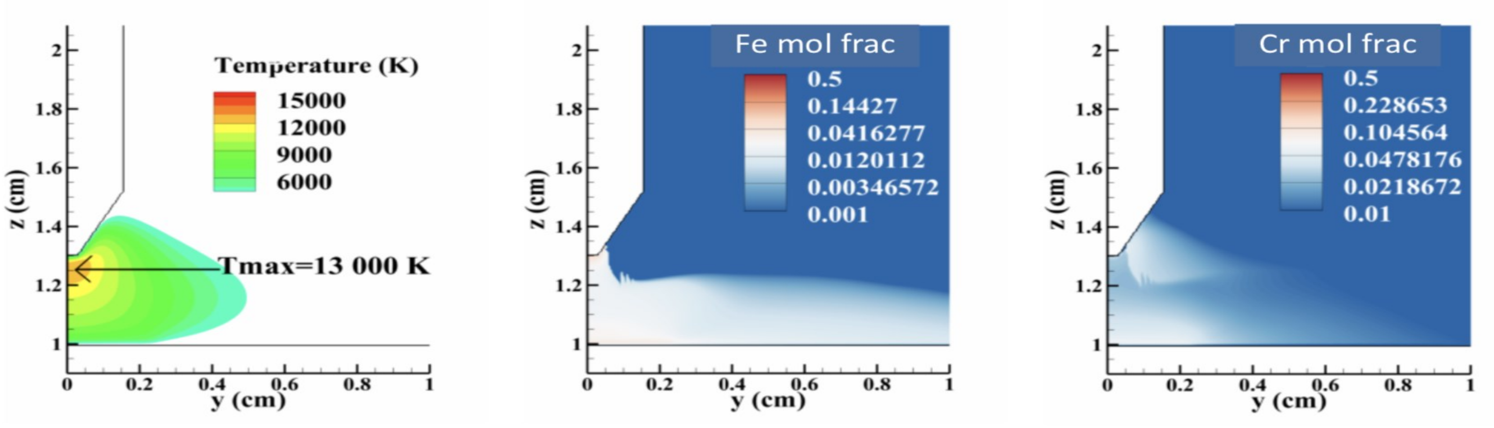

(a) (b) (c)

Fig. 4. Distributions of (a) temperature, (b) iron vapour mole fraction and (c) chromium vapour mole fraction in helium TIG welding of stainless steel.

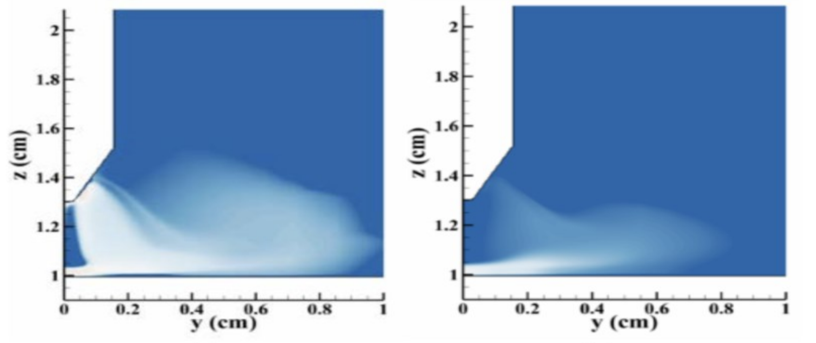

(a) (b)

Fig. 2. Distributions of chromium vapour mole fraction neglecting (a) diffusion driven by electric fields and (b) diffusion driven by temperature gradients. The mole fraction scale is the same as in Fig. 1(c).

Metal vapour transport in tungsten-inert-gas welding

A.B. Murphy

Modèle: TIG dans Argon + vapeurs Fe / Cr

- Comparaison faite avec et sans diffusion sous Champ Electrique, avec et sans diffusion sous gradient T

Résultats:

- **La diffusion à cause des gradients de températures** est dominant (pas par E), plus forte à basses T pour Ar-Fe-Cr que He-Fe-Cr, les coefficients de diffusion combinés sont plus faibles pour Ar-Fe-Cr que He-Fe-Cr
- Les vapeurs métalliques sont produites à l'anode, puis diffusion upwards to recirculating flow, et trapped near cathode tip by upward diffusion -> importance de la convection

Validation par mesures expérimentales : OES montre la présence de Cr proche cathode

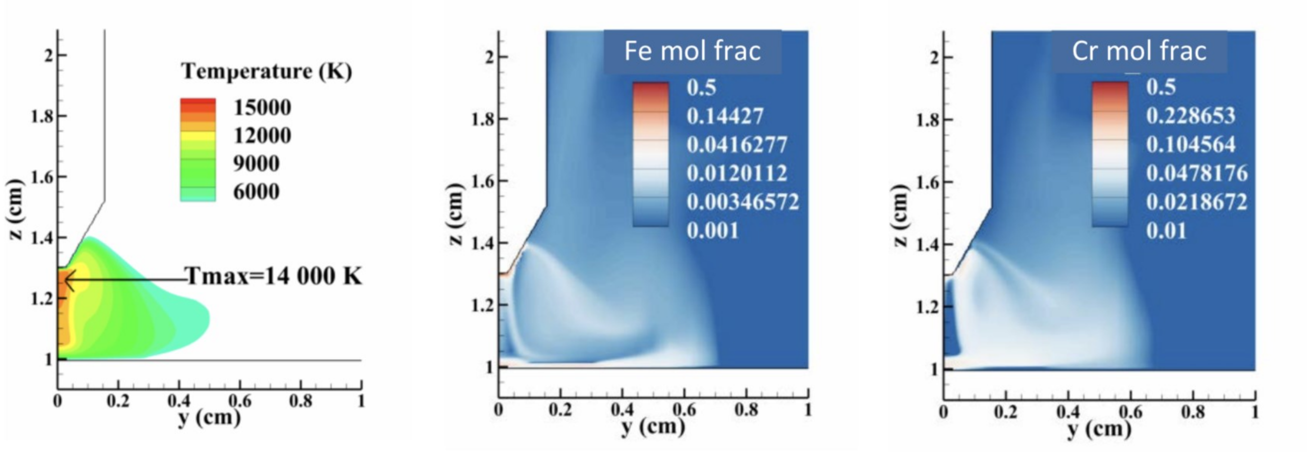

(a) (b) (c)

Fig. 1. Distributions of (a) temperature, (b) iron vapour mole fraction, (c) chromium vapour mole fraction in argon TIG welding of stainless steel.

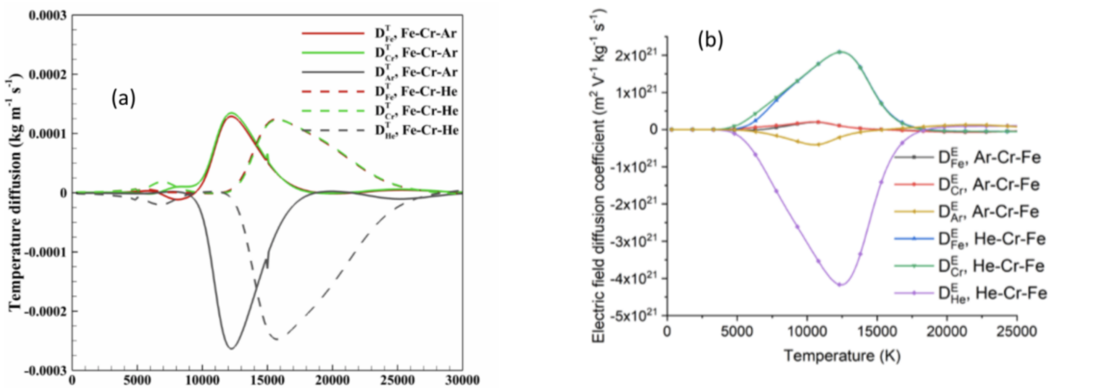

Fig. 3. Combined (a) temperature and (b) electric field diffusion coefficients for mixtures of 10% wt% iron and 10 wt% chromium with argon or helium.

Validated modeling of atmospheric pressure – anodic arc
I. Kaganovich

Développement d'un modèle pour la synthèse de CNT par arc dans C-He plasmas
-> déterminer les profils de champ électrique, densité d'électron, température électronique proche anode
-> avec mode « faible » ablation

Modèle :
2D-3D modèle - Ansys CFX - Non equilibrium plasmas, Patm, Self consistent model, P=500 torr
Plasma current, emission current, ion current, sheath voltage drop, heat fluxes at plasma-electrode interfaces
Momemtum + continuity + neutral transport + ions transport + electron transport equations
Validation for 1D short nonuniform arc (arc core, near-cathode-anode regions, voltage drop, ion current)

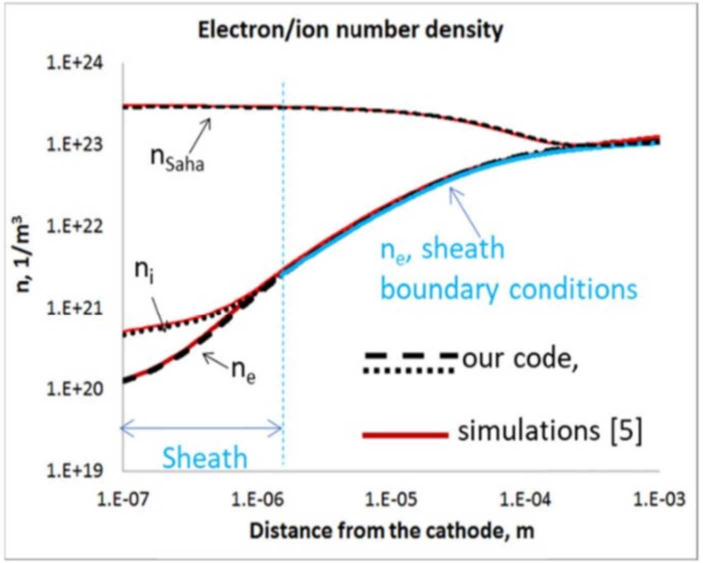

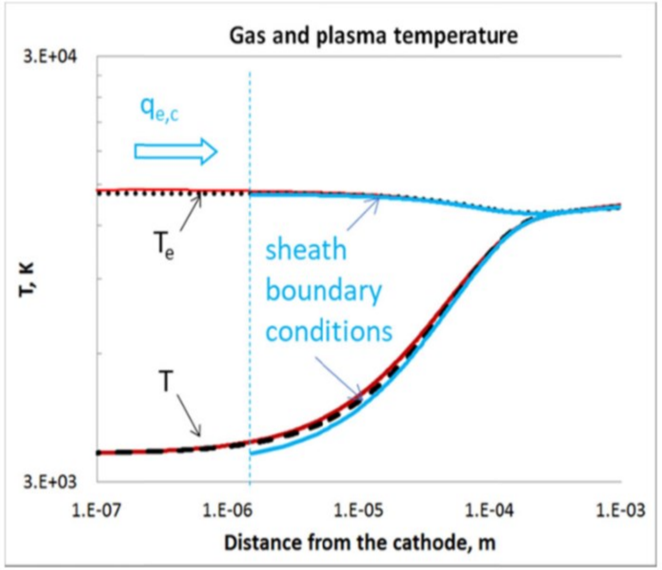

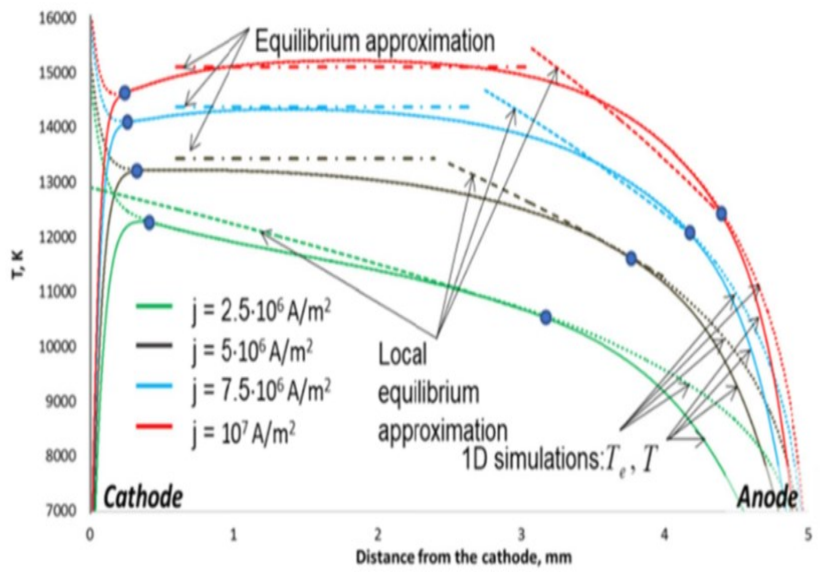

Validated modeling of atmospheric pressure – anodic arc

I. Kaganovich

2D simulations

2D- axisimmetric and steady-state

Navier-Stokes equations + heat transfer + current flow in solid electrodes (ablation anode et déposition cathode) + near-electrode space-charge sheathes + wall function (plasma-electrode interfaces) + radiation from electrodes surfaces, Joule heating of electrodes, and the thermal resistance of the deposit at the cathode.

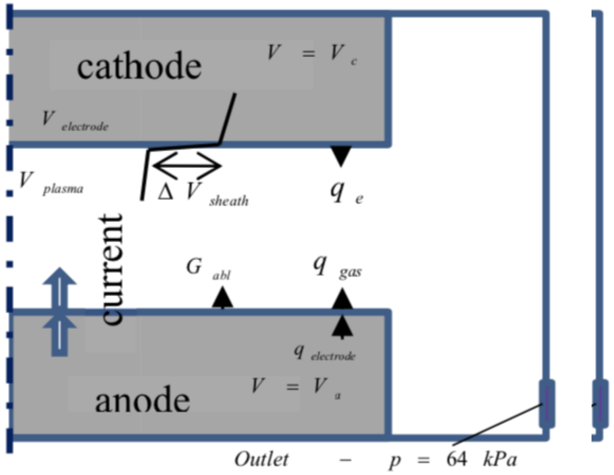

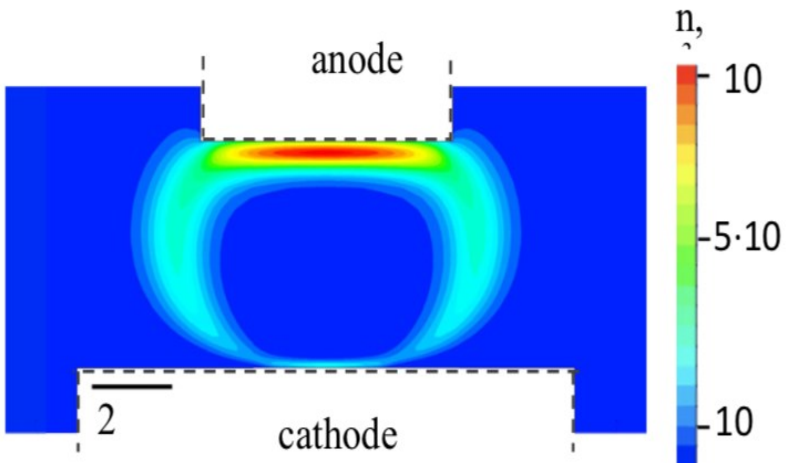

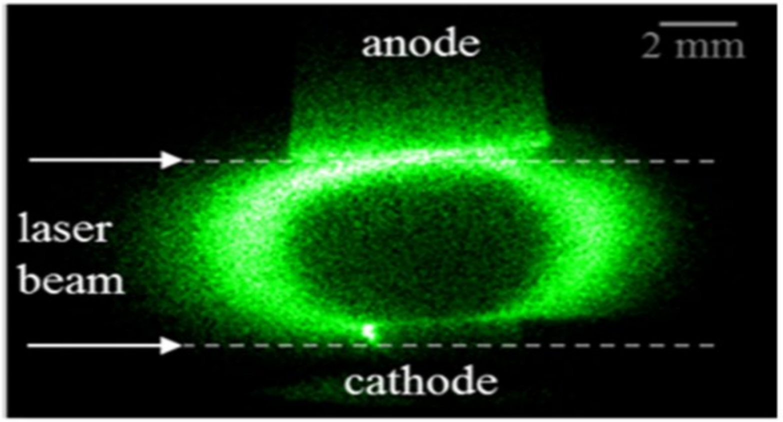

Carbon dimer distribution has a bubble-like shape around the arc core. Comparison of (top) simulated and (bottom) measured C_2 density distribution (planar LIF: spectral image of carbon dimer, emission is at 470 nm and laser radiation is at 437 nm) in the arc at current 50 A

En mode « faible » ablation, courant d'arc à l'anode est drivé par diffusion électronique (V_{anode} faible-> flux chaleur faible)

Les profils de densité de courant sont affecté par la gaine pour de faibles gap : 1.5mm

Les profils de densité de courant sont plus uniformes pour de larges gap : 3mm

Les molécules de carbone se forment dans les région froides, périphériques du plasma

Fluctuation phenomena in diode-rectified multiphase AC arc for improvement of electrode erosion

M. Tanaka

Inconvénients : arc instable et non uniforme dans l'espace et le temps, forte érosion des électrodes

Constat : à la cathode on veut Low work function et high melting point, à l'anode high thermal conductivity.
Aucun matériau ne satisfait à la fois les propriétés requises pour cathode et anode : le plus gros problème=> forte érosion en AC des électrodes.

Intérêt de la Diode Rectification (DR) : séparer l'électrode en une paire de cathode et anode, et permettre ainsi de mieux visualiser efficacement les fluctuations

Objectif : comprendre et caractériser l'impact de la DR spatialement et temporellement par caméra rapide, observation du profile de température pour un MultiPhase-Arc (MPA)

Conclusion : l'érosion est mieux caractérisée avec DRMPA

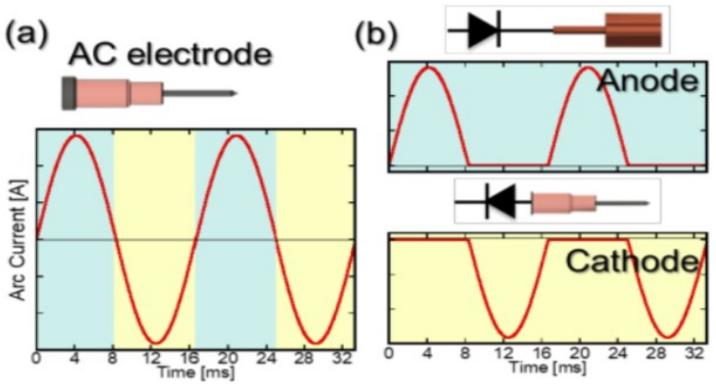

3. Conceptual waveforms of arc current for MPA (a) and DRMPA electrode (b).

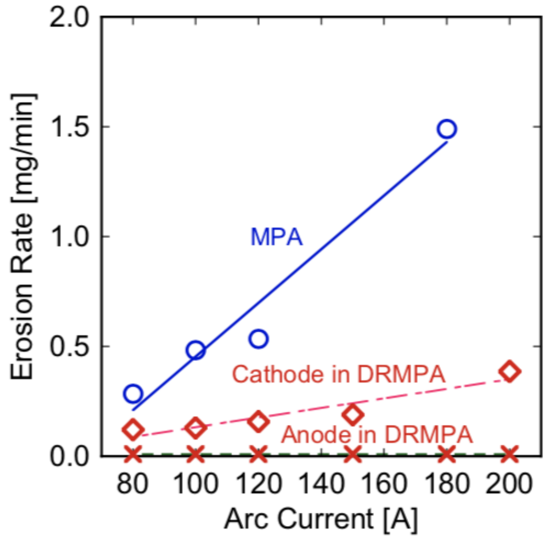

Fluctuation phenomena in diode-rectified multiphase AC arc for improvement of electrode erosion
M. Tanaka

Dispositif expérimental:
Patm, 6 phases, Argon, 100-150A, gap électrode 50mm, cathode $WThO_2$ (3.2mm diam), anode Cu (25mm diam)
Mesures par Camera rapide FASTCAM SA5.
Etude des raies atomiques (O, Ar, W) par OES -> distribution de la température, radiale et temporelle
Comparaison des observations faites MPA et DRMPA à 120A sur les raies à 794nm et 675nm

Arc temperature fluctuation

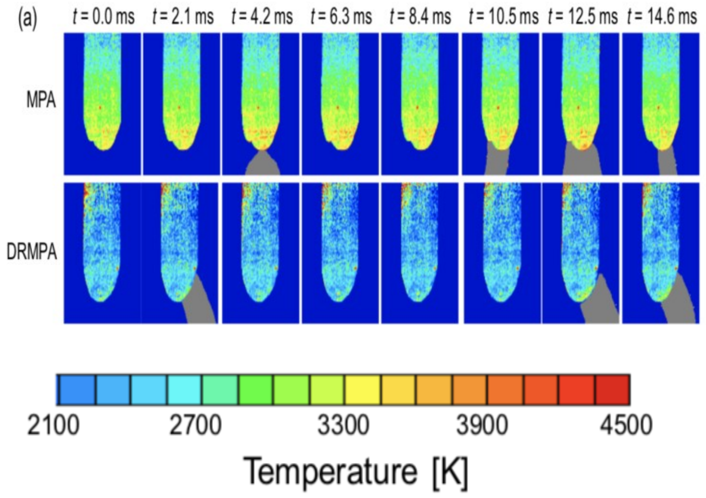

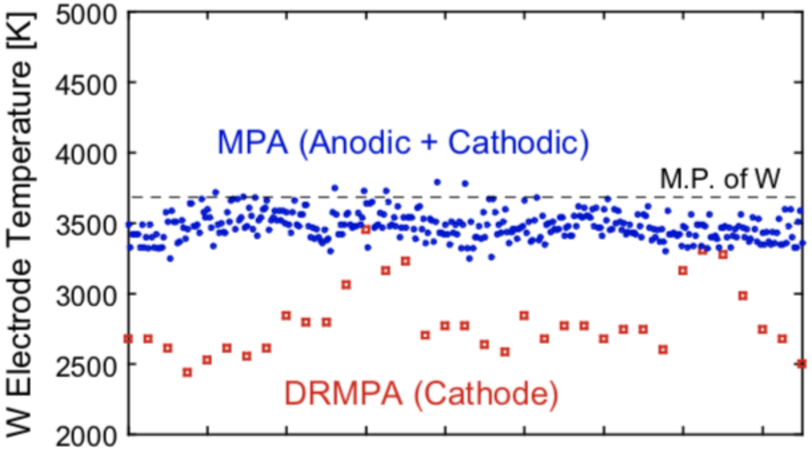

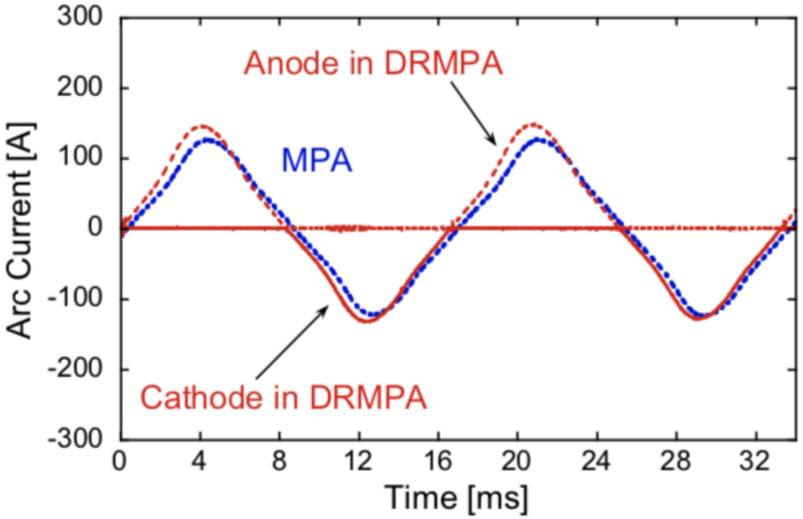

Fluctuation phenomena in diode-rectified multiphase AC arc for improvement of electrode erosion

M. Tanaka

Résultats :

Analyse à la cathode : T=13000K (MPA et DRMPA) - Diamètre : 5mm cathode (9.106A/m^2 pour les 2 méthodes),
Analyse à l’anode : T=9000K (DRMPA)-11000K(MPA) - Diamètre : 7mm+7mm (DRMPA 2 arcs présents, 2.106A/m^2) contre 7mm (1 arc en MPA 4.106A/m^2)

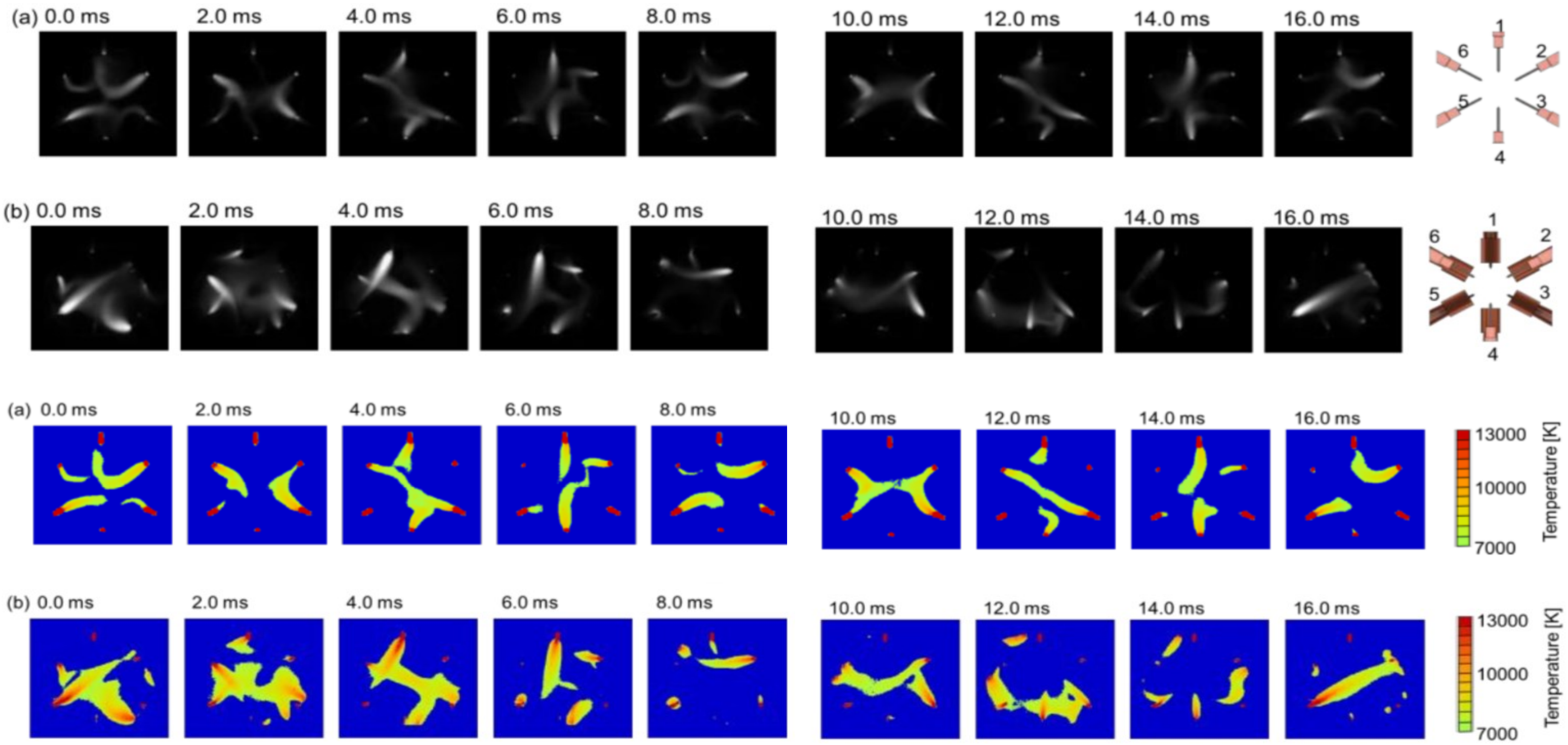

Fluctuation phenomena in diode-rectified multiphase AC arc for improvement of electrode erosion

M. Tanaka

Conclusions :

Cathode jet >> anode jet pour DRMPA

Cathode jet = Anode jet pour MPA

Le profil de température à la cathode est plus important qu'à l'anode

Différences aux électrodes est due à la présence de vapeurs métalliques, anode shape effet

Différences aux électrodes du jet de plasma en configuration DRMPA et MPA ont été analysées et clarifiées

Un courant plus fort conduit à plus d'uniformité de l'arc

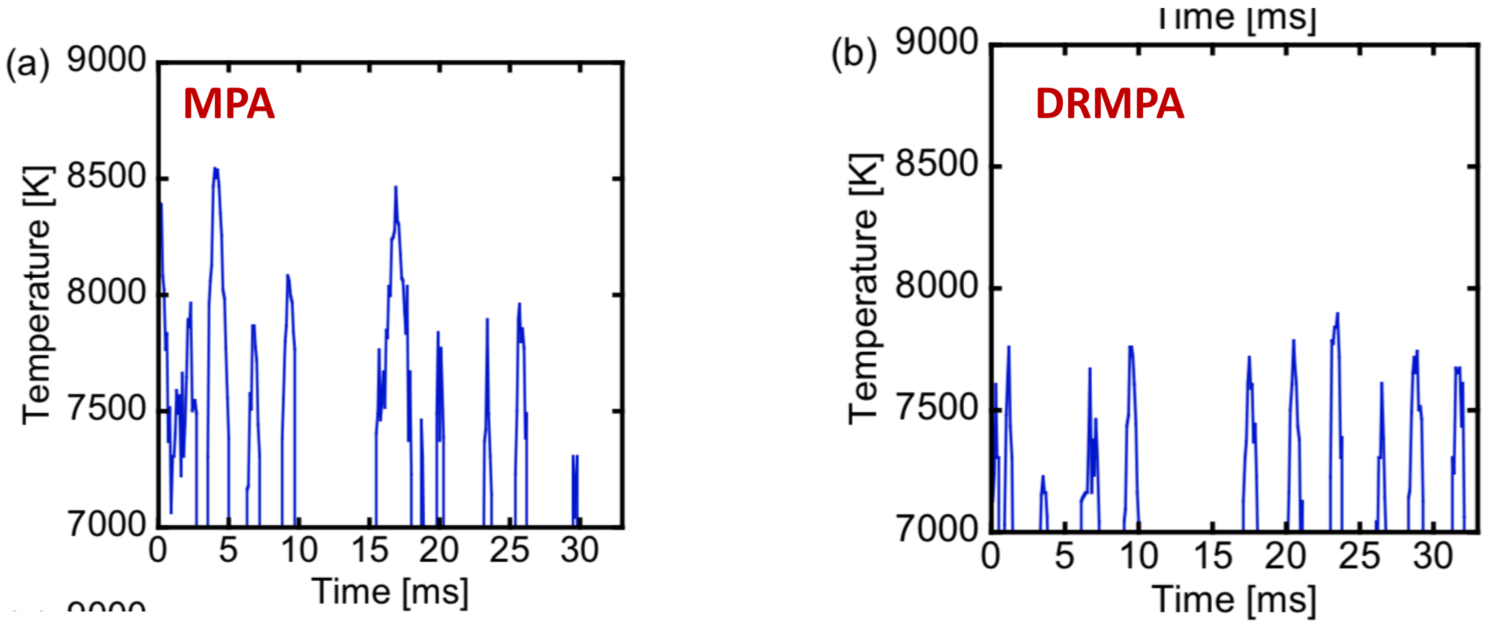

Temperature fluctuation at the centre of the discharge region for the MPA (a) and the DRMPA (b)

Complementary studies of DC arc by experiments and combined modelling of the plasma bulk and the cathode boundary layer

C. Mohsni

Motivation

- Meilleure description des phénomènes aux électrodes
- Comparaison modèle – mesures Air, CO2 gaz.

Dispositif expérimental

- Anode sphérique en graphite, cathode W, gap 5mm
- Mesures électriques (V et I) + Mesures OES (profil de température) at midplane of the arc

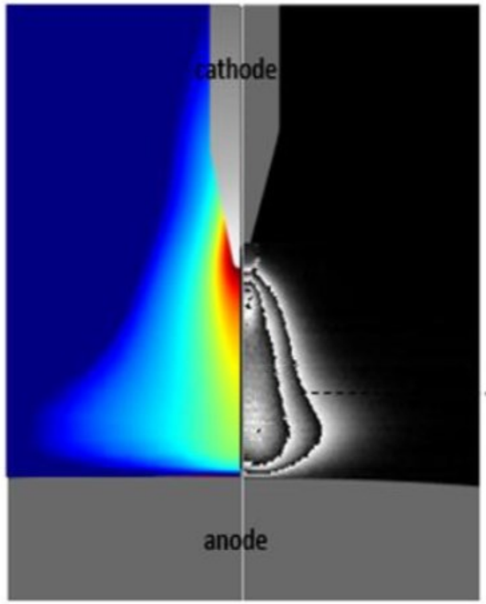

Modèle

Colonne d'arc LTE + nonequilibrium cathode boundary -> couplage

Cathode boundary layer : basé sur travaux de Benilov

Heat transfer+current transfer+boundary conditions+iterations till: on obtient J et T à la surface, couplé au reste du model

Complementary studies of DC arc by experiments and combined modelling of the plasma bulk and the cathode boundary layer

C. Mohsni

Resultats:

Densité de courant et chute de potentiel en fonction de la température de surface

Différents flux et température électronique en fonction de

Température en fonction de la distance à la surface de la cathode (0-12mm) : basé sur travaux de Baeva.

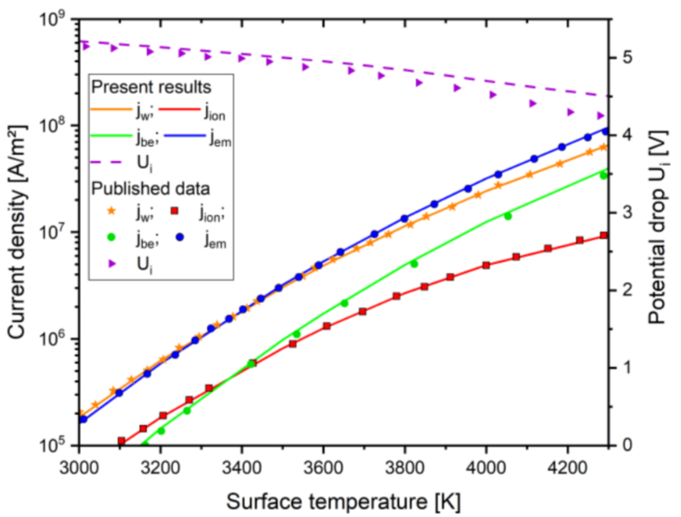

Fig. 2. Total current density and its components in the cathode space-charge sheath for U_{tot} = 10 V.

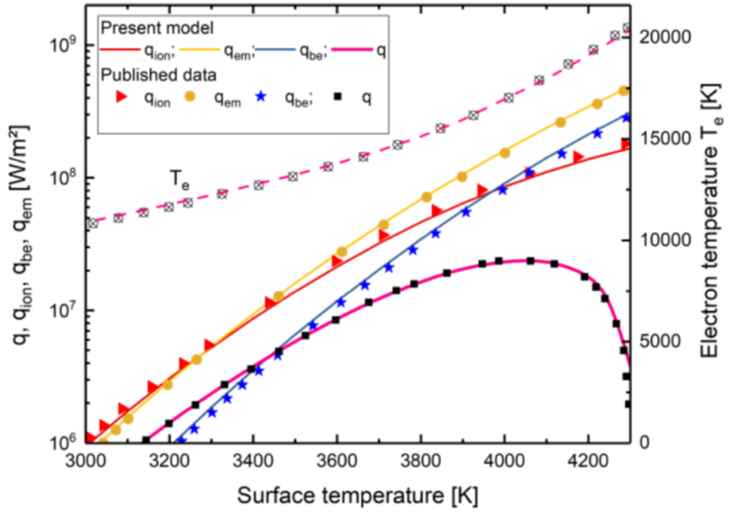

Fig. 3. Total heat flux from the plasma to the cathode surface and its components for U_{tot} = 10 V.

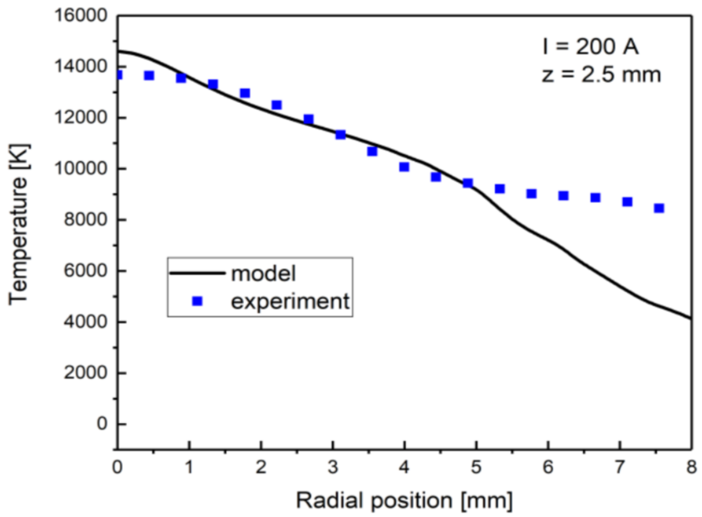

Fig. 4. Radial distribution of the plasma temperature in the midplane of the arc obtained in the combined modelling approach and OES for an arc current 200 A.

Complementary studies of DC arc by experiments and combined modelling of the plasma bulk and the cathode boundary layer
C. Mohsni

Combined arc model results

I=200A, profil de température, U_{arc}=16.56V (mesuré 17.54V)
à z=2.5mm, « fair » accord jusqu'à 5mm en position radial
Comparaison entre model à LTE et combined model : températures quasi pareilles, mais champ électrique différent
Accord acceptable sur la tension d'arc

Projet : appliquer le model combiné au CO_2

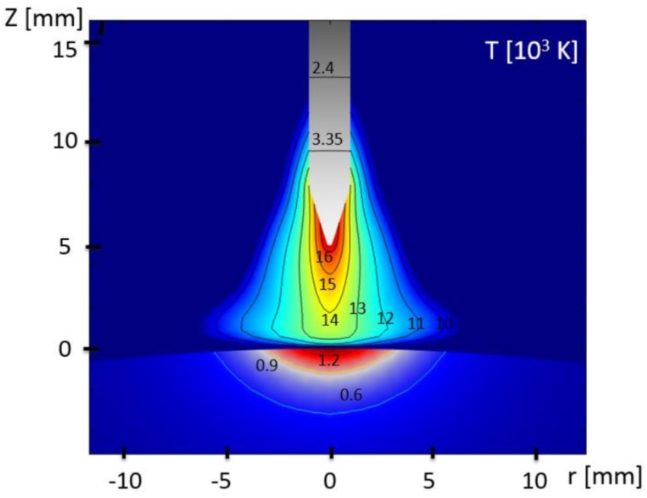

Fig. 5. Two-dimensional distribution of the plasma temperature and the temperature in the electrodes obtained in the combined modelling approach for arc current 200 A.

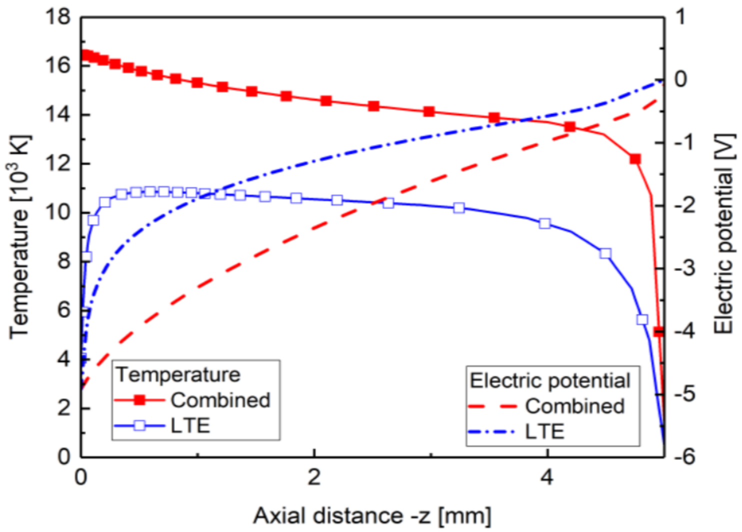

Fig. 6. Plasma temperature and electric potential in the plasma along the arc axis for an arc current of 200 A.

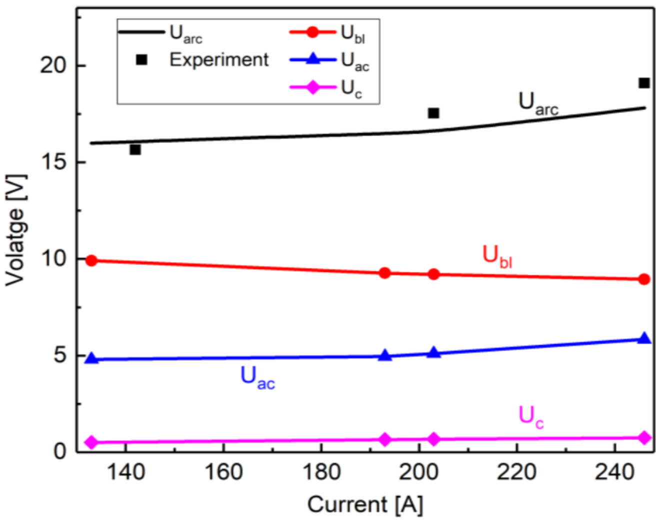

Fig. 7. The current-voltage characteristics of the arc obtained by the combined modelling approach and electric measurements. Additionally, the individual contributions of the boundary layer (U_{bl}), the voltage drop in the cathode (U_c) and the arc column (U_{ac}) are shown.

CO2 plasmas : from solar fuels to oxygen production on Mars
V. Guerra

Constats : augmentation des émission de CO_2, réchauffement climatique
Solutions : produire du CO_2 « neutre », utiliser le CO_2 pour produire des gaz de synthèse $CO+H_2$, electrolysis vs plasmalysis

Motivation:
- L'activation du CO_2 par plasma - CO_2 dissociation peut être améliorée par l'excitation vibrationnelle
- Comprendre la relaxation du CO_2 -> Self consistent model kinetic model+experiment support (LPP/TU/e)
- Application ISRU (In Situ Resource Utilisation) Mars ($96\%CO_2+2\%Ar+2\%N_2$, basses T et basses P=5Torr,
V-T coefficients plus faibles, V-V plus importants)

CO_2 molécules : 3 modes de vibration : symmetric, bending, asymmetric
- Electron impact, vibration-to-vibration, vibration-to-vibration energy exchanges

Kinetic model :
- Niveaux hauts vibrationnels négligeables, rôle négligeable de la dissociation et produits issus de la dissociation
- 70 niveaux de vibration, équation Boltzmann pour les électrons couplée système équations taux réaction, E/N constant
- 250 direct réactions (e-V), 450 pour V-T, et 800 pour V-V

Manipulation
DC pulsée et continue, 1-5torr, 10-50mA, T_{gaz}=230K, Δt=5ms, diagnostique par FTIR
CO_2 pur : influence de $T_{g.}$ Temperature room : influence de Ar/N_2

CO2 plasmas : from solar fuels to oxygen production on Mars
V. Guerra

<u>Résultats :</u>

- Validation plutôt bonne du calcul des densités des niveaux vibrationnels (e-V, V-T et V-V) mais quelques différences pour la température

-> ajout d'une équation : $n_m C_p dT_g/dt = Q_{in} - 8\lambda(T_g - T_w)/R^2$

-> ajout des niveaux jusqu'à $\nu_3=21$

-> la section efficace de dissociation par impact électronique est mal connue

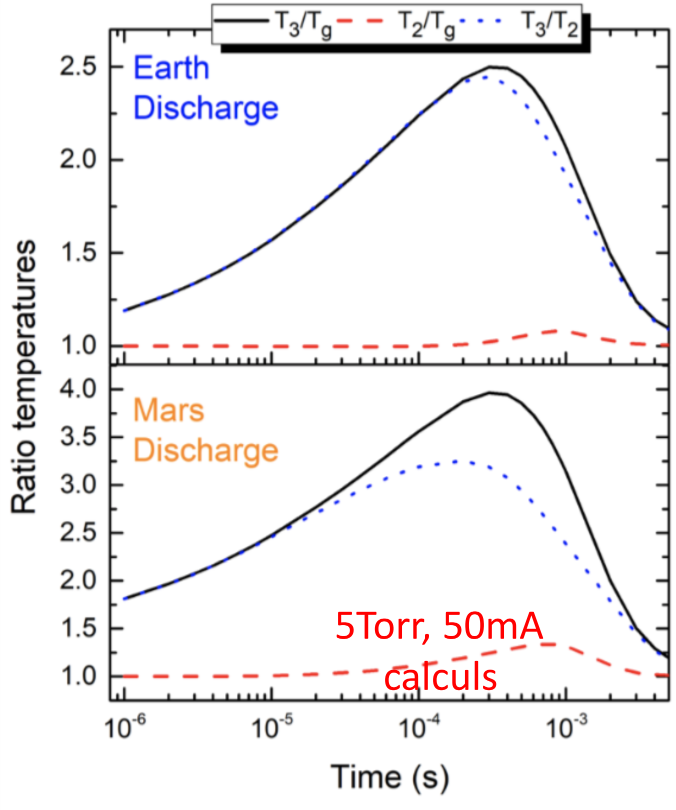

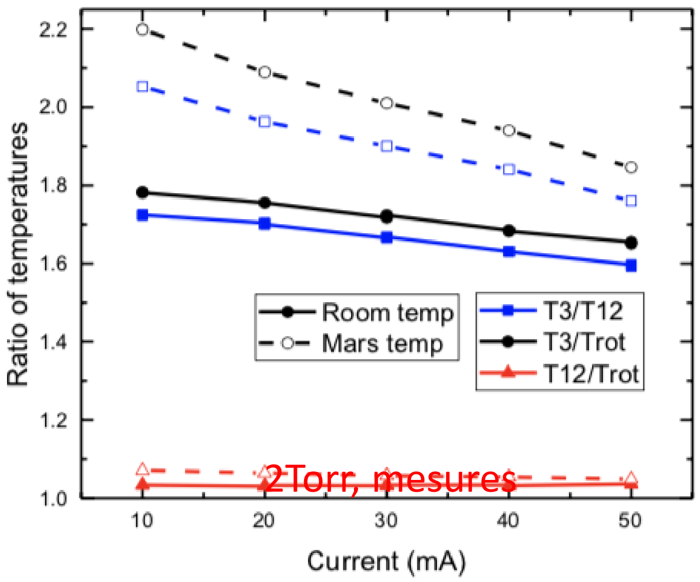

a = [CO] / ([CO]+[CO₂])

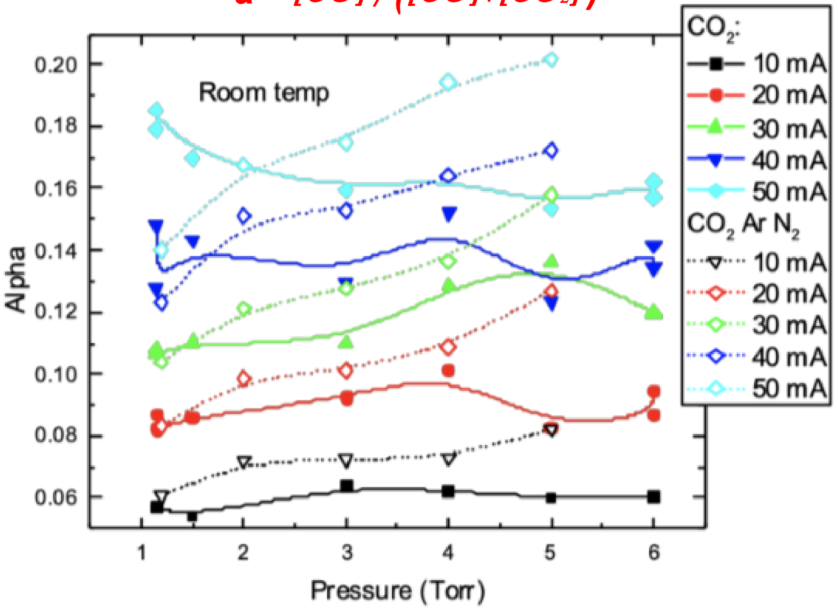

Plus fort déséquilibre sur Mars -> favorise dissociation vibrationnelle
Facteur 1.2 (mesures), et 1.6 (calculs) du déséquilibre (Terre vers Mars)
Effet positif de la composition de Mars sur la dissociation (facteur conversion $\alpha(CO_2+Ar+N_2)$)

Plasma treatment of biomedical waste

A. Ustimenko

Thermodynamic analysis and experiments on gasification of biomedical waste (BMW)

Constituants le plus souvent constatés : C, H, O, N, S, P, $CaCO_3$

Espèces carbonées solides : TERRA thermodynamic code

300-3000K, 0.1MPa, cas 1 (dry 10kgBMW+5kg air) ou cas 2 (wet 10kgBMW+1kg air + 0.5 steam)

Cas 1

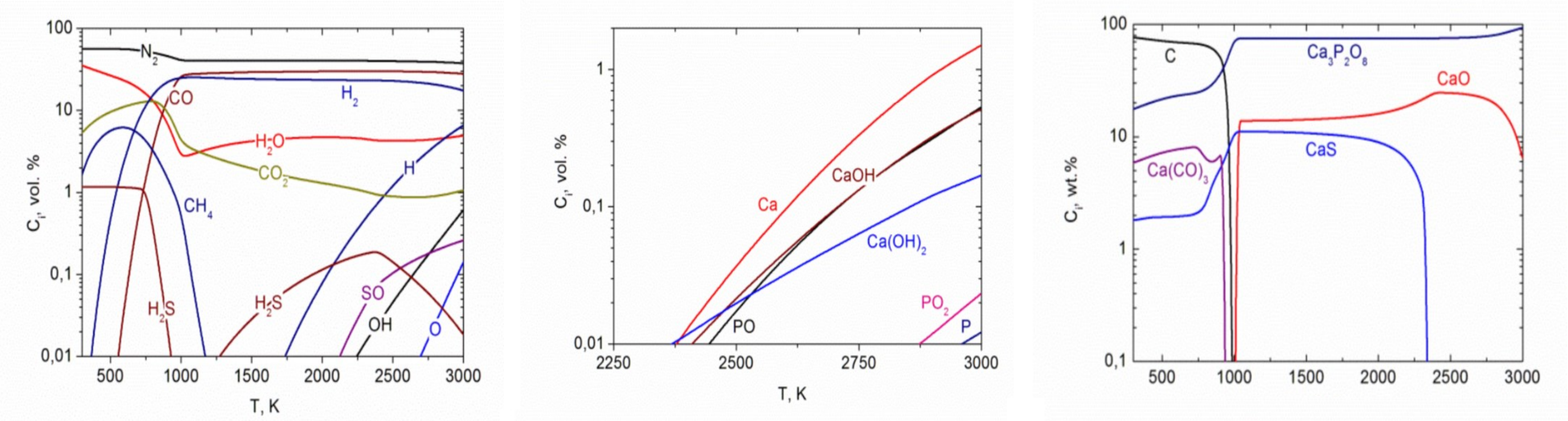

Cas 2

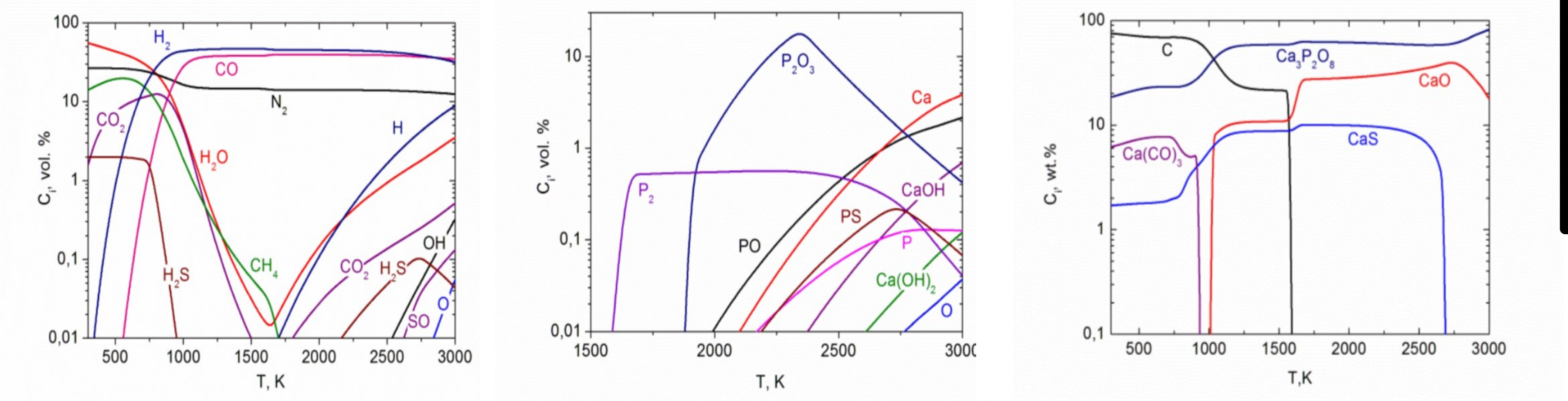

Observation:

- des espèces formées
- espèces carbonées
- espèces condensées

Détermination des températures limites des phases condensées

Plasma treatment of biomedical waste
A. Ustimenko

Dispositif expérimental pour la gazéification

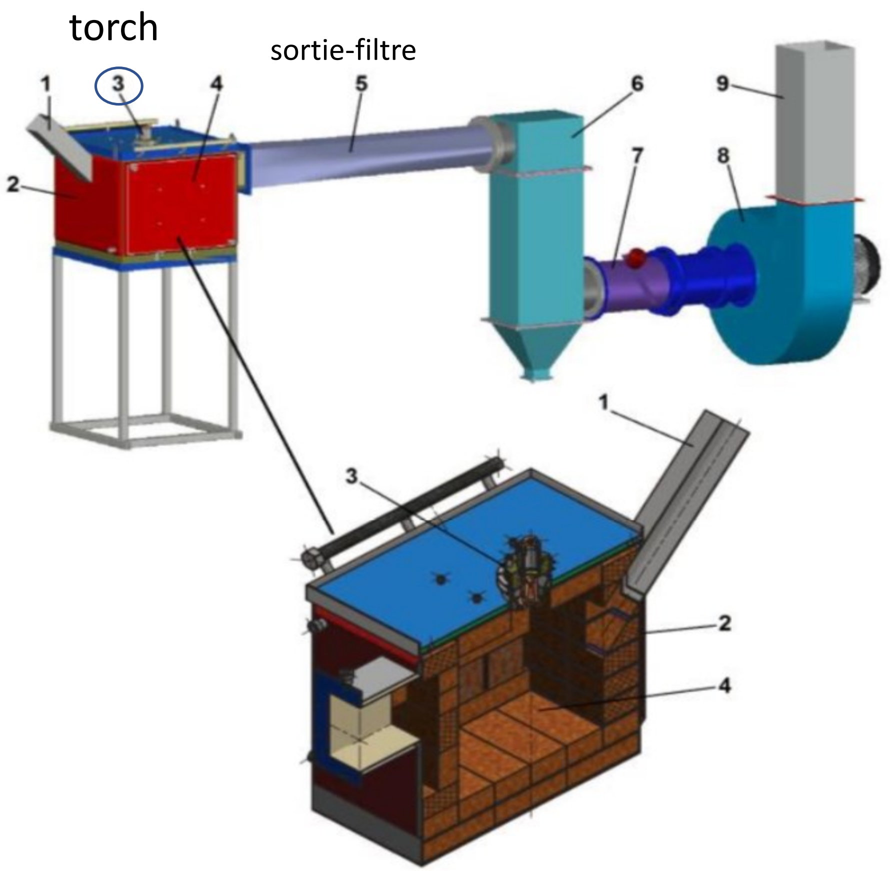

DC plasma torch – 35-70kW
Air, 3.6kg/h (max 30kg/h)
Dimension 0.33m x 0.22m x 0.22m
Epaisseur (réfractaire) : 0.04m
Volume = 0.016m3
Mass process BMW : 5.4-10.8kg/h
3.5-4.6 kW.h/kg

Table 2. Comparison of modelling and experimental results on BT plasma processing.

Method	CO, vol. %	H_2, vol. %	N_2, vol. %	S, vol. %	Ca, wt. %	P, wt. %	O, wt. %	X_C, %	Q_{SP}, kWh/kg
Experiment	63.4	6.2	29.6	0.15	54.6	12.9	32	79.3	4.0
Calculation (variant 1)	28.7	24.7	40.4	0.2	40.9	18.7	40.4	100	1.7

Conclusion : synthèse max < 1600K, permet de dimensionner l’installation.

Papers on nanopowders / nanoparticles fabrication

To simulate turbulent thermal plasma flows for nanopowder fabrication
M. Shigeta

* Review : Shigeta & Murphy : JPhysD 2011
3 catégories : processus de vaporisation, processus de refroidissement, processus de croissance

Challenges : transport properties, plasma flow dynamics inside a torch (heat source important), plasmas flows outside (nanopowders)
Processus de croissance par nucléation, condensation, et coagulation, transport par convection, diffusion et thermophoresis dans/autour du plasma, compliqué : transfert de masse de la microseconde à la milliseconde.

Historique 1990-2018 sur la modélisation de l'écoulement/turbulence en sortie de la torche, 1D, 2D, 3D : 27 ans pour simuler le phénomène (difficile à simuler car 300K-12000K, large banque de propriétés de transport, large variation de la densité (x45), mach number de 0.003 à 0.046, fluide incompressible avec variation de la densité compliqué à simuler.

Patankar est la solution pour la modélisation mais faible précision mais stable

Solutions :
- 1/ faible précision avec très fin maillage et beaucoup de GPs, CVs (impossible en pratique, temps calcul très long)
- 2/ Haute précision mais maillage (more coarse), discrétisation et efforts mathématiques nécessaires (1st order Upwind, 2nd order Central, Hybrid upwind K-K*
- EDDIES : tourbillons

To simulate turbulent thermal plasma flows for nanopowder fabrication
M. Shigeta

Plasma flow **dynamics inside** a torch [Key: Interaction with EM field]

Example **Inside an RF plasma torch with jet assisted**

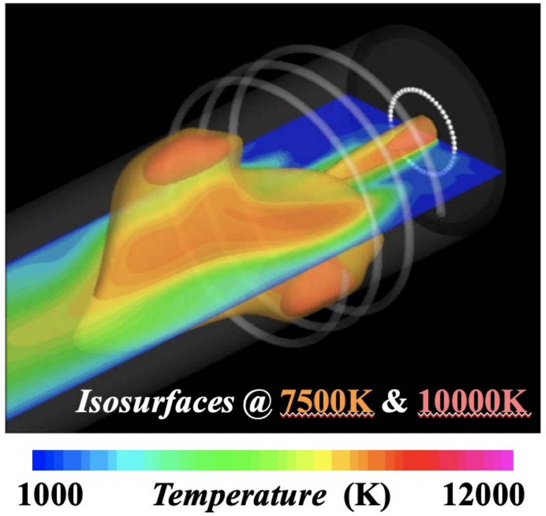

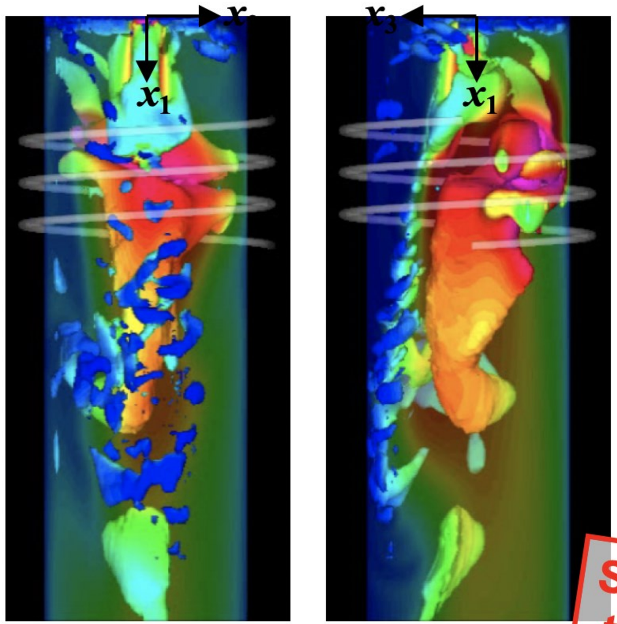

Eddies by Q-criterion

M. Shigeta:
- **Plasma Sources Sci. Tech. (2012)**
- **J. Phys. D: Appl. Phys. (2013)**

Standing on the shoulders of giants!!

M.I. Boulos, P. Proulx (U. Sherbrooke, Canada), J. Mostaghimi (U. Tronto, Canada), S.L. Girshick (U. Minnesota, USA), T. Yoshida (U. Tokyo, Japan), T. Watanabe (Kyushu U., Japan), V. Colombo, E. Ghedini (U. Bologna, Italy), Y. Tanaka (Kanazawa U., Japan) … and more

To simulate turbulent thermal plasma flows for nanopowder fabrication

M. Shigeta

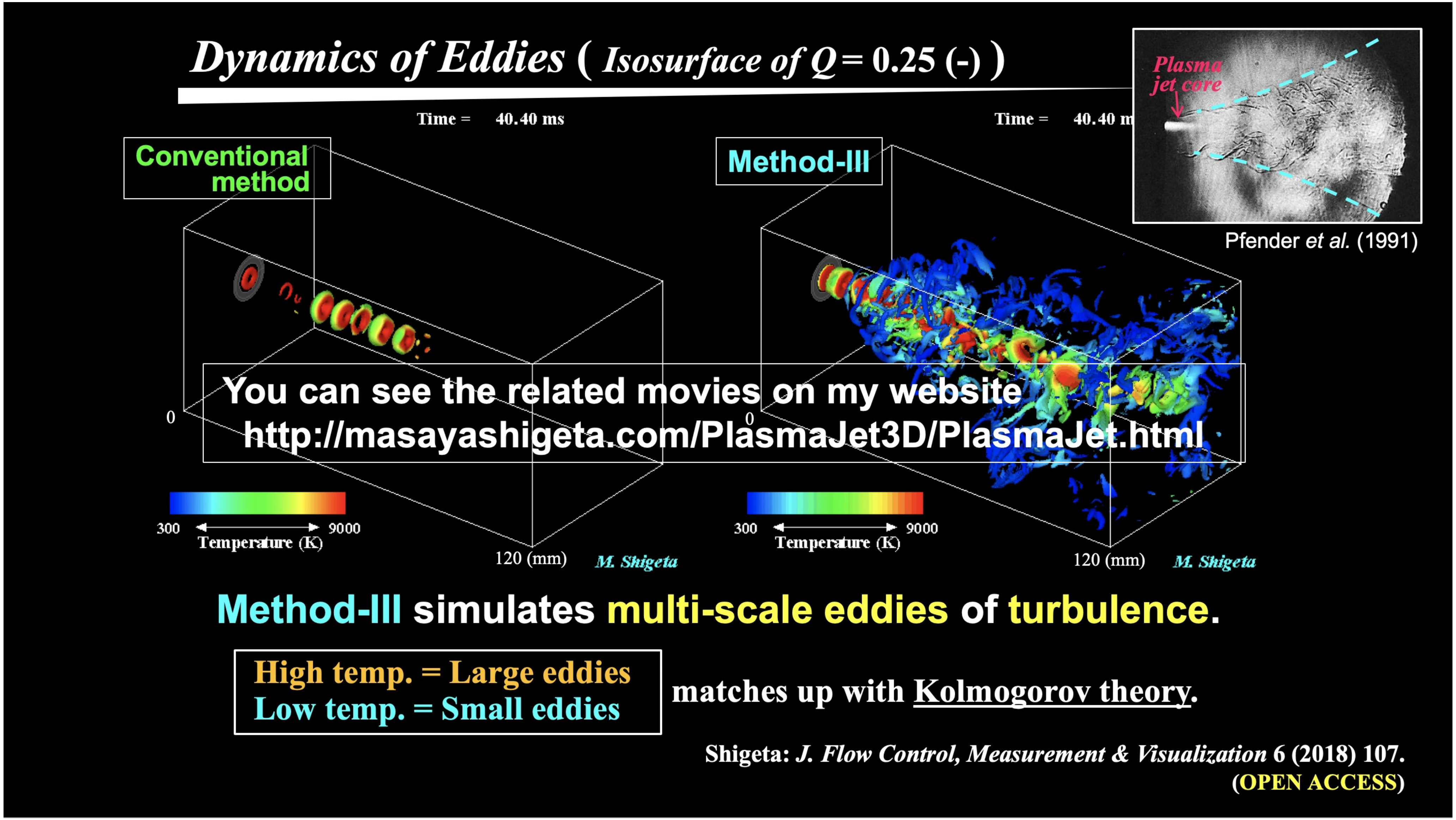

To simulate turbulent thermal plasma flows for nanopowder fabrication

M. Shigeta

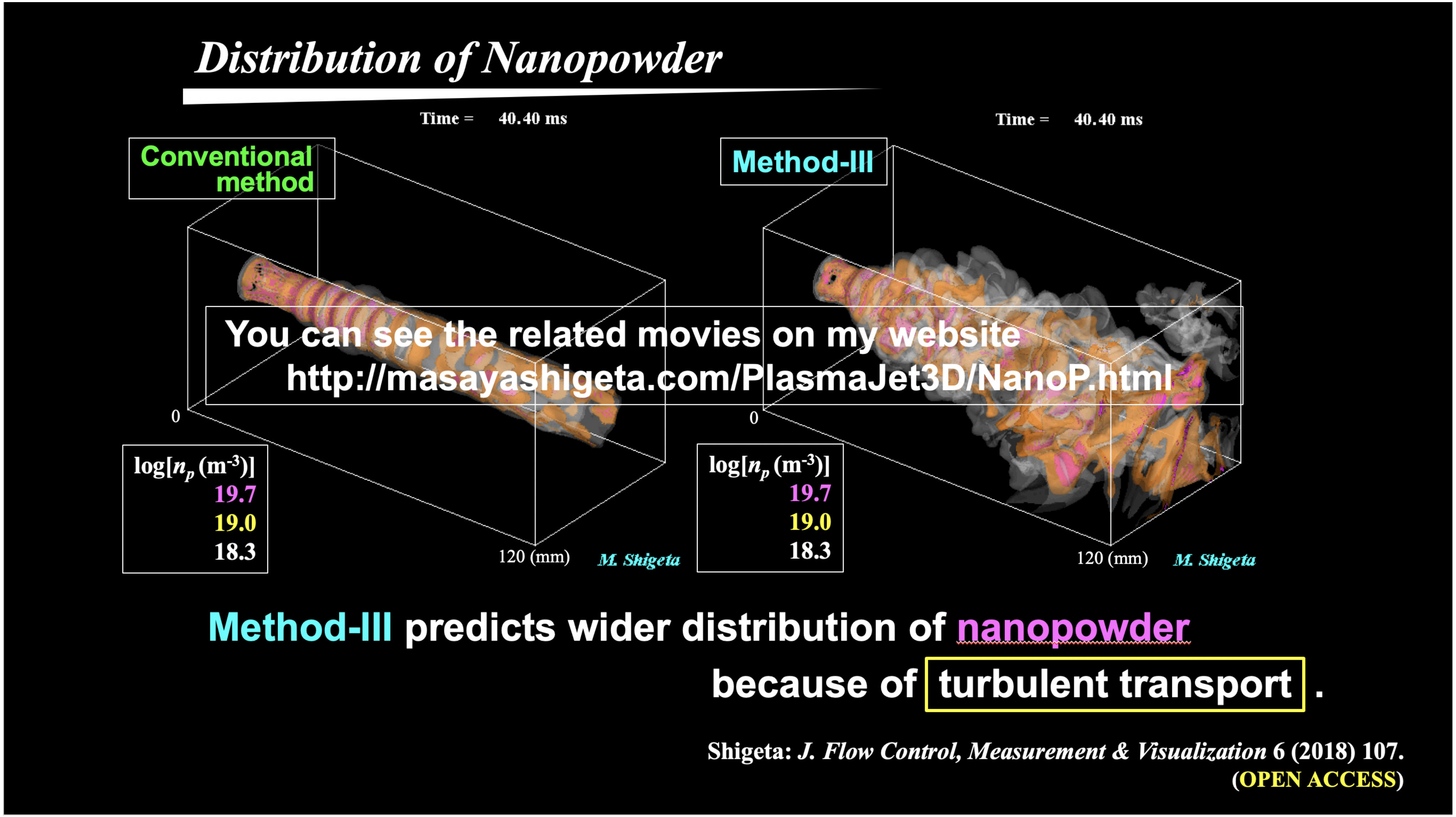

To simulate turbulent thermal plasma flows for nanopowder fabrication
M. Shigeta

Modélisation Nanopoudres Si par plasma Argon
- Convection (Hybrid upwind K-K*) + Transient (3rd order Adams Bashforth-Moulton)
- Termes de diffusion et source (2nd order Central)
- Laminar et turbulent states dans le même run
- Modèle k-eps pas applicable, LES (Large Eddy Simulation) OUI

Résultats

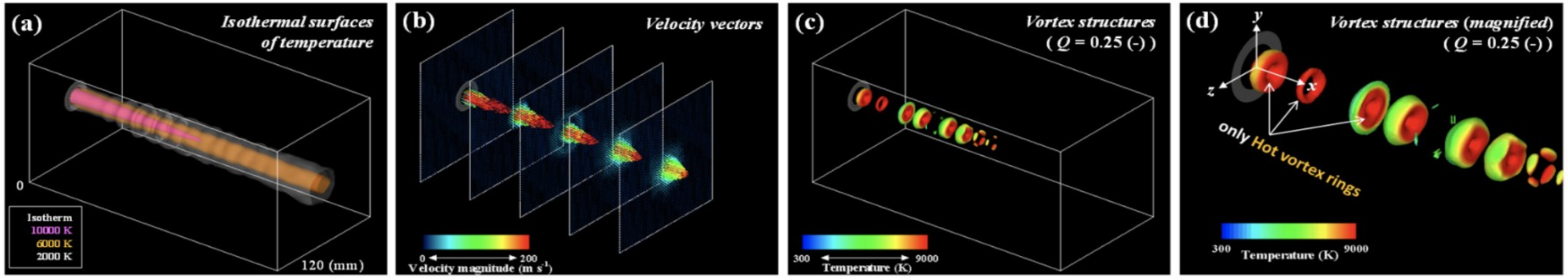

Fig. 2. Instantaneous thermal flow fields in and around a thermal plasma jet obtained by the conventional method.

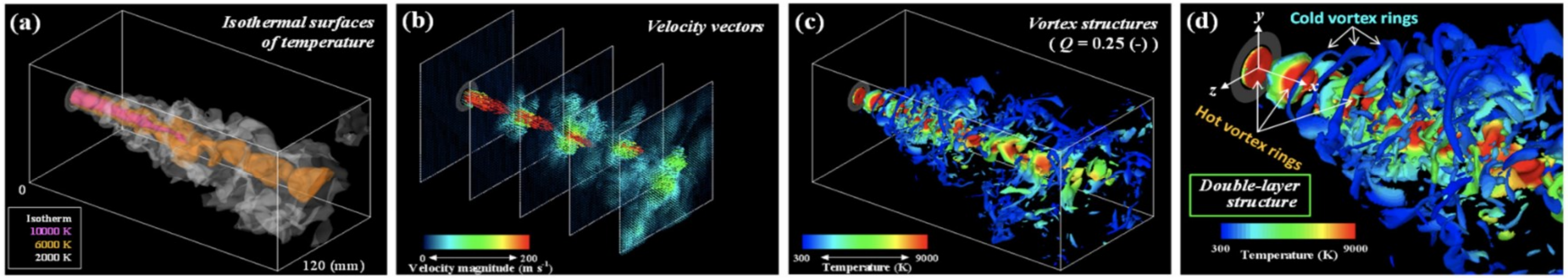

Fig. 3. Instantaneous thermal flow fields in and around a thermal plasma jet obtained by the advanced method.

To simulate turbulent thermal plasma flows for nanopowder fabrication
M. Shigeta

Modélisation de la croissance des nanopoudres
Moment model : nucléation+condensation+coagulation (Nemshinsky+Shigeta WWW)
Method III prédit bien la distribution des poudres à cause du transport sous effet de la turbulence

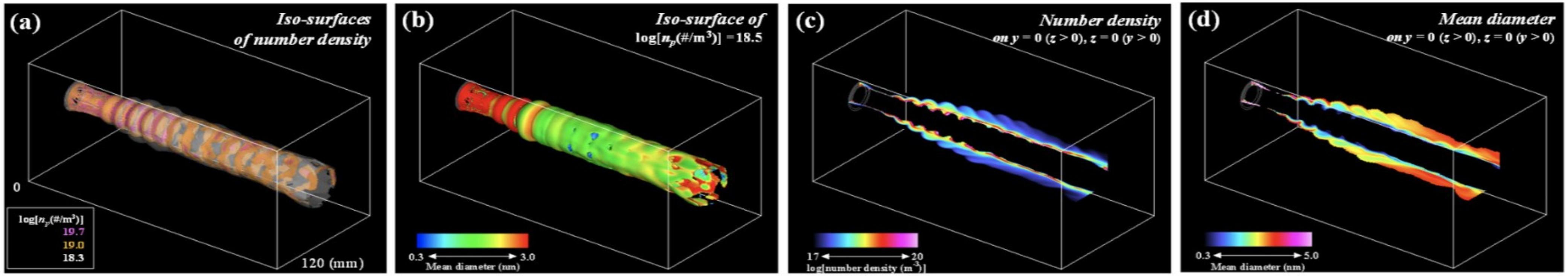

Fig. 4. Instantaneous distributions of nanopowder obtained by the conventional method.

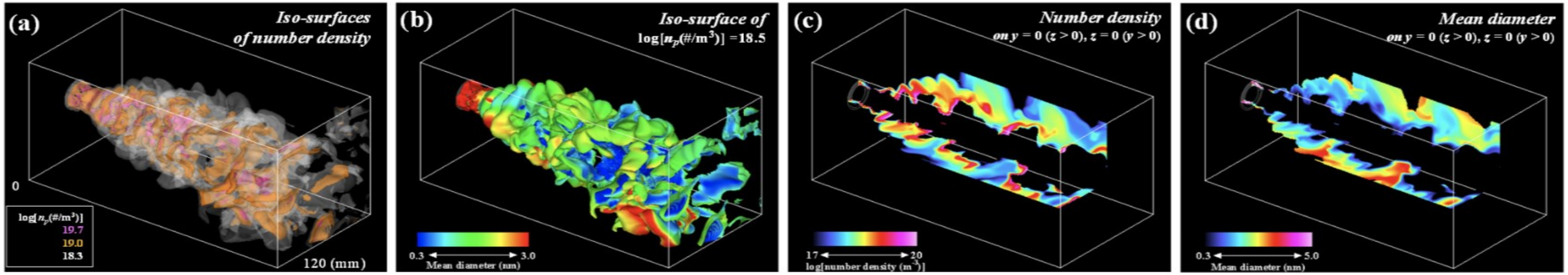

Fig. 5. Instantaneous distributions of nanopowder obtained by the advanced method.

Design-oriented modelling for the synthesis of Cu nanoparticles by a RF thermal plasma : impact of quenching solutions, radiative losses and thermophoresis
V. Colombo

But : Développer des modèles axés sur le design pour réduire les essais couteux et souvent en échec
Avec prise en compte des effets/pertes du rayonnement + thermophoresis sur la synthèse de nanoCu + différence entre les modes active-passive quentching
Active quentching :
Passive quentching :

Papiers: PCPP 2017 (modelling solution quenching) + J.Phys.D.App.Phys 50 2017 (modelling thermophoresis + radiation losses) + PSST 22 2013 (modelling evaporation RF torch) + PSST 21 2012 (modelling nucleation and growth)

H2020 : TRL 6-7, « INSPIRED » pour impression électronique
- Utilisation du quenching gas pour « figer » la croissance des NPs Cu
- Produire 20kg/j avec une taille d'environ 60-70nm

Modèles :
TEKNA PL-50 plasmas torch
Equations fluides + MHD + Méthode des moments pour la synthèse des particules
Etude de Evaporation efficiency
Etude de production efficiency
Etude du Yield

$$\text{Evaporation Efficiency} = \frac{\text{Evaporation rate inside the chamber}}{\text{Precursor feed rate}}$$

$$\text{Production Efficiency} = \frac{\text{Vapour to nanoparticle conversion rate}}{\text{Precursor feed rate}}$$

$$\text{YIELD} = \frac{\text{Nanoparticle rate to collection chamber}}{\text{Precursor feed rate}}$$

Design-oriented modelling for the synthesis of Cu nanoparticles by a RF thermal plasma : impact of quenching solutions, radiative losses and thermophoresis

V. Colombo

Effet des pertes radiatives (vapeurs de Cu)

Fort refroidissement du au présence de vapeurs de cuivre

Evaporation plus élevée sans prise en compte des pertes radiatives

L'augmentation de la puissance a un faible impact sur l'évaporation

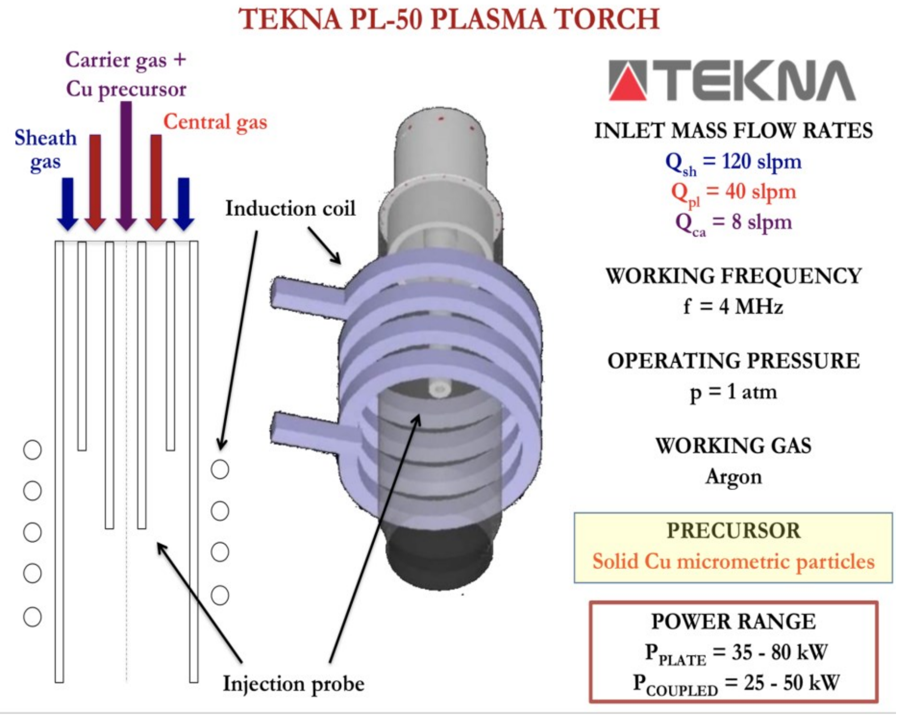

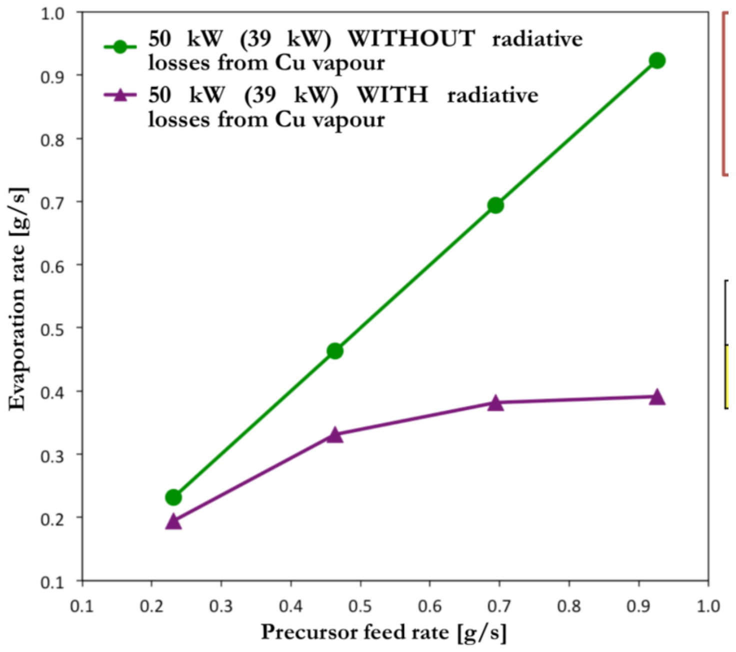

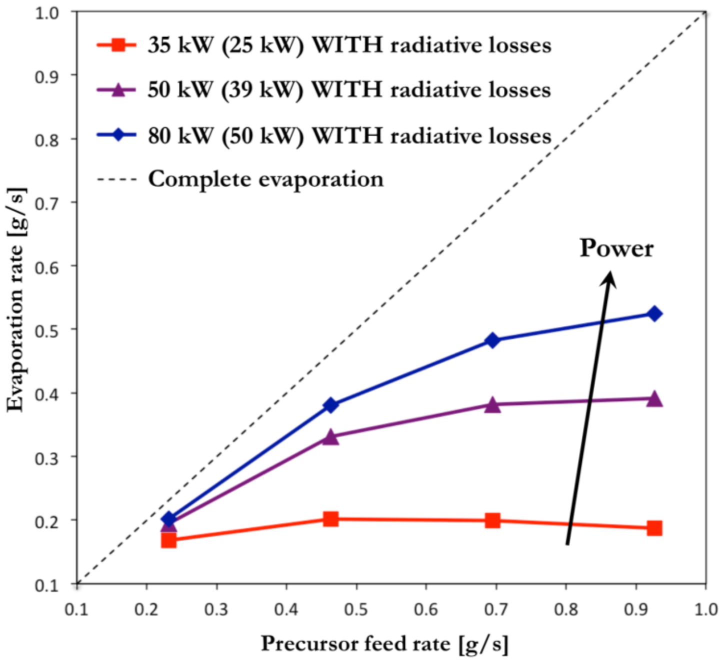

Design-oriented modelling for the synthesis of Cu nanoparticles by a RF thermal plasma : impact of quenching solutions, radiative losses and thermophoresis

V. Colombo

Effet des solutions quenching (passive/active)

Avec active : %nano sur les bords

Avec passive : meilleur taux, %nano faible sur les bords + plus débit augmente, formation de vortex qui diminuent le taux de production

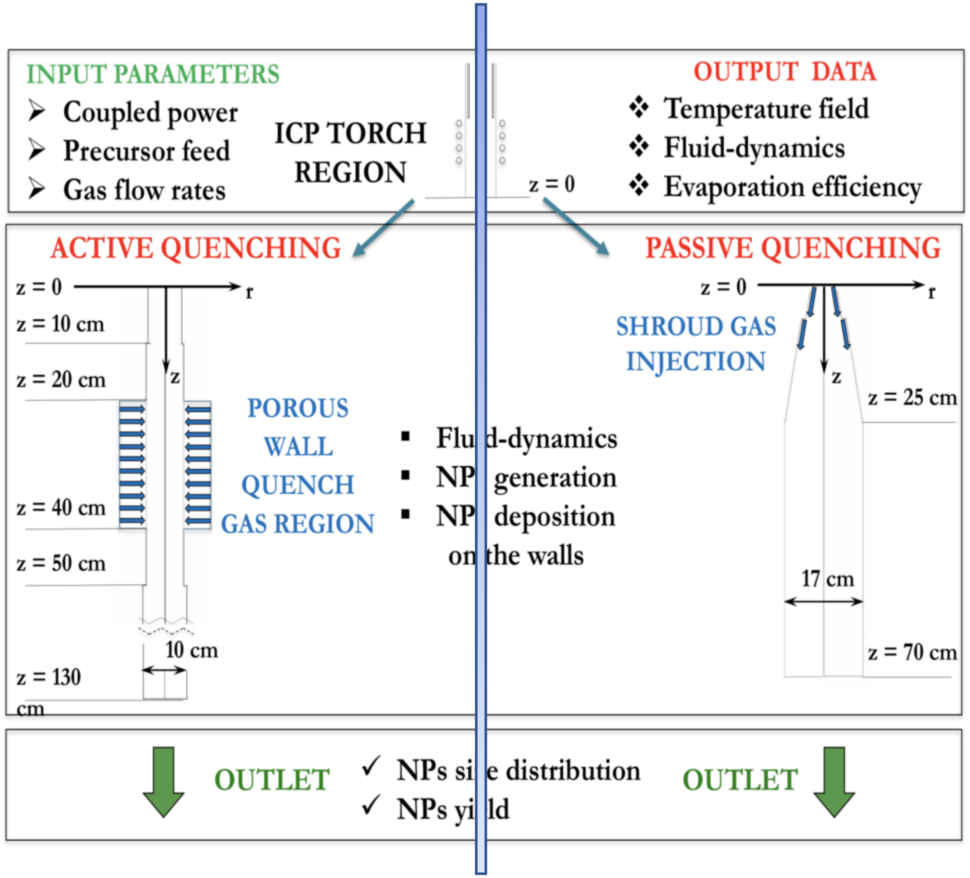

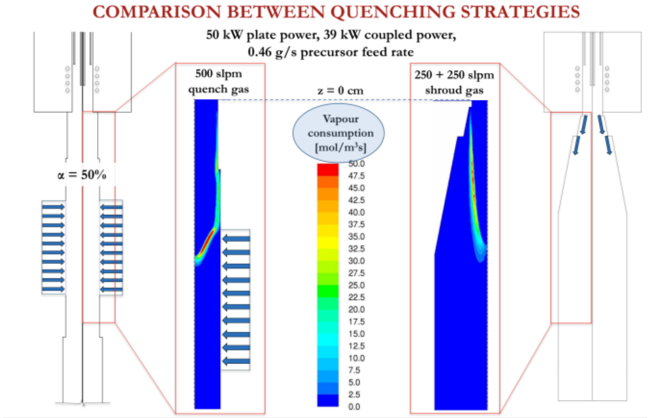

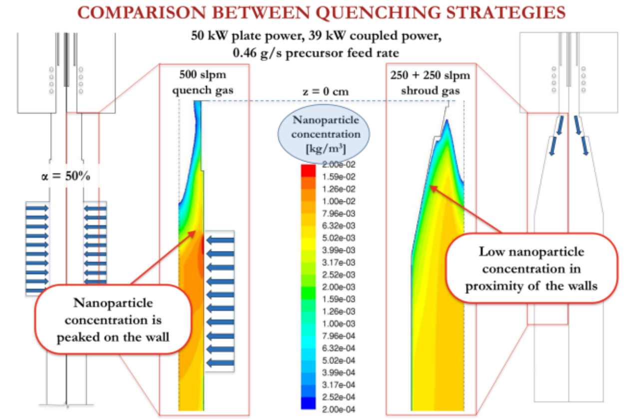

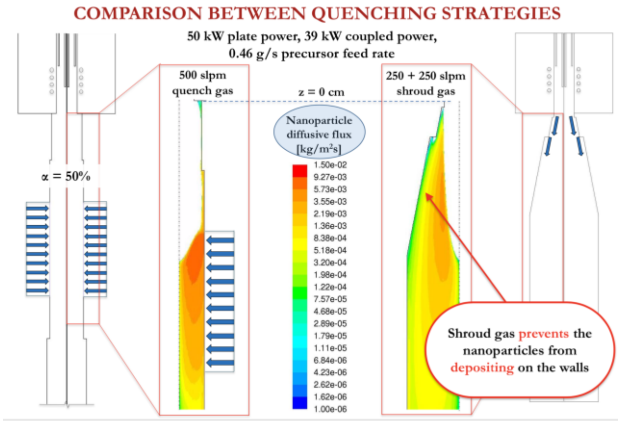

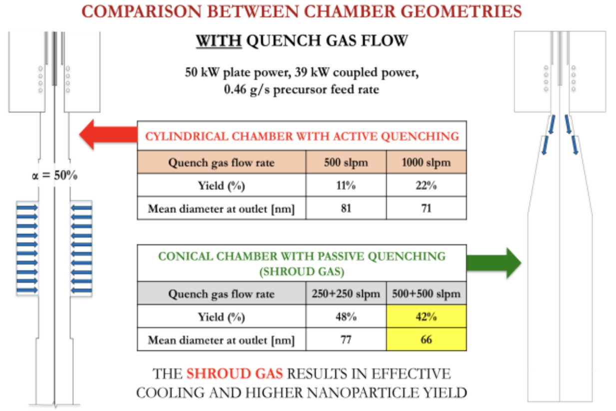

Design-oriented modelling for the synthesis of Cu nanoparticles by a RF thermal plasma : impact of quenching solutions, radiative losses and thermophoresis

V. Colombo

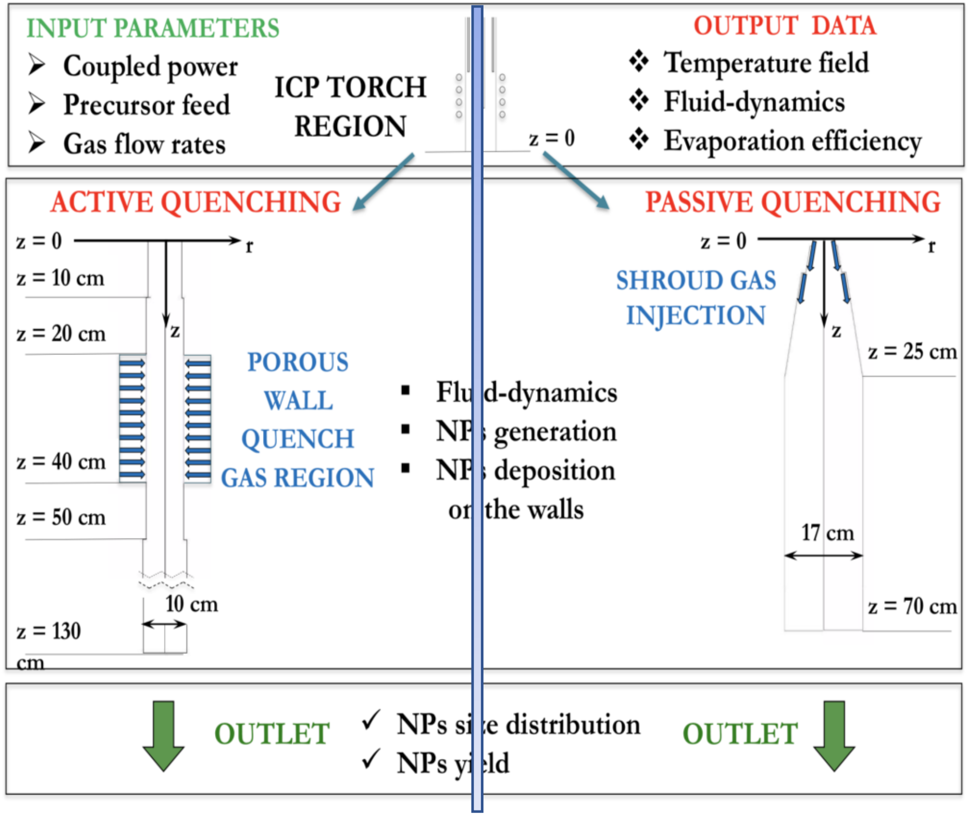

Effet de la thermophorese

Quenching induit de fort gradients de temperature (sortie de torche)

Flux thermophorese plus intense (at the top of the chamber)

Légère réduction du taux, dépôt plus important sur les bords, plus faible sur l'axe, taille plus petite

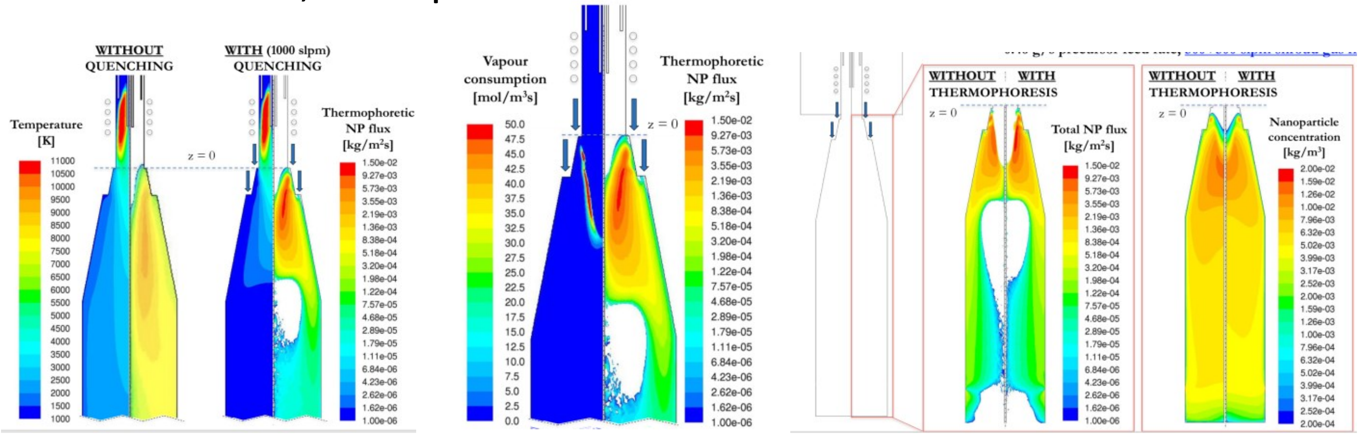

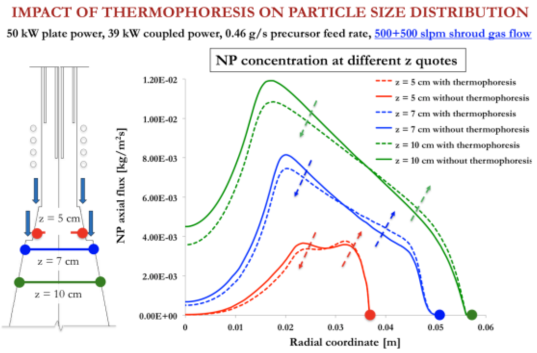

THERMOPHORESIS ALWAYS RESULTS IN A LOWER PARTICLE DIAMETER

Chamber and quenching strategy	Quench	Thermophoresis	Yield (%)	d_p at outlet [nm]
CYLINDRICAL WITH ACTIVE QUENCHING	No	No	11%	116
		Yes	7%	106
	1000 slpm	No	22%	71
		Yes	17%	65
CONICAL WITH PASSIVE QUENCHING	No	No	16%	93
		Yes	10%	81
	1000 slpm	No	42%	66
		Yes	38%	64

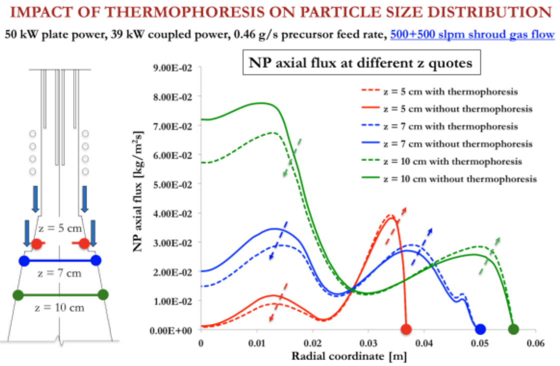

Effect of alternating gas injection on temperature flieds in reaction chamber using inductively coupled thermal plasma for nanoparticle synthesis

Y. Tanaka

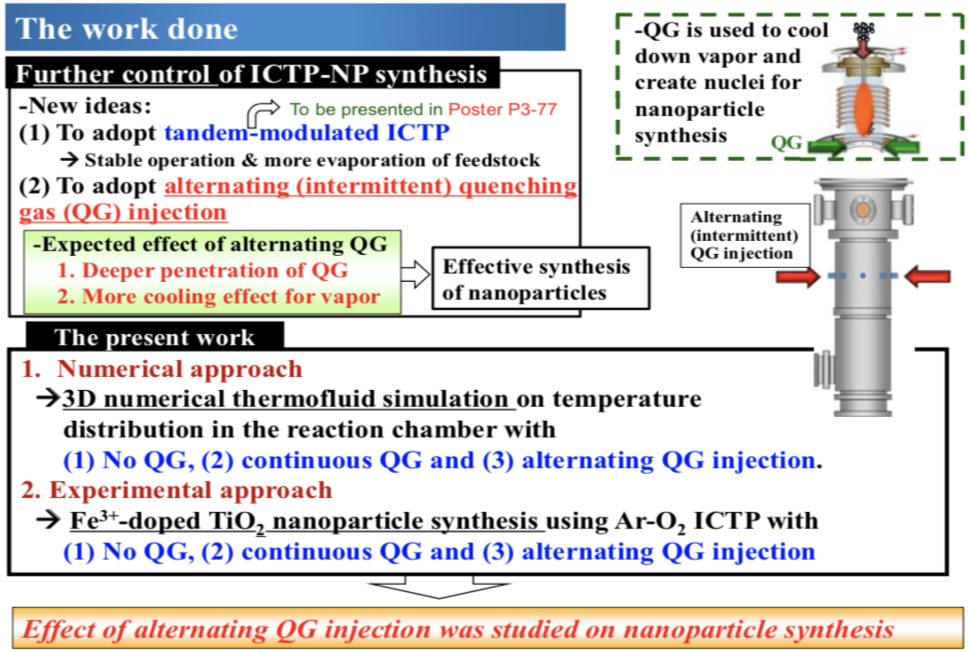

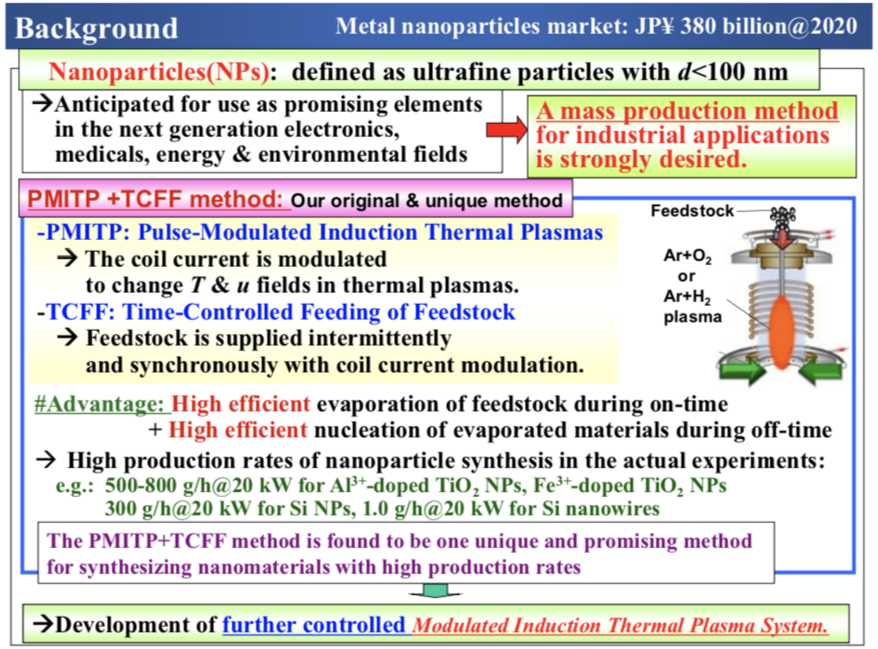

<u>Objectif :</u> synthèse de nanoparticules

- Utiliser PMITP + TCFF method
- Adopter « alternating quenching gas injection AQGI »

Voir l'effet AQGI sur synthèse nano.

Modèle 3D pour obtenir T(r) dans réacteur

(1) No quentching gas,
(2) continuous QG
(3) alternating QG injection
(4) ICTP torch, COMSOL 5.3

Etudes expérimentales

(1)+(2)+(3)

Effect of alternating gas injection on temperature flieds in reaction chamber using inductively coupled thermal plasma for nanoparticle synthesis

Y. Tanaka

Calc. space & procedure for 3D thermofluid simulation

(1) Calculation space for 3D simulation

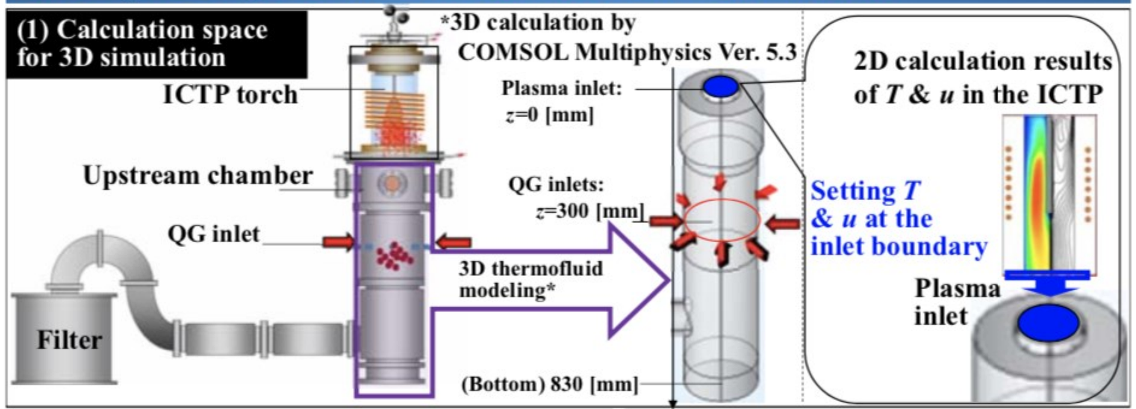

(2) Calculation procedure of 3D thermofluid modeling

1) 3D calculation space was defined for the chamber downstream of the ICTP torch.
2) For the thermal plasma flow at plasma inlet, 2D calculation was made to obtain the temperature and gas flow velocity.
3) These were given as the boundary condition.
4) QG was set to be supplied from 8 ports located at the wall of the chamber.
5) QG flow rate was set to be modulated in case of alternating injection.

(3) Gas flow velocity of alternating QG

-QG was assumed to be supplied with a sinusoidal waveform at a given cycle Tcyc. with a given time-averaged flow rate:

$$Q_{\mathrm{avg}} = \frac{1}{Tcyc}\int_0^{Tcyc} f_{\mathrm{QG}}(t)\,dt$$

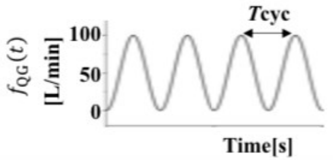

Governing equations & calculation condition

Governing equation

-Mass conservation

$$\frac{\partial \rho}{\partial t} + \nabla \cdot (\rho \boldsymbol{u}) = 0$$

-Navier Stokes equation

$$\rho\frac{\partial \boldsymbol{u}}{\partial t} + \rho(\boldsymbol{u}\cdot\nabla\boldsymbol{u}) = \nabla\cdot\left[-p\boldsymbol{I} + \mu(\nabla\boldsymbol{u} + (\nabla\boldsymbol{u})^T) - \frac{2}{3}\mu(\nabla\cdot\boldsymbol{u})\boldsymbol{I}\right]$$

-Energy transport equation

$$\rho C_p\frac{\partial T}{\partial t} + \rho C_p\boldsymbol{u}\cdot\nabla T = \nabla\cdot(\kappa\nabla T) - p\nabla\cdot\boldsymbol{u} + Q_{\mathrm{vd}}$$

-Equation of state: $p = \rho R(T)T$

Common condition

-Laminar flow
-Gas species: 100%Ar
-Wall temp.: 300 K
-Time-averaged QG flow rate: 50 L/min
-QG gas temp.： 300 K

ICTP condition

-Mod. of power: Non-mod.
-Input power: 20 kW
-Pressure: 300 torr
-Sheath gas: 90 L/min Ar gas
-Feedstock: Not supplied

The T & u calculated in advance by 2D simulation of ICTP were used for boundary condition at the plasma inlet.

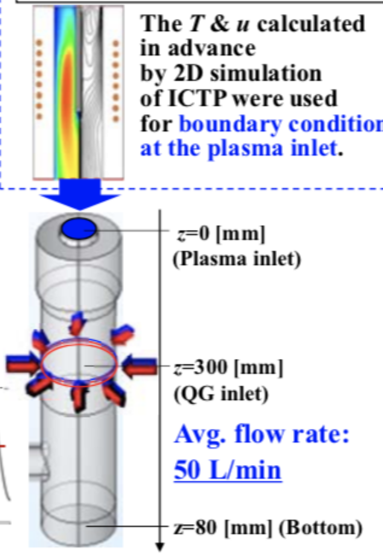

Conditions for comparison

	Modulation of QG	Cycle-time T
Condition-1	Continuous	–
Condition-2	Alternating	30 ms
Condition-3	Alternating	100 ms

Modulation of QG

-QG was set to change as sinusoidal waveform with an avg. rate of 50 L/min & a maximum peak rate of 100 L/min.

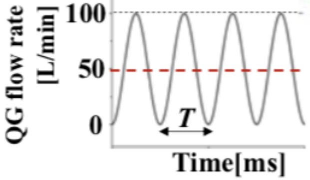

Effect of alternating gas injection on temperature flieds in reaction chamber using inductively coupled thermal plasma for nanoparticle synthesis

Y. Tanaka

Temperature distribution in the chamber w/o or w/ QG gas injection

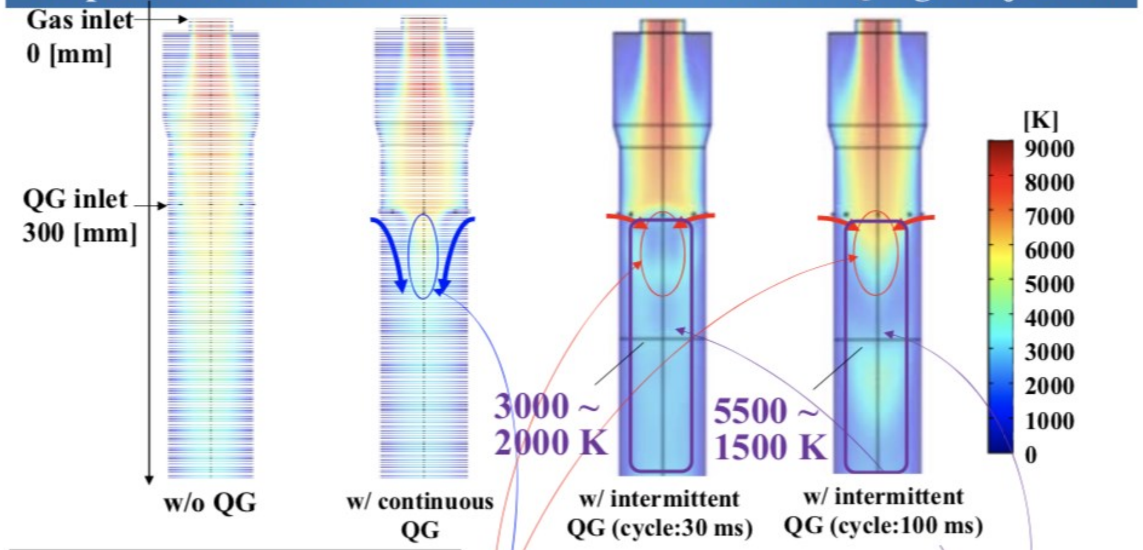

Results for different QG conditions

-Continuous inject.→ QG hardly reaches to the axis→ Axis *T* is weakly decreased.
-Alternating inject.→ QG is transported more deeply→ *T* effectively decreases.
(Cycle:30 ms) Alternating QG offers relatively uniform *T* distribution.
(Cycle:100 ms) Alternating QG produces periodical *T* distribution.

→Next, axial temperature distribution.

Axial temperature distributions in the chamber at three QG injections

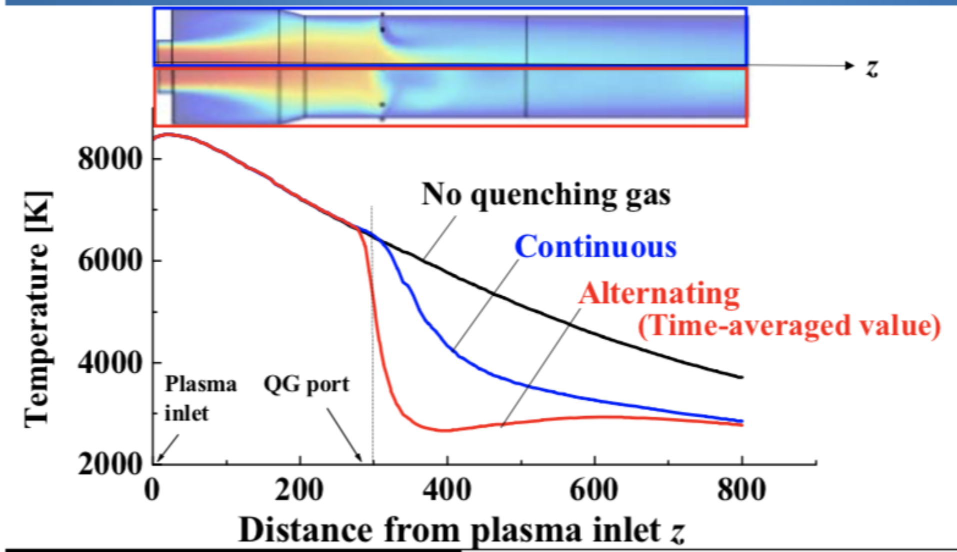

Results for different QG conditions

-Alternating QG injection results in the lower time-averaged temperature and minimum temperature than continuous QG injection.
←Deep penetration of alternating QG injection.

Next, we conducted experiments for nanoparticle synthesis using this intermittent alternating quenching gas injection technique.

→Results indicated that alternating QG can penetrate the ICTP, resulting in effective cooling of the thermal plasma in the chamber.

Effect of alternating gas injection on temperature flieds in reaction chamber using inductively coupled thermal plasma for nanoparticle synthesis

Y. Tanaka

Etude expérimentale

Synthèse nanoparticles (Fe^{3+} dopées TiO_2)

Ar-O_2 torch

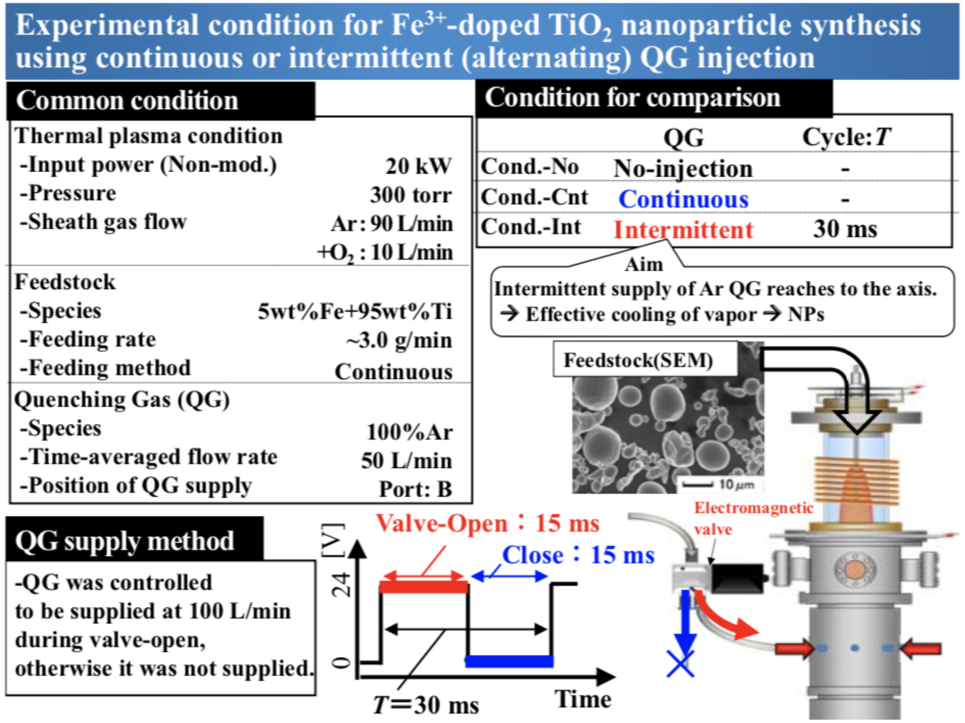

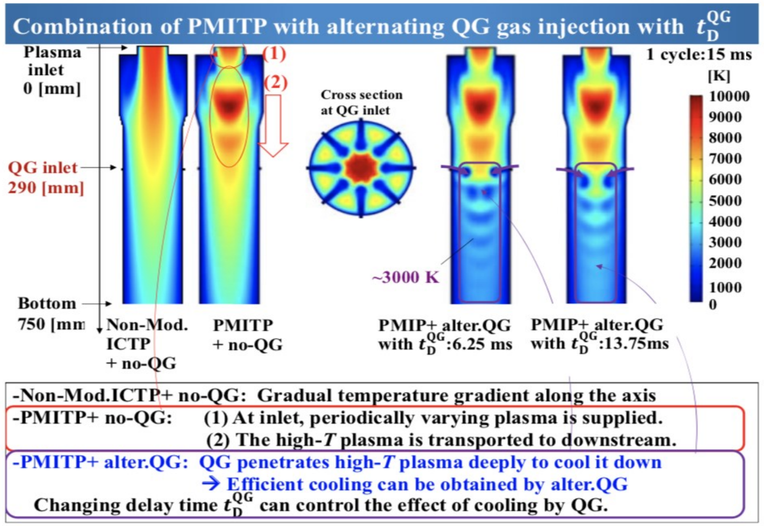

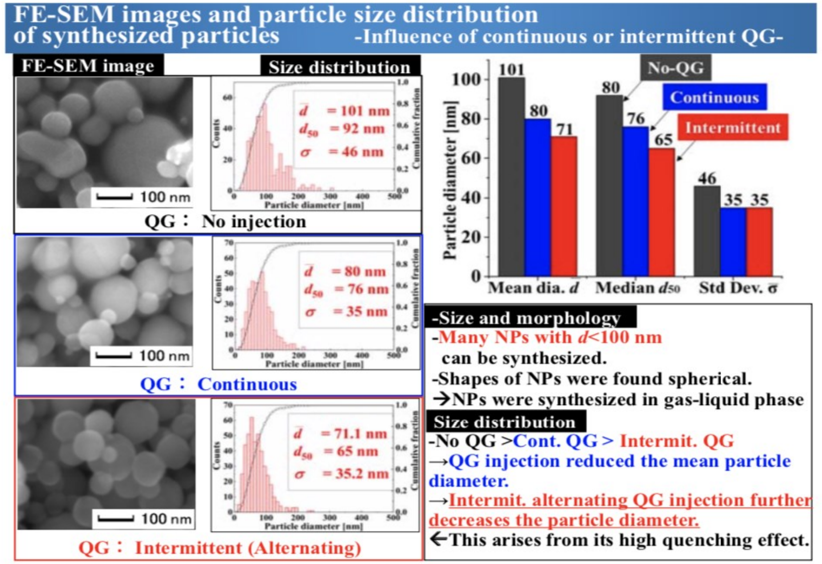

alternating QG provides smaller nanoparticles.
This is due to its high cooling effect on thermal plasma and vapor of feedstock, avoiding particle growth in the chamber.

Papers on Non-equilibrium phenomena

Non equilbrium phenomena in thermal plasmas

J.P. Trelles

Non equilibrium

Microscopique

-> Kinetic non-equilibrium

- Imbalance between particles and fields (Te, Th)
- Quasi-neutrality
- With low gradients
- Anode sheath, near sheath
- When molecules exist (synthesis processes, with vapeurs…)
- Mass action law is invalide
- Linear relaxation system
- **Thermodynamic nonequilibrium** (deviation from LTE)
- **Chemical nonequilibrium** (deviation from mass action law)
- **Multi-phase interaction** (plasma-solid interactions, plasma-anode, liquid, vapors)
- **Radiation transport** (if molecules or high θ) -> motivation solar fuel, Solar+electricity+CO2-> fuels, Solar enhanced Microwave plasma (SEMP) : greater solar absorption by plasma, increase conversion and efficiency à la Patm

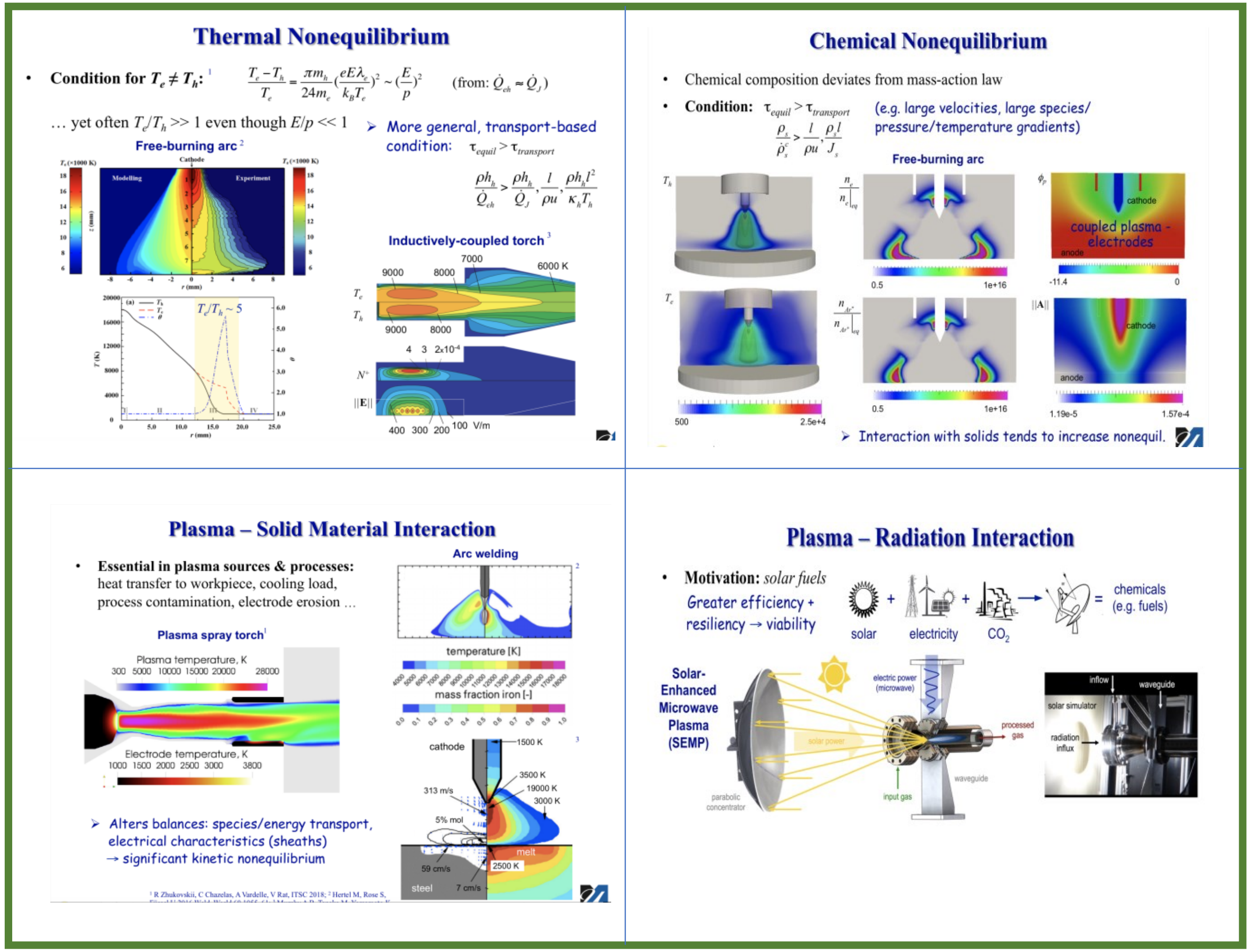

Non equilbrium phenomena in thermal plasmas

J.P. Trelles

Non equilibrium

Macroscopique
-> Dissipative non-equilibrium

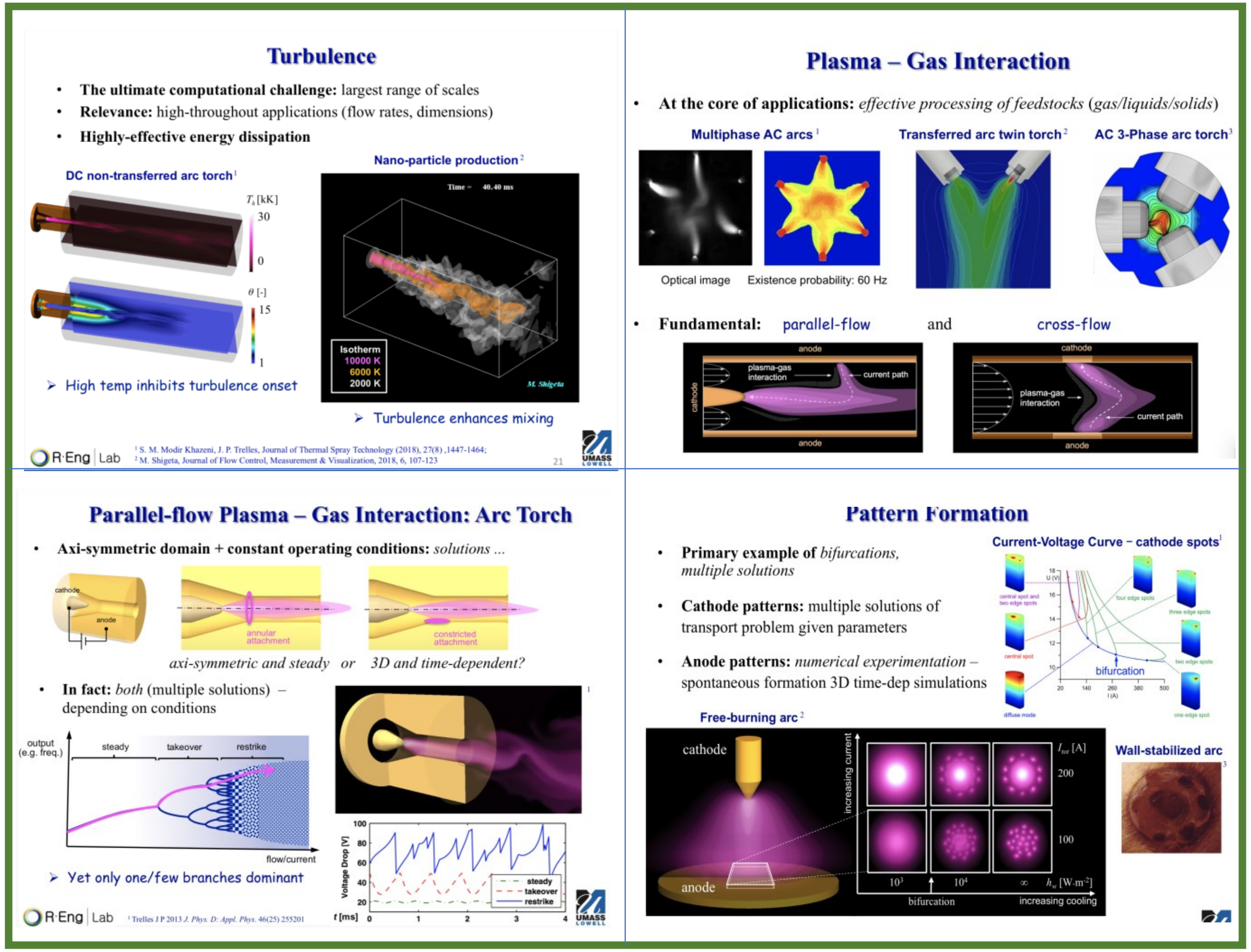

- Instability due to external forces(mass flow, heat flux, voltage)
- High variations, deviations
- Anode attachment, liquid-cooled metal anode, multiple anode attachment configurations
- Non linear system
- Multiple solutions, bifurcation when P=Pcritic (dissipative equilibrium if P<Pcrit, non equilibrium if P>Pcrit), ultim=chaos and turbulence
- θ increase, nbre solutions increases
- **Flow stability** (plasma-gas flow interaction, fluid dynamic, thermal, electromagnetic)
- **Pattern formation** (erosion of electrodes cathode-anode)
- **Turbulence**
- **Multi-electrodes**

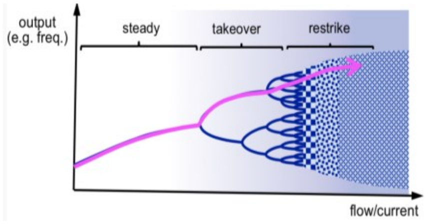

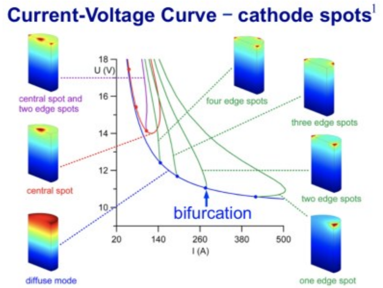

A 3D two-temperature model of loop type of arc inductively coupled thermal plasmas for large-area materials processing
Y. Tanaka

Constats : ICTP est avantageux : haute température du gaz, haute enthalpie, haute densité des radicaux, pas d'érosion
Mais avec ICTP, difficile de contrôler la forte enthalpie (impact Temp sur substrat), et les applications sont limitées
-> développement d'une loop ICTP torch : plus rapide et surface de traitement plus large

Expérience : Linear ICTP torch Ar/O_2 sur substrats Si, SiC (pour semi-conducteurs)
Développement méthode ultra-rapide de la modification de la surface
Taux d'oxidation : 100nm/min (contre 10nm/min habituellement)

Ar/O_2 loop-ICTP, 140A, 2.5kW, 360kHz, 10 torr, Q=0.1L/min
Traitement de surface en 2D

Résultat :
Substrat SiC oxidé uniformément sur 25mm de diamètre en seulement 3min
2D rapid oxidation 4H-SiC substrates à 20nm/min.
Profondeur de l'oxidation : 70mm

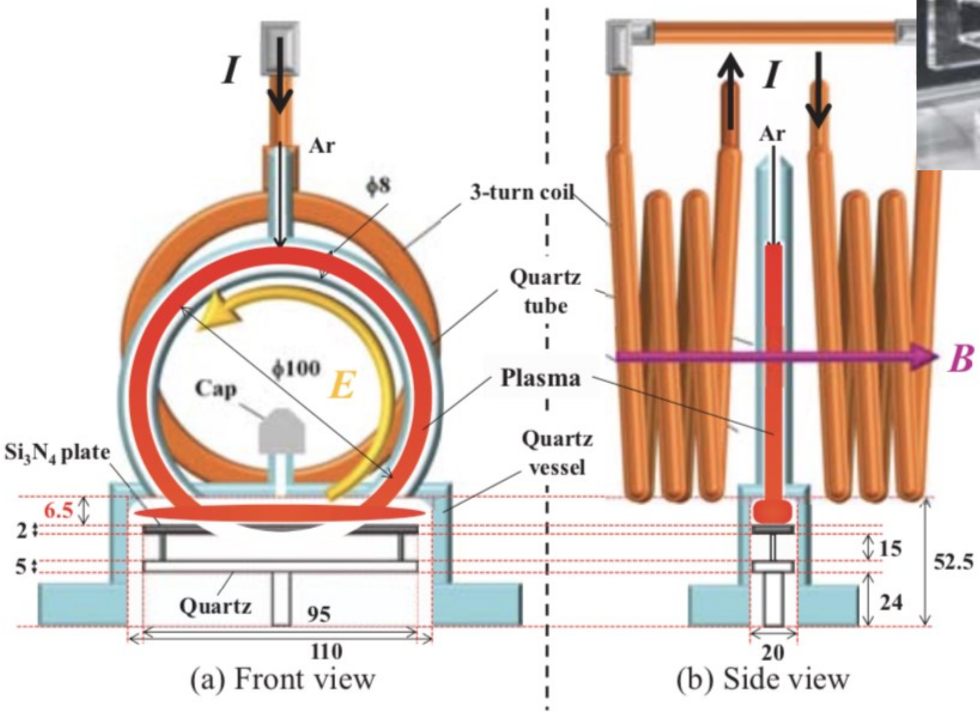

A 3D two-temperature model of loop type of arc inductively coupled thermal plasmas for large-area materials processing

Y. Tanaka

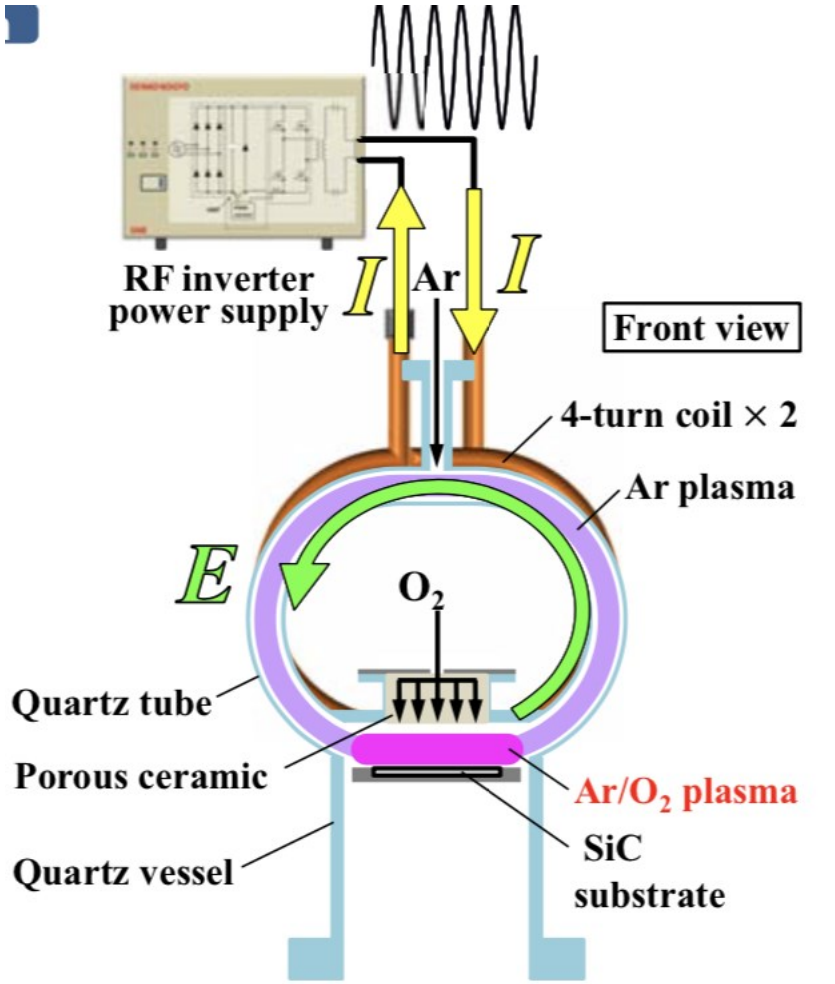

Surface oxidation result for 2-inch 4H-SiC substrate

A photo of a 4H-SiC(0001) substrate after scanning exposure by Ar/O_2 loop-ICTP

2D distribution of oxide layer thickness

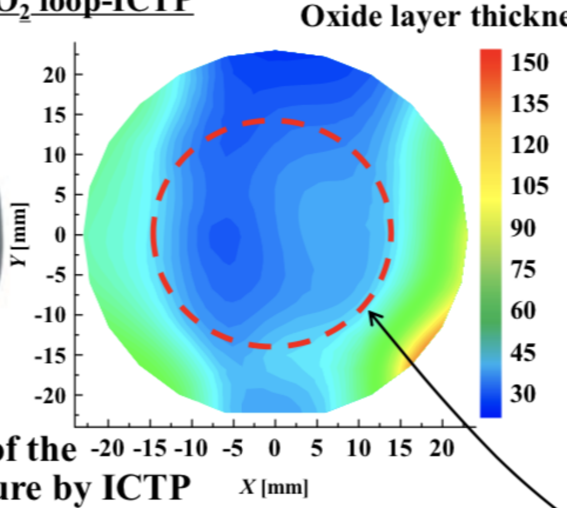

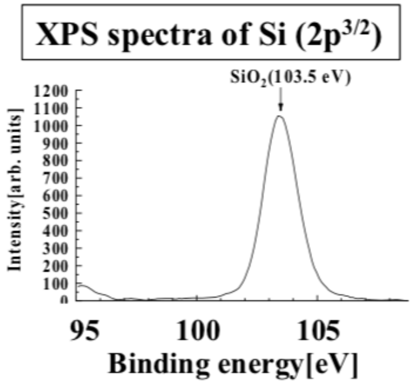

Backside temperature of the substrate during exposure by ICTP was 1213 K at exposure point.

-The SiC substrate surface was oxidized almost uniformly in a region of 25 mmϕ only by 3 min scanning exposure of Ar/O_2 loop-ICTP.
→ -The resultant oxide layer thickness is about 70 nm in that region.
-Effective oxidation rate was estimated as 20 nm/min, which is 20 times faster than those by the conventional thermal oxidation method.

This extremely rapid oxidation rate may be attributed to high-*Th* & high density atomic oxygen.

A 3D two-temperature model of loop type of arc inductively coupled thermal plasmas for large-area materials processing

Y. Tanaka

Modélisation : COMSOL 5.3, modélisation 3D (1D fluide, 2T température plasma pour transfert le énergie des électrons vers les lourds par collision élastique)

Sphère de calcul de 250mm

Equations classiques + 2 eqns k-eps pour effets turbulence (pour simplifier)

T_e et T_h traitées séparément, équilibre ionisation et excitation

Plasma optiquement mince, T_{vib}=10000K, T_{rot}: 3000K, 10torr, 140A_{rms}, 360Hz, 2.51kW

Calculation domain, mesh for calculation

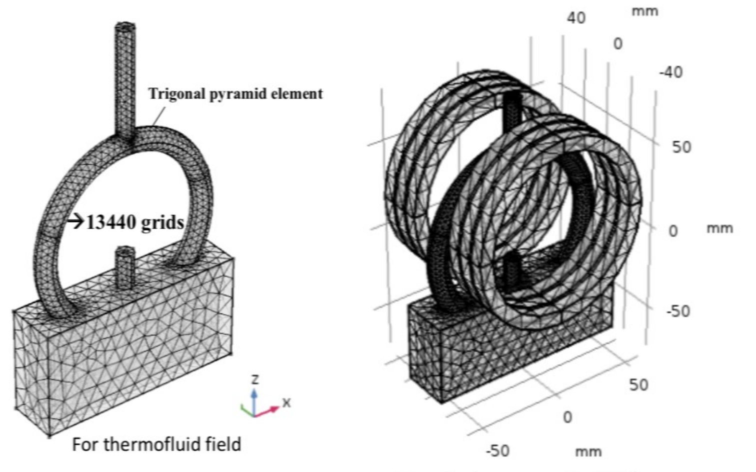

-COMSOL Multiphysics ver.5.3 was used for this 3D calculation.

For electromagnetic fields, we took a sphere calculation space with a diameter of 250 mm.

Governing equations for a 1-fluid and 2-temperature plasma

-Mass

$$\frac{\partial \rho}{\partial t} + \nabla \cdot (\rho \boldsymbol{u}) = 0$$

-Momentum

$$\rho \frac{\partial \boldsymbol{u}}{\partial t} + \rho (\boldsymbol{u} \cdot \nabla) \boldsymbol{u} = -\nabla p + \nabla : \boldsymbol{\tau}$$

$$\boldsymbol{\tau} = \tau_{ij} = 2\eta_{\mathrm{eff}} \left[e_{ij} - \frac{1}{3} \delta_{ij} (\nabla \cdot \boldsymbol{u}) \right]$$

-Energy for heavy particles

$$\rho C_p \frac{\partial T_h}{\partial t} + \rho C_p (\boldsymbol{u} \cdot \nabla T_h) = \nabla \cdot (\kappa_{\mathrm{eff}} \nabla T_h) + E_{eh}$$

-Energy for electrons

$$\nabla \cdot (\kappa_e \nabla T_e) = e n_e \mu_e \boldsymbol{E} \cdot \boldsymbol{E} - E_{eh} - P_{rad}(T_e)$$

-Energy transfer from electrons to heavy particles

$$E_{eh} = \frac{2 m_e m_{Ar}}{(m_e + m_{Ar})^2} \frac{3}{2} k (T_e - T_h) n_e (n_{Ar} \pi \overline{\Omega}_{eAr} + n_{Ar+} \pi \overline{\Omega}_{eAr+}) \bar{v}_{eAr}$$

-Saha's equation for ionization

$$\frac{n_e n_{Ar+}}{n_{Ar}} = 2 \left(\frac{2\pi m_e k T_e}{h^2} \right)^{\frac{3}{2}} \frac{Z_{Ar+}(T_e)}{Z_{Ar}(T_e)} \exp\left(-\frac{E_{Ar}}{k T_e} \right)$$

-Vector potential

$$\nabla \times (\nabla \times \boldsymbol{A}) = \mu_0 (\omega^2 \varepsilon - j e n_e \mu_e \omega) \boldsymbol{A}$$

$$\boldsymbol{B} = \nabla \times \boldsymbol{A}$$

$$\boldsymbol{E} = -j\omega \boldsymbol{A}$$

-To solve electron energy and Saha's equations, general partial differential equation (PDE) solver was used.
-2 eqns k-ε model was used to consider turbulent effects for simplicity.

cf. Exp.→2T-state
Tvib~10000K,
Trot~3000 K in
Ar/N_2 loop-ICTP
@10,20 torr, 10 kW

Boundary conditions

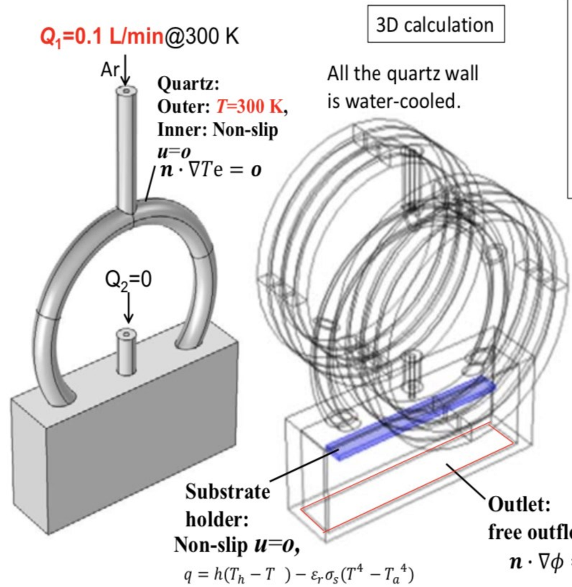

Condition
-Gas: Ar
-Gas flow rate: 0.1 L/min
-Pressure: 10 torr
-Coil current: 140 Arms
-Current freq.: 360 kHz
→2.51 kW

Operated in COMSOL

A 3D two-temperature model of loop type of arc inductively coupled thermal plasmas for large-area materials processing

Y. Tanaka

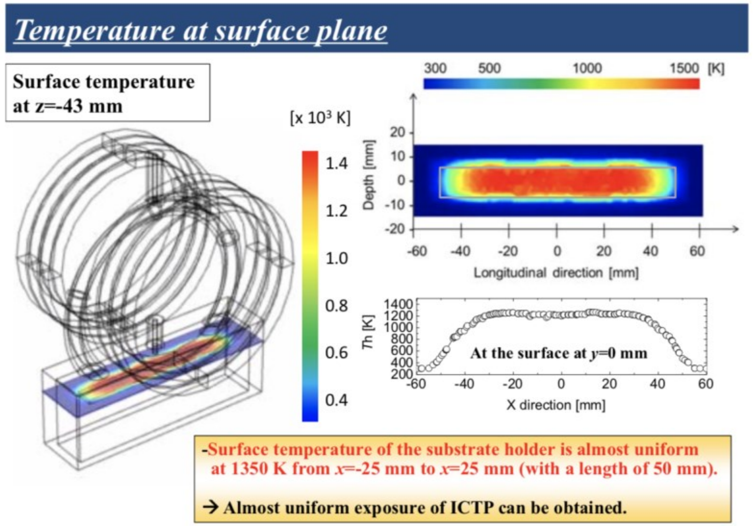

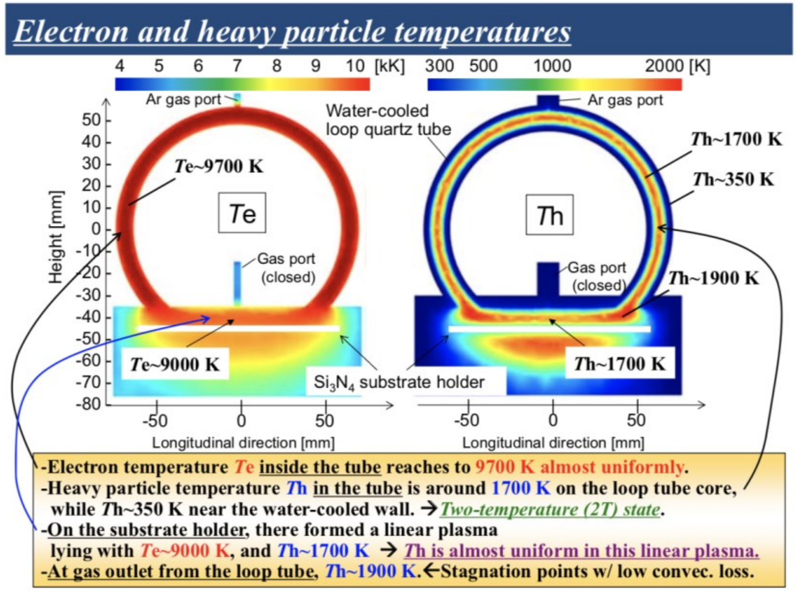

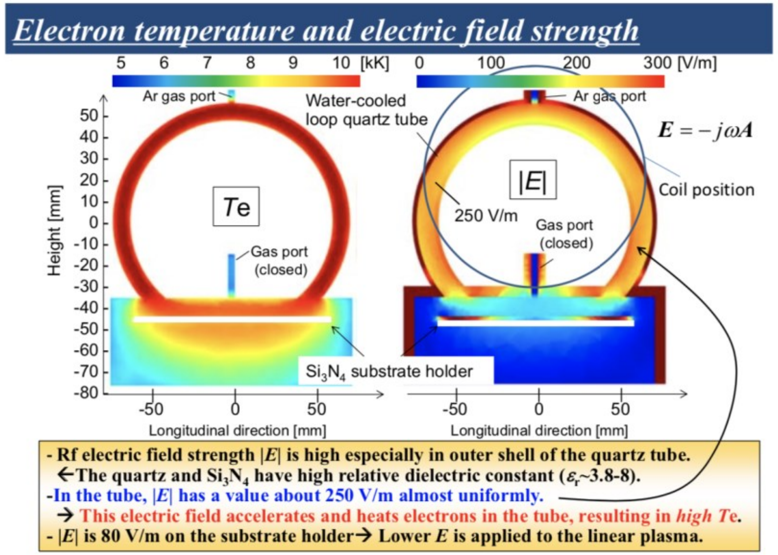

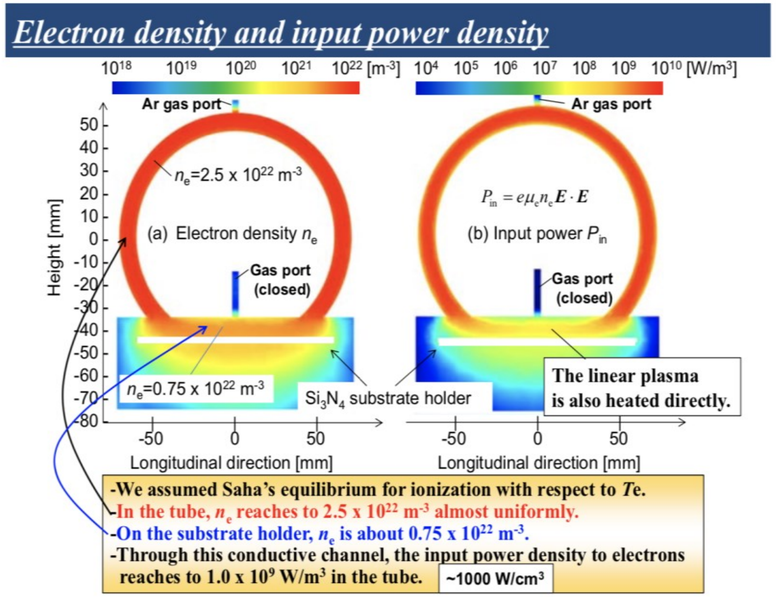

Résultats du modèle:

- T_e proche de 9700K dans le tube, uniformément
- T_h proche de 1700K dans le tube, 350K bord du tube (2T state)
- Sur le substrat : plasma linéaire formé : T_e=9000K
- E dans le tube proche de 250V/m uniforme, 80V/m sur le substrat
- N_e proche de $2.5.10^{22} m^{-3}$, uniforme, $7.5.10^{21} m^{-3}$ sur le substrat
- Température uniforme en surface

POSTERS

Three dimensional nonequilibrium numerical simulation of anode region of high intensity transferred arc

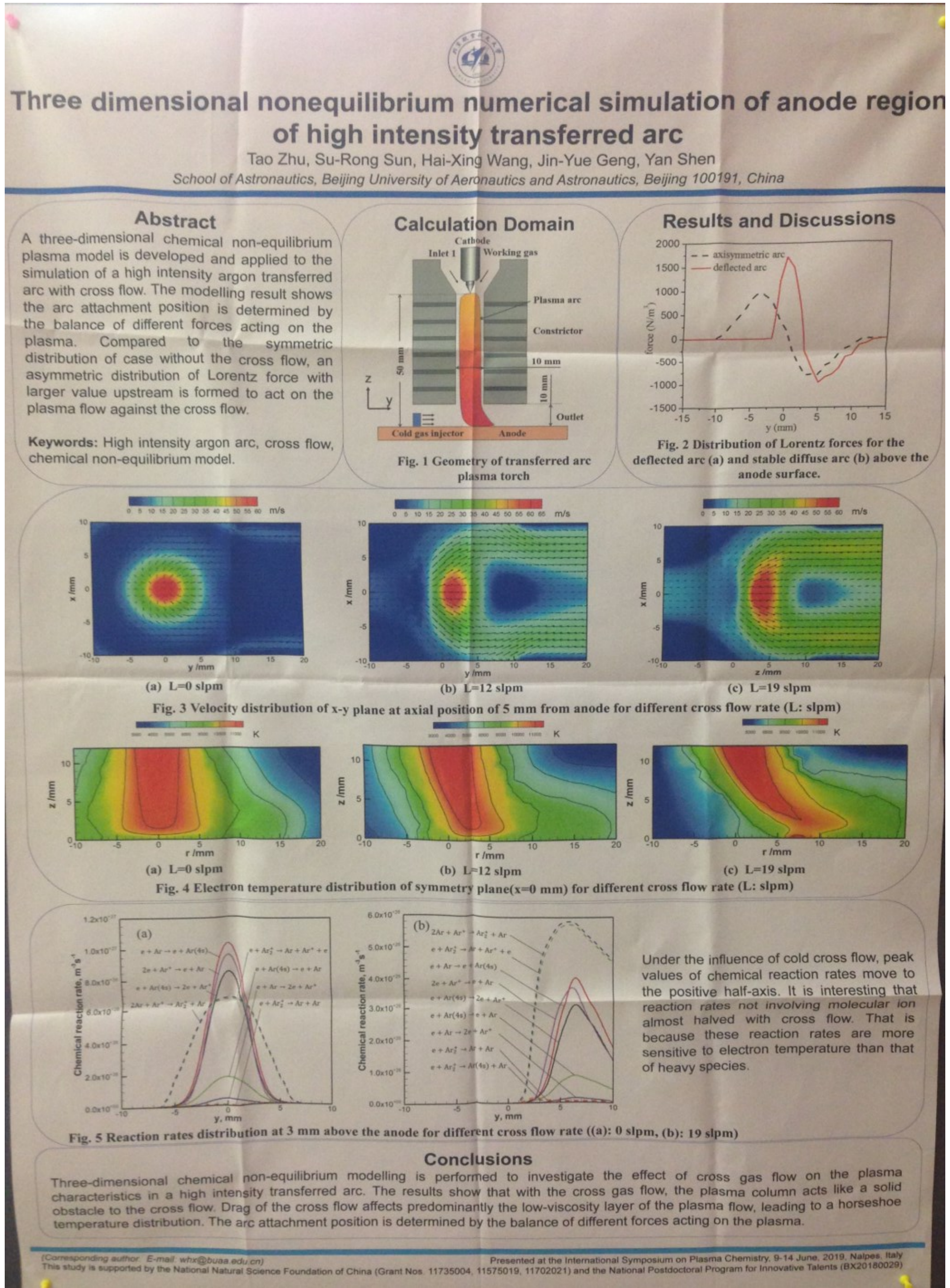

Three dimensional nonequilibrium numerical simulation of anode region of high intensity transferred arc

Tao Zhu, Su-Rong Sun, Hai-Xing Wang, Jin-Yue Geng, Yan Shen

School of Astronautics, Beijing University of Aeronautics and Astronautics, Beijing 100191, China

Abstract

A three-dimensional chemical non-equilibrium plasma model is developed and applied to the simulation of a high intensity argon transferred arc with cross flow. The modelling result shows the arc attachment position is determined by the balance of different forces acting on the plasma. Compared to the symmetric distribution of case without the cross flow, an asymmetric distribution of Lorentz force with larger value upstream is formed to act on the plasma flow against the cross flow.

Keywords: High intensity argon arc, cross flow, chemical non-equilibrium model.

Calculation Domain

Fig. 1 Geometry of transferred arc plasma torch

Results and Discussions

Fig. 2 Distribution of Lorentz forces for the deflected arc (a) and stable diffuse arc (b) above the anode surface.

(a) L=0 slpm (b) L=12 slpm (c) L=19 slpm

Fig. 3 Velocity distribution of x-y plane at axial position of 5 mm from anode for different cross flow rate (L: slpm)

(a) L=0 slpm (b) L=12 slpm (c) L=19 slpm

Fig. 4 Electron temperature distribution of symmetry plane(x=0 mm) for different cross flow rate (L: slpm)

Under the influence of cold cross flow, peak values of chemical reaction rates move to the positive half-axis. It is interesting that reaction rates not involving molecular ion almost halved with cross flow. That is because these reaction rates are more sensitive to electron temperature than that of heavy species.

Fig. 5 Reaction rates distribution at 3 mm above the anode for different cross flow rate ((a): 0 slpm, (b): 19 slpm)

Conclusions

Three-dimensional chemical non-equilibrium modelling is performed to investigate the effect of cross gas flow on the plasma characteristics in a high intensity transferred arc. The results show that with the cross gas flow, the plasma column acts like a solid obstacle to the cross flow. Drag of the cross flow affects predominantly the low-viscosity layer of the plasma flow, leading to a horseshoe temperature distribution. The arc attachment position is determined by the balance of different forces acting on the plasma.

(Corresponding author. E-mail: whx@buaa.edu.cn)

Presented at the International Symposium on Plasma Chemistry, 9-14 June, 2019, Nalpes, Italy

This study is supported by the National Natural Science Foundation of China (Grant Nos. 11735004, 11575019, 11702021) and the National Postdoctoral Program for Innovative Talents (BX20180029)

High-speed vizualization of temperature fluctuation in multiphase AC arc

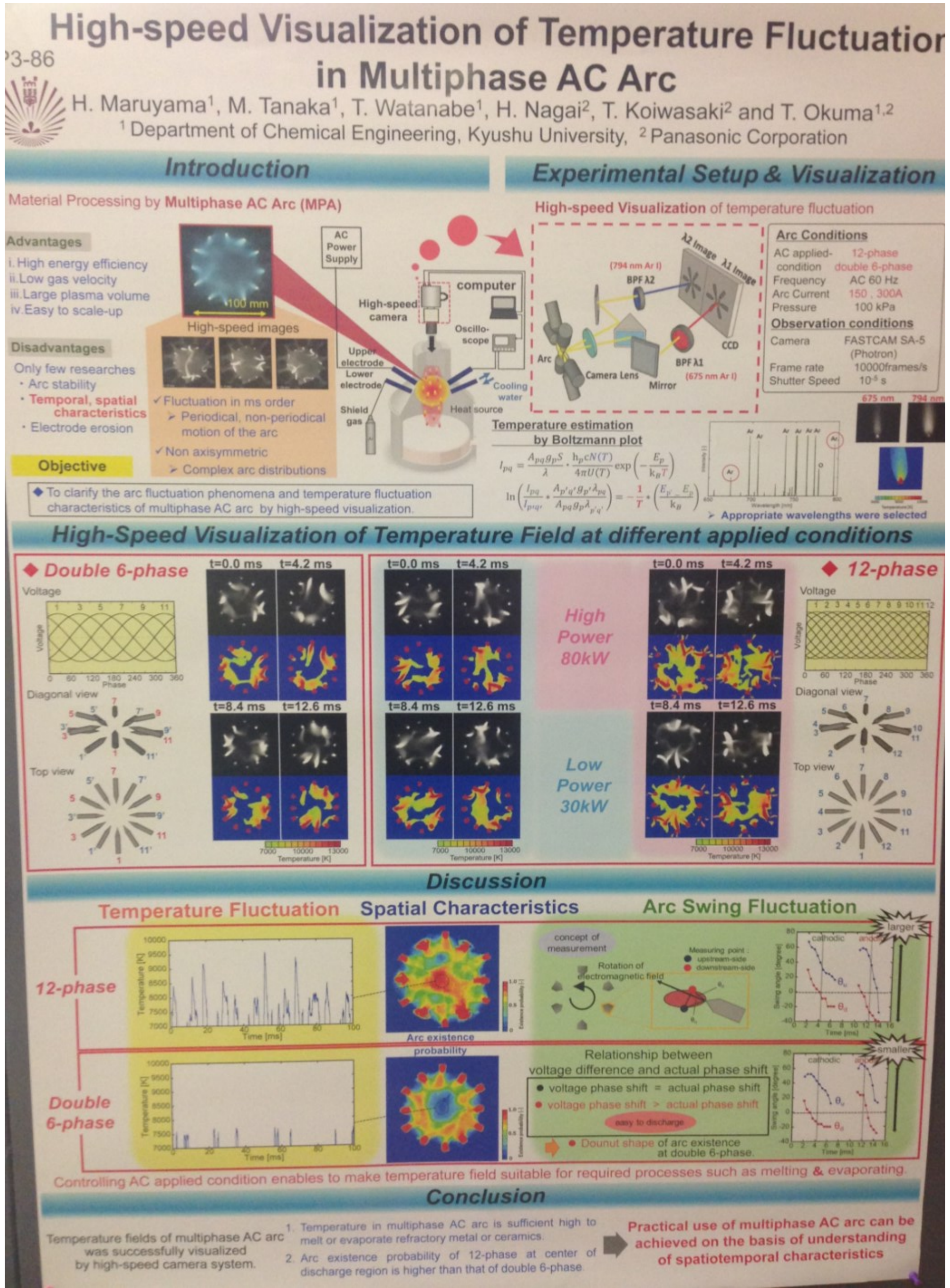

Visualisation of electrode phenomena in nitrogen DC arc

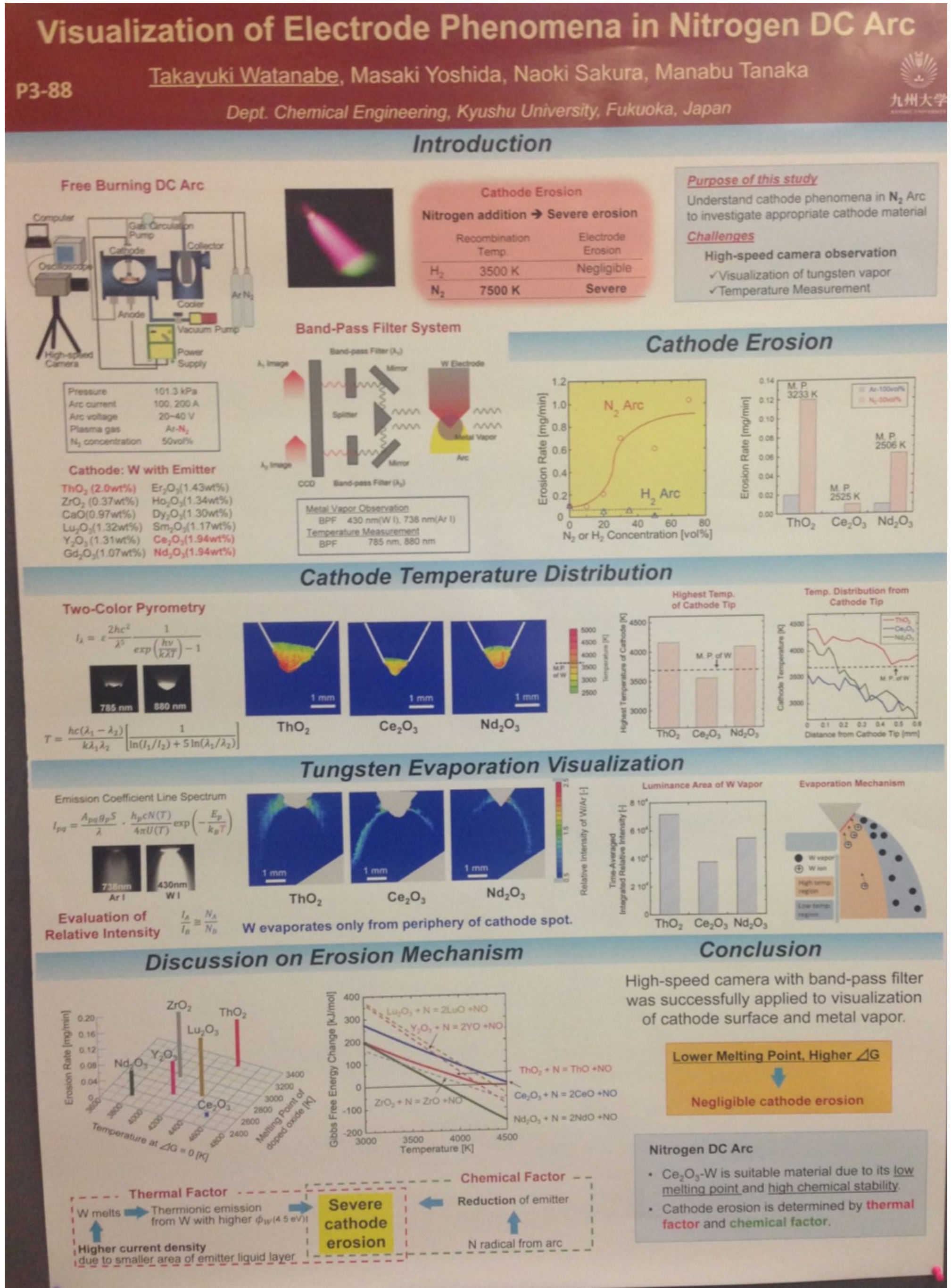

Development of a novel swirl flow induced rotating arc discharge reactor for CO_2 conversion

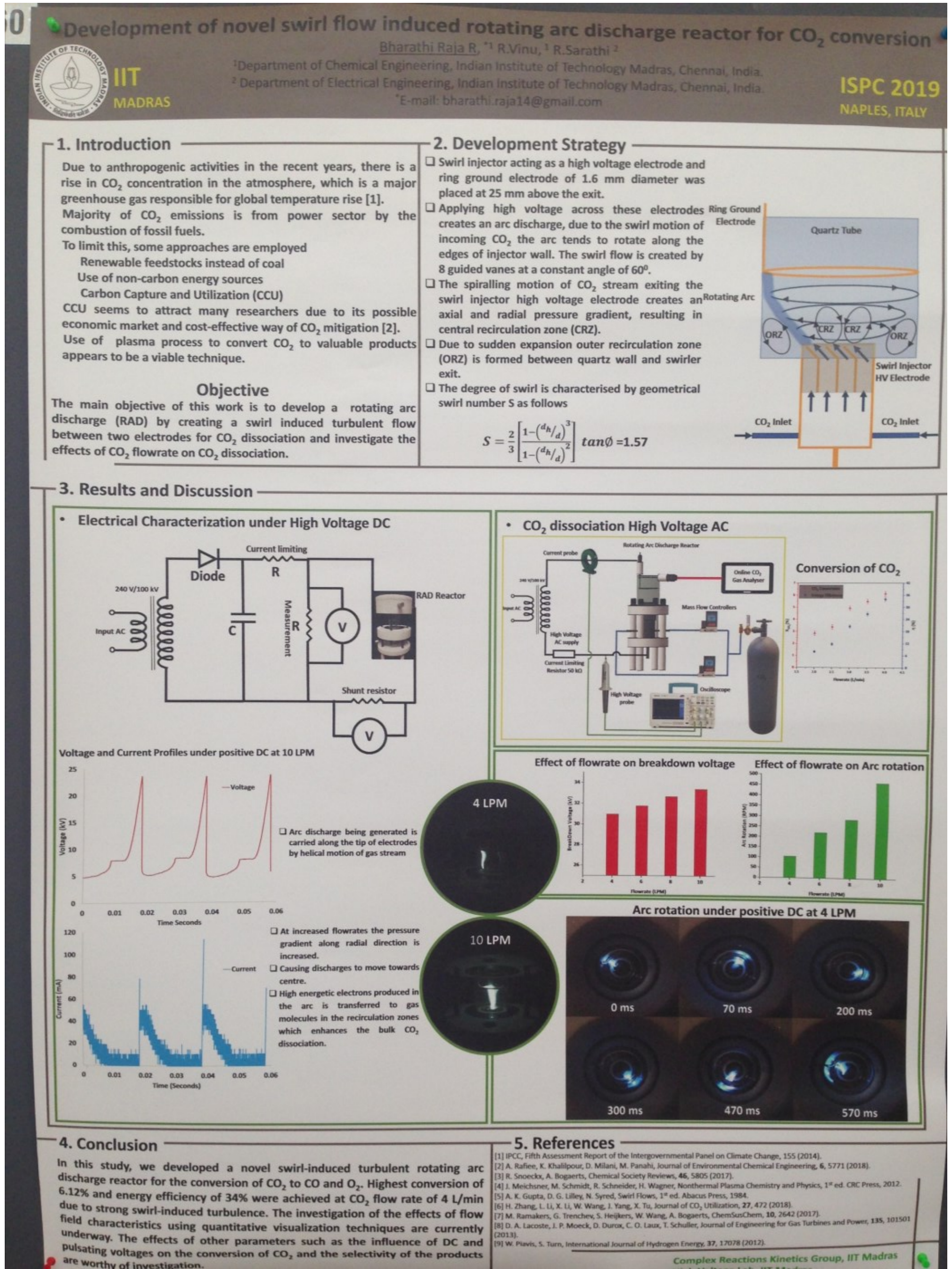

Atmospheric pressure radio frequency hydrogen induction TP diagnostics by OES

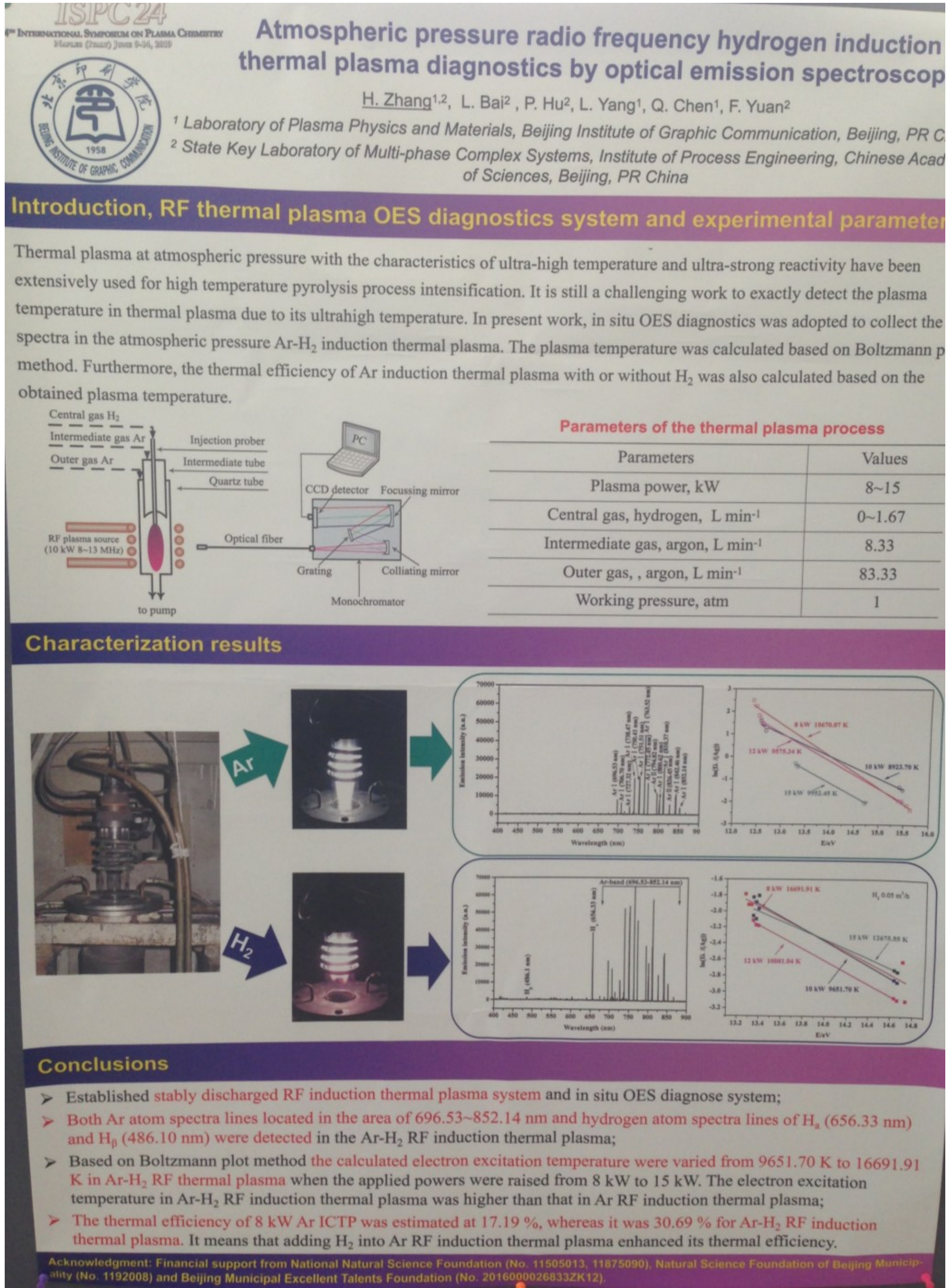

ISPC 24
24th International Symposium on Plasma Chemistry
Naples (Italy) June 9-14, 2019

Atmospheric pressure radio frequency hydrogen induction thermal plasma diagnostics by optical emission spectroscop

H. Zhang[1,2], L. Bai[2], P. Hu[2], L. Yang[1], Q. Chen[1], F. Yuan[2]

[1] Laboratory of Plasma Physics and Materials, Beijing Institute of Graphic Communication, Beijing, PR C

[2] State Key Laboratory of Multi-phase Complex Systems, Institute of Process Engineering, Chinese Acad of Sciences, Beijing, PR China

Introduction, RF thermal plasma OES diagnostics system and experimental parameter

Thermal plasma at atmospheric pressure with the characteristics of ultra-high temperature and ultra-strong reactivity have been extensively used for high temperature pyrolysis process intensification. It is still a challenging work to exactly detect the plasma temperature in thermal plasma due to its ultrahigh temperature. In present work, in situ OES diagnostics was adopted to collect the spectra in the atmospheric pressure Ar-H_2 induction thermal plasma. The plasma temperature was calculated based on Boltzmann p method. Furthermore, the thermal efficiency of Ar induction thermal plasma with or without H_2 was also calculated based on the obtained plasma temperature.

Parameters of the thermal plasma process

Parameters	Values
Plasma power, kW	8~15
Central gas, hydrogen, L min^{-1}	0~1.67
Intermediate gas, argon, L min^{-1}	8.33
Outer gas, , argon, L min^{-1}	83.33
Working pressure, atm	1

Characterization results

Conclusions

- Established stably discharged RF induction thermal plasma system and in situ OES diagnose system;
- Both Ar atom spectra lines located in the area of 696.53~852.14 nm and hydrogen atom spectra lines of H_α (656.33 nm) and H_β (486.10 nm) were detected in the Ar-H_2 RF induction thermal plasma;
- Based on Boltzmann plot method the calculated electron excitation temperature were varied from 9651.70 K to 16691.91 K in Ar-H_2 RF thermal plasma when the applied powers were raised from 8 kW to 15 kW. The electron excitation temperature in Ar-H_2 RF induction thermal plasma was higher than that in Ar RF induction thermal plasma;
- The thermal efficiency of 8 kW Ar ICTP was estimated at 17.19 %, whereas it was 30.69 % for Ar-H_2 RF induction thermal plasma. It means that adding H_2 into Ar RF induction thermal plasma enhanced its thermal efficiency.

Acknowledgment: Financial support from National Natural Science Foundation (No. 11505013, 11875090), Natural Science Foundation of Beijing Municipality (No. 1192008) and Beijing Municipal Excellent Talents Foundation (No. 2016000026833ZK12).

The on-going development of a CFD model to better understand the plasma arc discharge in a waste-water treatment application

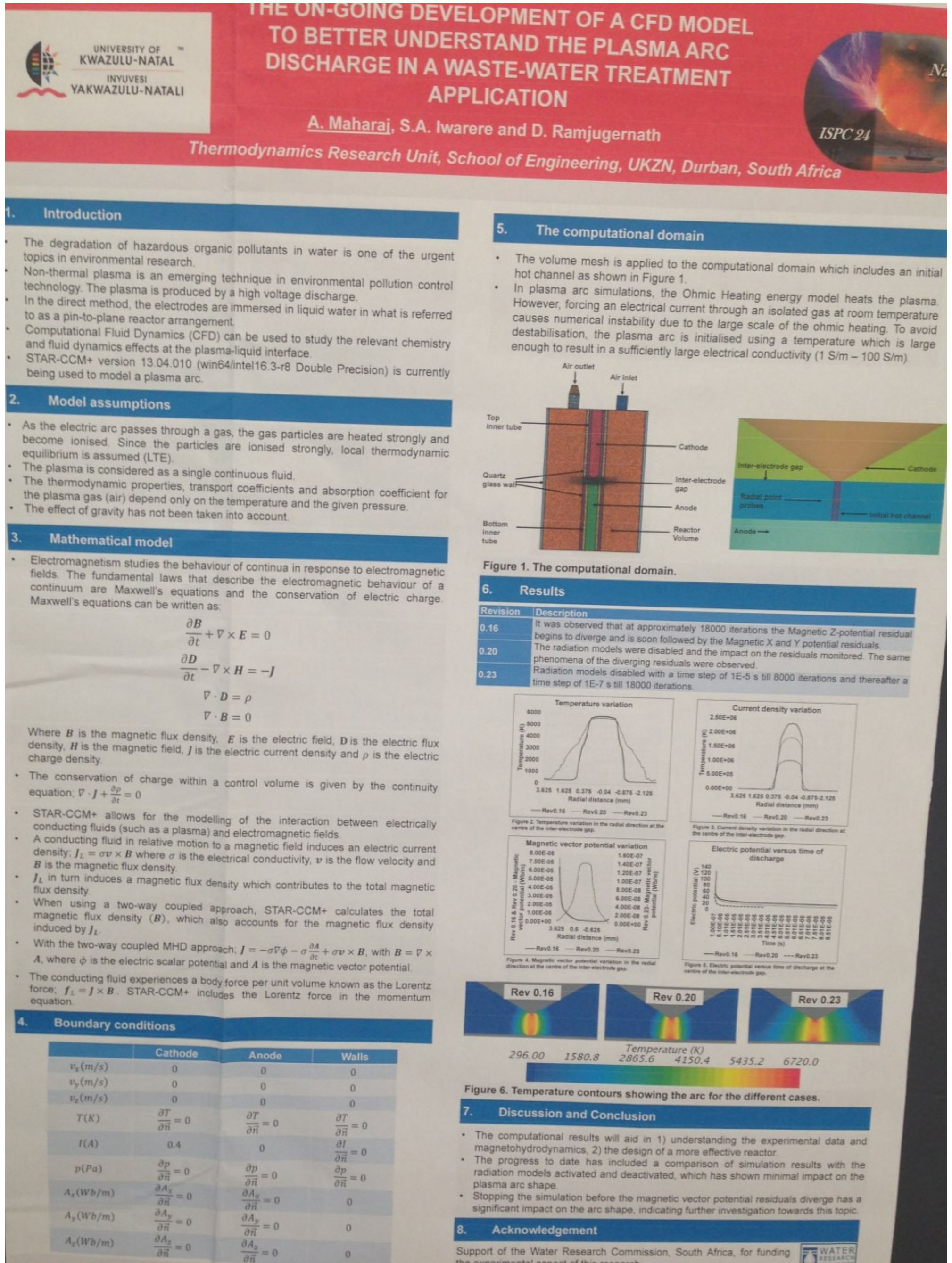

Non-equilibrium transport processes in a free-burning argon arc plasma under different operating pressures

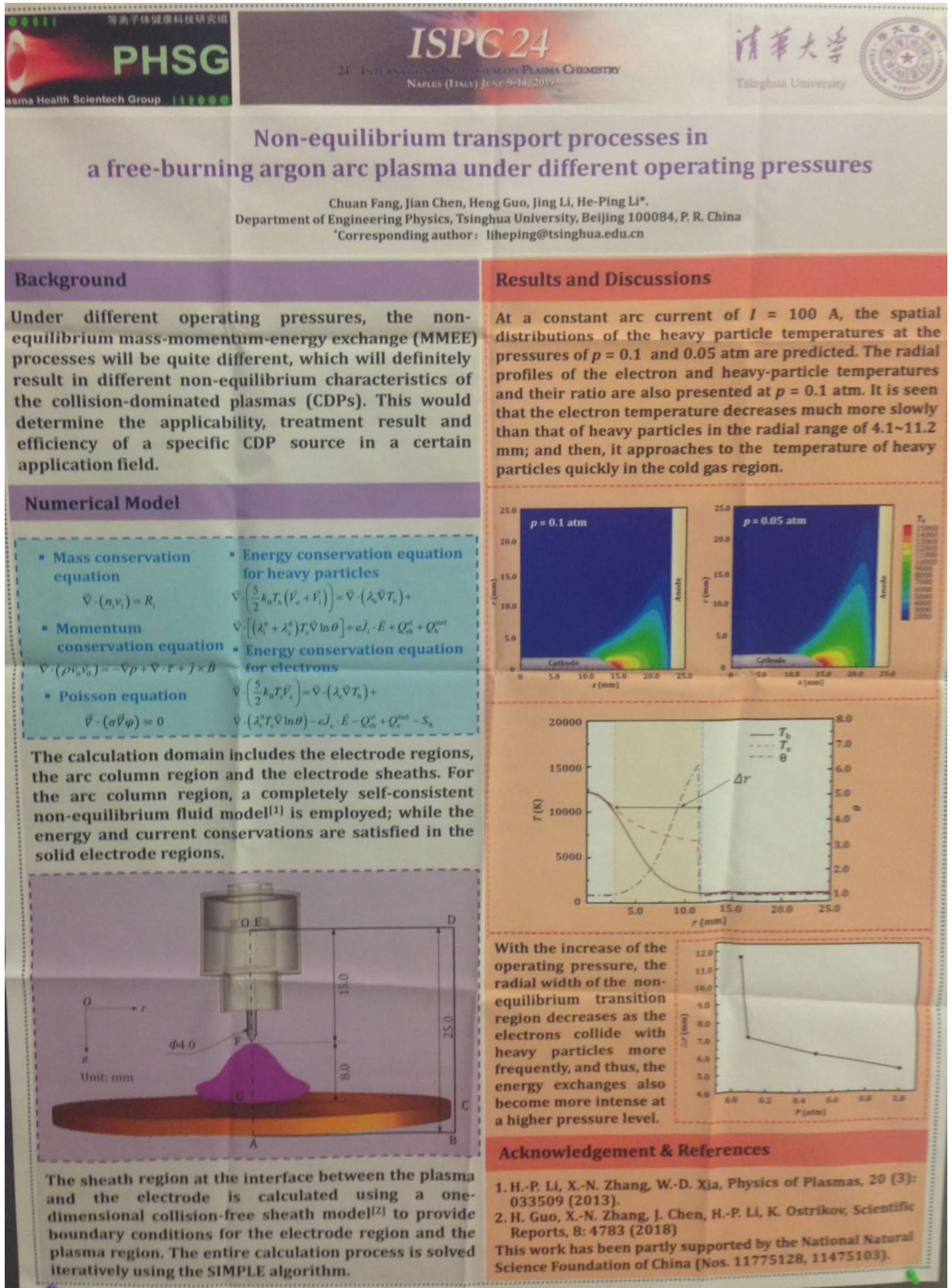

RF plasma for environmental and agriculture applications

3D modelling of a DC transferred arc twin torch plasma system for the synthesis of copper nanoparticules

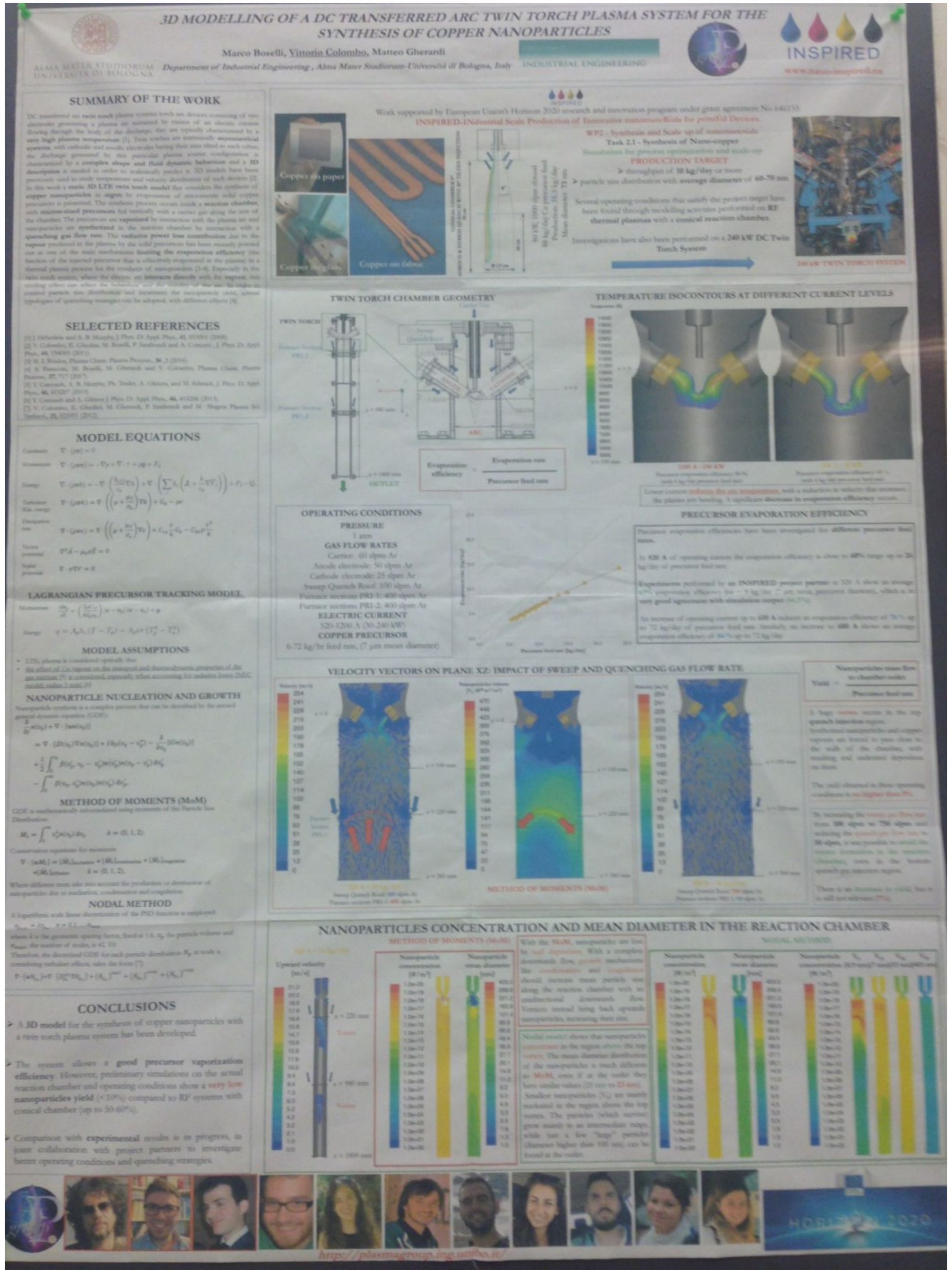

Synthesis of aluminium nitride nano-powder using IP technology: effect of feedstock molar ratio and reactor pressure

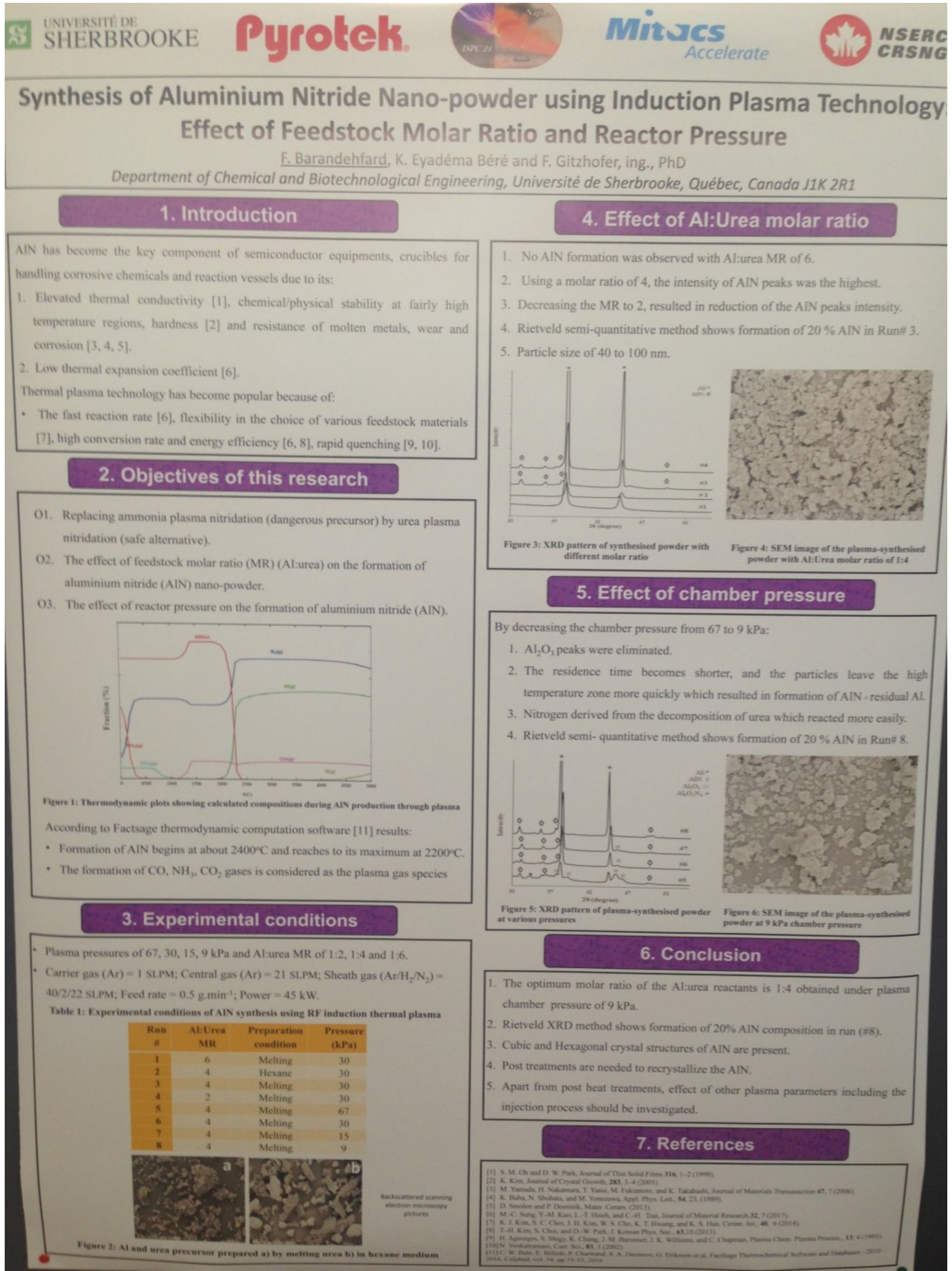

UNIVERSITÉ DE SHERBROOKE · Pyrotek · ISPC 24 · Mitacs Accelerate · NSERC CRSNG

Synthesis of Aluminium Nitride Nano-powder using Induction Plasma Technology: Effect of Feedstock Molar Ratio and Reactor Pressure

F. Barandehfard, K. Eyadéma Béré and F. Gitzhofer, ing., PhD
Department of Chemical and Biotechnological Engineering, Université de Sherbrooke, Québec, Canada J1K 2R1

1. Introduction

AlN has become the key component of semiconductor equipments, crucibles for handling corrosive chemicals and reaction vessels due to its:

1. Elevated thermal conductivity [1], chemical/physical stability at fairly high temperature regions, hardness [2] and resistance of molten metals, wear and corrosion [3, 4, 5].
2. Low thermal expansion coefficient [6].

Thermal plasma technology has become popular because of:

- The fast reaction rate [6], flexibility in the choice of various feedstock materials [7], high conversion rate and energy efficiency [6, 8], rapid quenching [9, 10].

2. Objectives of this research

O1. Replacing ammonia plasma nitridation (dangerous precursor) by urea plasma nitridation (safe alternative).

O2. The effect of feedstock molar ratio (MR) (Al:urea) on the formation of aluminium nitride (AlN) nano-powder.

O3. The effect of reactor pressure on the formation of aluminium nitride (AlN).

Figure 1: Thermodynamic plots showing calculated compositions during AlN production through plasma

According to Factsage thermodynamic computation software [11] results:

- Formation of AlN begins at about 2400°C and reaches to its maximum at 2200°C.
- The formation of CO, NH_3, CO_2 gases is considered as the plasma gas species

3. Experimental conditions

- Plasma pressures of 67, 30, 15, 9 kPa and Al:urea MR of 1:2, 1:4 and 1:6.
- Carrier gas (Ar) = 1 SLPM; Central gas (Ar) = 21 SLPM; Sheath gas ($Ar/H_2/N_2$) = 40/2/22 SLPM; Feed rate = 0.5 $g.min^{-1}$; Power = 45 kW.

Table 1: Experimental conditions of AlN synthesis using RF induction thermal plasma

Run #	Al:Urea MR	Preparation condition	Pressure (kPa)
1	6	Melting	30
2	4	Hexane	30
3	4	Melting	30
4	2	Melting	30
5	4	Melting	67
6	4	Melting	30
7	4	Melting	15
8	4	Melting	9

Backscattered scanning electron microscopy pictures

Figure 2: Al and urea precursor prepared a) by melting urea b) in hexane medium

4. Effect of Al:Urea molar ratio

1. No AlN formation was observed with Al:urea MR of 6.
2. Using a molar ratio of 4, the intensity of AlN peaks was the highest.
3. Decreasing the MR to 2, resulted in reduction of the AlN peaks intensity.
4. Rietveld semi-quantitative method shows formation of 20 % AlN in Run# 3.
5. Particle size of 40 to 100 nm.

Figure 3: XRD pattern of synthesised powder with different molar ratio

Figure 4: SEM image of the plasma-synthesised powder with Al:Urea molar ratio of 1:4

5. Effect of chamber pressure

By decreasing the chamber pressure from 67 to 9 kPa:

1. Al_2O_3 peaks were eliminated.
2. The residence time becomes shorter, and the particles leave the high temperature zone more quickly which resulted in formation of AlN - residual Al.
3. Nitrogen derived from the decomposition of urea which reacted more easily.
4. Rietveld semi- quantitative method shows formation of 20 % AlN in Run# 8.

Figure 5: XRD pattern of plasma-synthesised powder at various pressures

Figure 6: SEM image of the plasma-synthesised powder at 9 kPa chamber pressure

6. Conclusion

1. The optimum molar ratio of the Al:urea reactants is 1:4 obtained under plasma chamber pressure of 9 kPa.
2. Rietveld XRD method shows formation of 20% AlN composition in run (#8).
3. Cubic and Hexagonal crystal structures of AlN are present.
4. Post treatments are needed to recrystallize the AlN.
5. Apart from post heat treatments, effect of other plasma parameters including the injection process should be investigated.

7. References

The effect of H2 on the transport of graphene to amorphous carbon by DC arc discharge

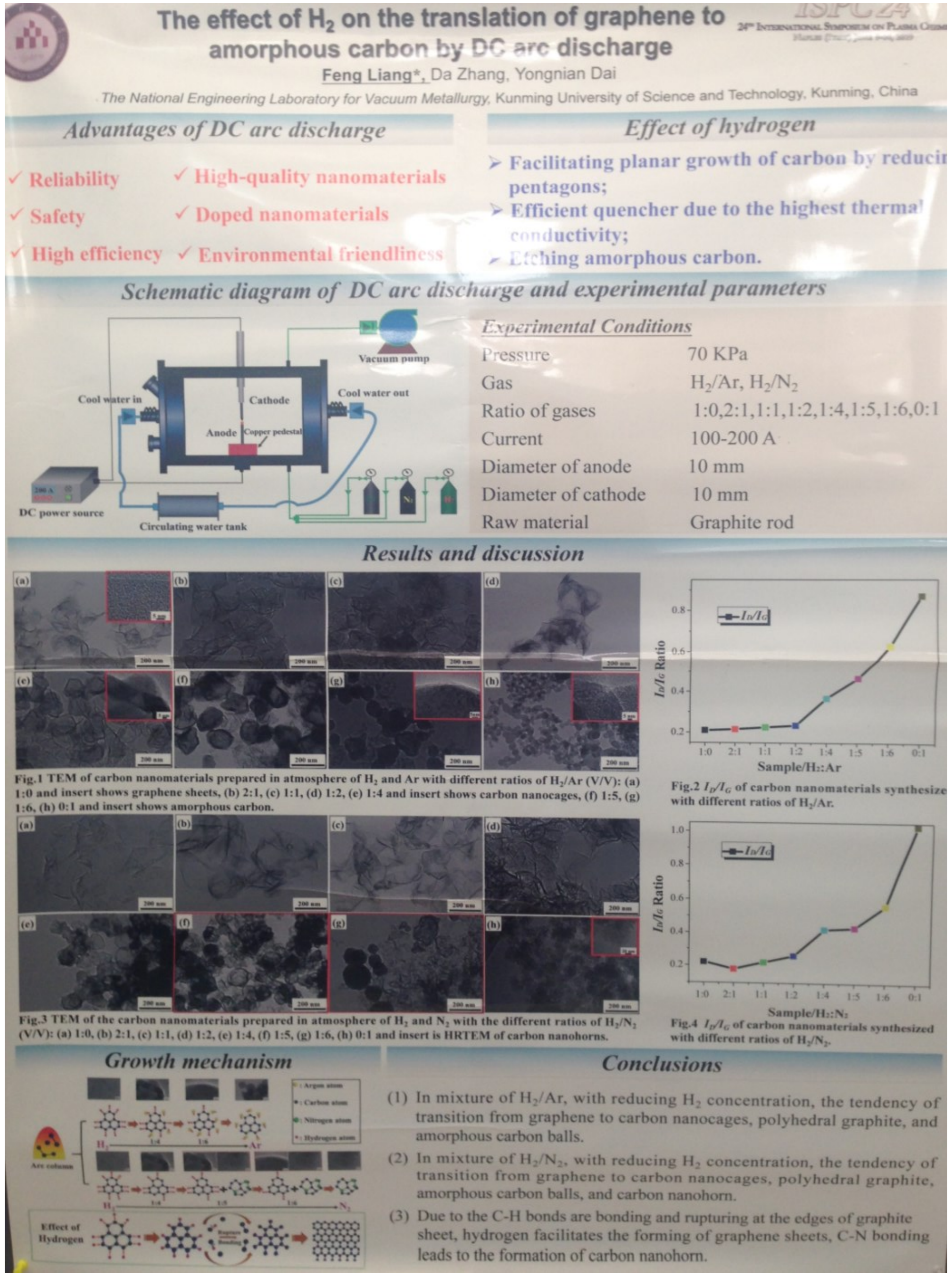

Formation mechanism of carbon-coated amorphous Si nanoparticules synthetized by induction thermal plasmas

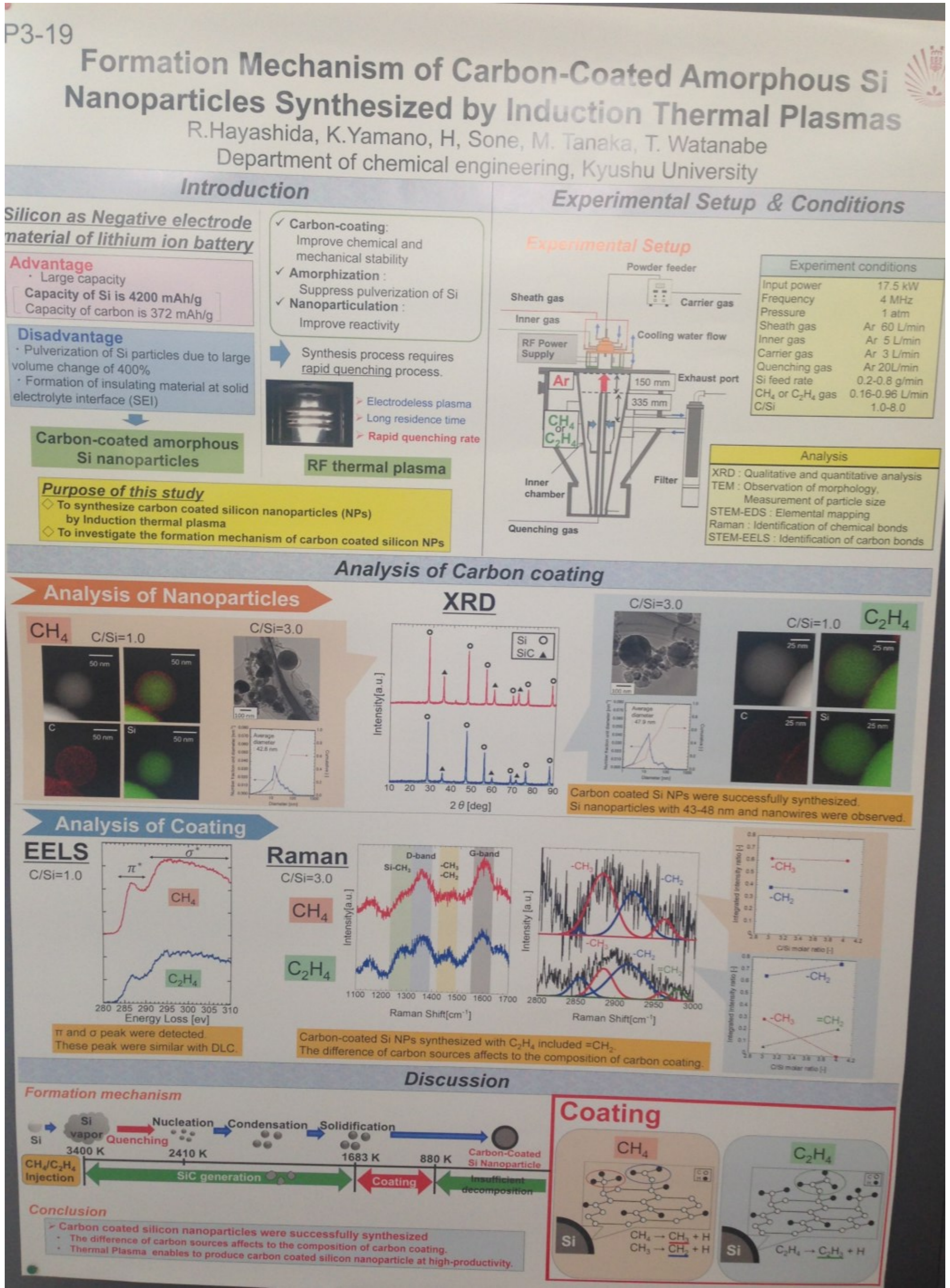

Synthesis of Lithium oxide composite with refractory metal by induction thermal plasmas

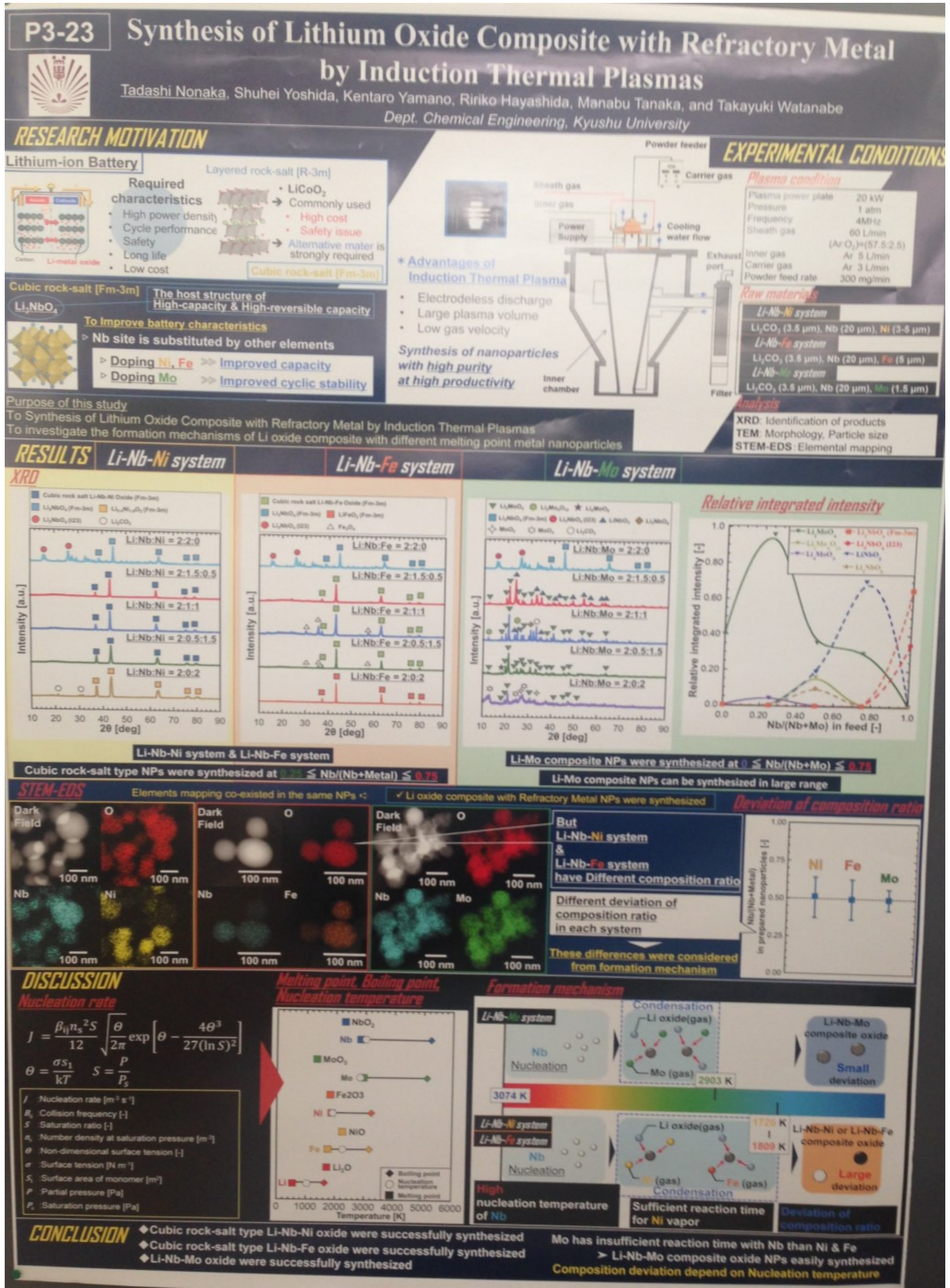

P3-43

Synthesis of Transition Metal Boride Nanoparticles by Induction Thermal Plasma

L. Liu, Y. Tanoue, T. Nonaka, M. Tanaka and T. Watanabe*

Department of Chemical Engineering, Faculty of Engineering, Kyushu University, 744 Motooka, Nishi-ku, Fukuoka 819-0395, Japan

Introduction

Transition metal (Mo & W) boride (TMB)

Advantages

- High hardness,
- Thermal and electric conductivity,
- High wear and corrosion resistance,
- Radiation shielding performance.

Difficulties — Conventional methods

- Hard to produce refractory metal boride
- Difficult manufacturing process
- Production efficiency
- Oxidation problem
- Synthesis of TMB nanoparticles

Induction Thermal Plasma

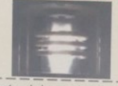

- Electrodeless plasma
- Long residence time
- large high temperature area

✓ High purity of TMB nanoparticles at high productivity

Purpose of this study

I. Investigate the formation mechanism

II. Apply to large-scale industrial production

Experimental Setup and Conditions

Experimental Setup

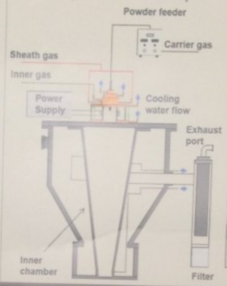

Experimental condition

Plasma power [kW]:	20
RF frequency [MHz]:	4
Operation pressure [atm]:	1
Sheath gas flow rate Ar [L/min]:	60
Inner gas flow rate Ar [L/min]:	5
Carrier gas flow rate Ar [L/min]:	3
Powder feed rate [mg/min]:	300
Composition:	(Mo or W):B= 1:0.5, 1:1, 1:2, 1:2.5, 1:4, 1:6

Analysis methods

XRD: Identification of products

STEM-EDS: Elements mapping

Result

I. Mo-B system

XRD

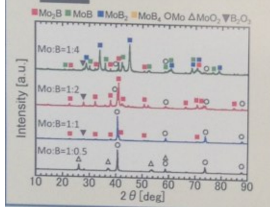

Relative integrated intensity of each product

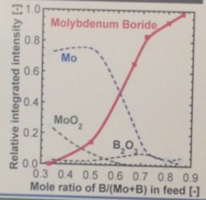

STEM-EDS

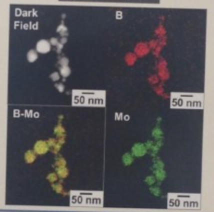

Mean diameter of nanoparticles

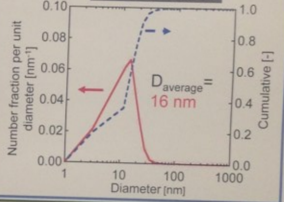

II. W-B system

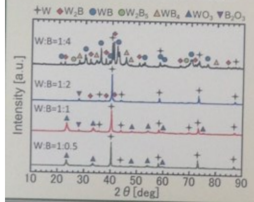

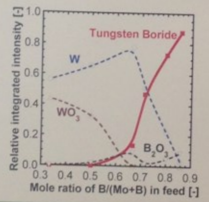

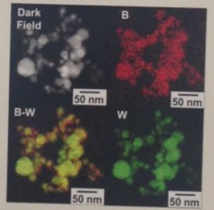

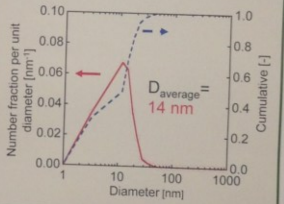

Discussion

Nucleation temperature

$$J = \frac{\beta_{ij} n_s^2 S}{12}\sqrt{\frac{\Theta}{2\pi}}\exp\left[\Theta - \frac{4\Theta^3}{27(\ln S)^2}\right],$$

$$S = \frac{P_1}{P_s}, \quad \Theta = \frac{\sigma s_1}{kT}$$

J: homogeneous nucleation rate [$m^{-3}\cdot s^{-1}$]

Θ: dimensionless surface tension [-]

S: saturation ratio [-]

β_{ij}: collision frequency function between monomers [-]

n_s: equilibrium saturation monomer concentration [m^{-3}]

◆ Melting Point, Boiling Point and Nucleation Temperature

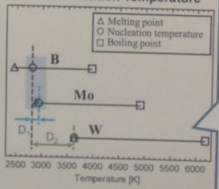

◆ Nucleation Temperature Difference (D_1 & D_2) between metal and B

Mo and B	W and B
□ Small difference	□ large difference
well-mixed Mo and B vapors	W has started to solidify before B vapors condense
efficient reaction	difficult reaction
better preparation of thermodynamically stable phases	far deviation from the thermodynamically phases

◆ Product phases and expected product phases according to the phase diagram

	Molar ratio	Main product	Expected product
W-B system	1:0.5	W	W_2B, W
	1:1	W	WB, W_2B_5
	1:2	W, W_2B	WB, W_2B_5
	1:4	W_2B, WB, WB_4, W_2B_5, W	W_2B_5, WB_4, B
Mo-B system	1:0.5	Mo	Mo_2B, Mo
	1:1	Mo, Mo_2B	MoB, Mo_2B, Mo
	1:2	Mo_2B, MoB_2, Mo	MoB_2, Mo_2B_5, MoB_4, B
	1:4	MoB_2, MoB, Mo_2B, Mo	Mo_2B_5, MoB_4, B

Formation mechanism

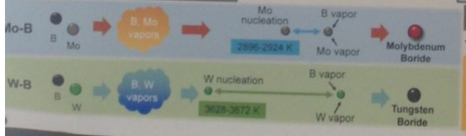

Conclusion

TMB nanoparticles were successfully synthesized by induction thermal plasma.

- Mo and B react more easily than W and B. The products of W-B system showed greater deviation from the phase diagram.
- Induction thermal plasma can provide a high efficient way to synthesize TMB nanoparticles to apply to large-scale industrial production.

Synthesis of Few-walled Boron Nitride Nanotubes using Triple Thermal Plasma Jet System with Hydrogen Injection

Minseok Kim[a], J.-H. Oh[a], B. I. Min[1], Y. H. Lee[1] S. H. Hong[1], T.-H. Kim[2*], and S. Choi[1,2*]

[1] Department of Nuclear and Energy Engineering, Jeju National University, Jeju 63243, Republic of Korea
[2] Institute for Nuclear Science and Technology, Jeju National University, Jeju 63243, Republic of Korea

Introduction

1994 years

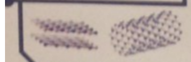

Firstly proposed

- Boron Nitride Nano Tubes(BNNT) might be formed from hexagonal boron nitride(BN) [1].

1995 years

Firstly synthesized

- BNNTs are synthesized for the first time by Zettl and coworkers [2].

1998 ~ 2004 years

1. *Young's modulus* = $\frac{Stress}{Strain}$
2. *Thermal stability*
3. *Oxidation resistivity*

Filing various properties

- Wide band gap > 5 eV.
- The elastic Young's modulus of BNNT over 1 Tpa.
- It was revealed BNNTs are stable at 700 °C in air.
- It was demonstrated an onset temperature for oxidation of BNNTs is 800 °C.

2009 years

A noteworthy advance

- Ultrafine BNNT were produced using laser ablation.
- The production rate was 60 mg of BNNTs during 30 minutes.

2014 years

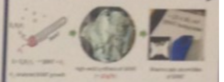

Impressive BNNT mass production

- Highly crystalline small diameter BNNT are synthesized and at an unprecedentedly high rate approaching 20 g/h without for metal catalysts.

HYPOTHESIS AND SYNTHESIZE → PROPERTIES → MASS PRODUCTION (PRESENT GOAL)

Experimental set up

Experimental Set-up

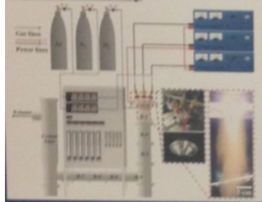

Experimental Condition

	Experiments
Chamber pressure [kPa]	Atmospheric pressure
Plasma forming gas [slpm]	4 (Ar) and 8(N_2)
Carrier gas [slpm]	5 (Ar)
Reactant gas [slpm]	8 (H_2)
Arc current [A]	100
Arc voltage [V]	(1) 70 (2) 69 (3) 75
Starting material	B and h-BN

Analysis

Thermal equilibrium equation
➢ HSC Chemistry 9

FE-SEM
➢ MIRA3

FE-TEM
➢ JEM-2100F

Hypothesized Chemical Path to be Grown into BNNT

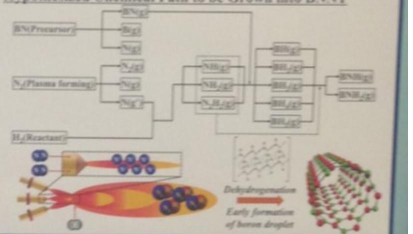

Results and Discussion

The results of thermodynamic equilibrium calculation

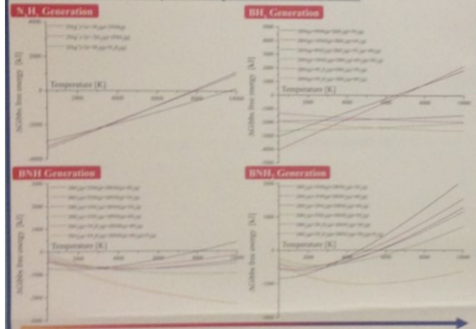

Super heating area

- ➢ The nitrogen molecules are circumstanced in the **strong electrical field** which is **sufficient to ionize** them.
- ➢ The formed radicals react with hydrogen molecules **to produce N_xH_y gases**.

Quenching area

- ➢ In the process of quenching, the formed N_xH_y gases combine with BN gases **to form assorted BH gases**.
- ➢ Among the BH gases, BH_2 and BH_3 gases continuously combine with N_xH_y gases during the cooling process **to form BNH and BNH_2 gases**.

The macroscopic, SEM, and TEM images of the formed BNNT

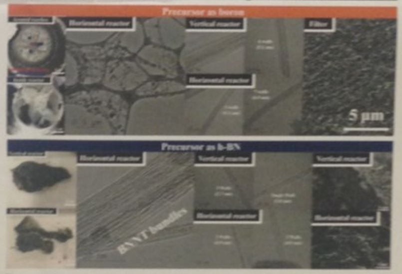

Comparison with other works

Method	Input power(kW)	Production rate(g/h)	Production rate per power(g/h kW)	Injection gas(SLPM)	Production rate per nitrogen gases(g/h SLPM)	Reference
Laser ablation	1	0.12	0.12	-	-	Smith, M. W. et al
Chemical vapor deposition	-	0.016	-	Ar: 0.3, NH_3: 0.2	0.08	Huang, Y. et al
Induction thermal plasma	60	20	0.33	Ar: 75, H_2: 20, N_2: 55	0.36	Kim, K. S. et al
Induction thermal plasma	40	35	0.875	N_2: 50	0.7	Fathalizadeh, A. et al
Triple DC thermal plasma	20	12.6	0.63	Ar: 12, H_2: 8, N_2: 24	0.525	Present work

※ The price of BNNTs is up to 1,350 $/g from Sigma Aldrich as of May 2019

Conclusion

IMPORTANT **Triple DC thermal plasma jet provides appropriate environment for synthesis of BNNT with hydrogen**

- The N_2 gas as plasma forming gas was circumstanced in the **strong electrical field** which is **sufficient to ionize** them, which leads **forming N_xH_y gases with H_2 gas** in plasma flame.
- The formed **NxHy gases reacts with BN gas** as precursor to generate **B-N-H intermediates** which are **eventually grown into BNNT**.

IMPORTANT **The thin cotton appearance material in macroscopic scale was successfully formed and validated for BNNT**

- The TEM analysis validated the fabric material from the reactors **has highly crystalline tubular structures which are straight and parallel** to the axis of the tube, and these tubular structure have **diameters below 5 nm without drawback**.
- As a result, **12.6 g of the BNNT** was produced with input power of 21.4 kW, which was **a superior yield**.

ISPC24

Synthesis of Si-MWCNT nanocomposite using triple DC thermal plasma jet system

Seung-Hyun Hong[1], Tae-Hee Kim[2], Jeong-Hwan Oh[1], Minseok Kim[1] and Sooseok Choi[1,2*]
[1] Department of Nuclear and Energy Engineering, Jeju National University, 102 Jejudaehak-ro, Jeju 63243, Republic of Korea
[2] Institute for Nuclear Science and Technology, Jeju National University, 102 Jejudaehak-ro, Jeju 63243, Republic of Korea

Introduction

◆ Li-ion battery

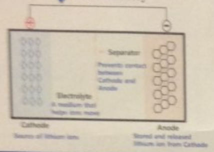

◆ Advantage of silicon as an anode electrode

Materials	Carbon (current anode material)	Silicon
Lithiated phase	LiC_6	$Li_{4.4}Si$
Specific capacity (mAh/g)	372	4200
Volume change (%)	12	420

◆ Role of MWCNT in Si-MWCNT anode material

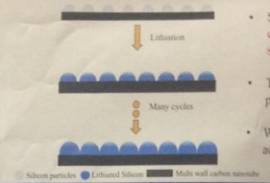

- Silicone anode material has high specific capacity but difficult to commercialize due to significant volume expansion.
- The high tensile strength of MWCNT prevents the volume expansion of silicon.
- We propose synthesis of Si-MWCNT according to the mass ratio.

Experimental set-up

Thermal plasma system used for Si-MWCNT synthesis consists of a power supply, triple plasma torch, powder feeder, reactors and cyclone filter. The mixed powder of micron sized Si and MWCNT was injected into the triple plasma jet as raw material. The detail of experimental condition is presented in the right Table.

Synthesis process using triple DC thermal plasma jet system

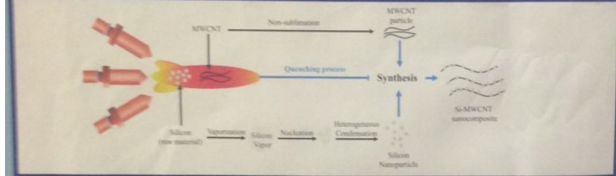

Experimental Condition

Exp. no.	Exp.1	Exp.2	Exp.3
Total input power (kW)	18.6	19.1	19.9
Feeding rate (g/min)	0.32	0.31	0.5
Plasma forming gas (L/min)		N_2 (6), Ar (4)	
Mass ratio of powder (Si : MWCNT)	2 : 1	5 : 1	1 : 2

❖ All experiments were carried out in atmospheric pressure

	Exp. 1	Exp. 2	Exp. 3
Silicon (nm)	62.84	100.67	53.52
MWCNT (nm)	18.09	19.11	20.57

Table 1. Average diameter of synthesized nanomaterial in Exp. 1, 2, and 3.

Results and discussion

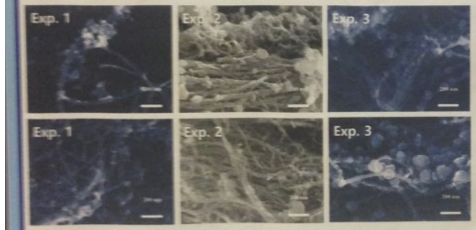

Fig 1. FE-SEM images of synthesized powder in Exp. 1, 2, and 3

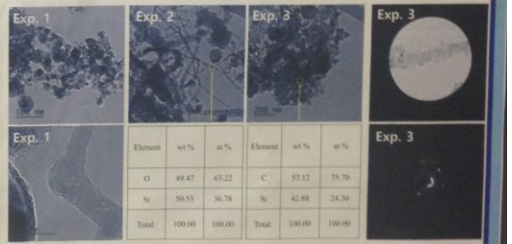

Element	wt %	at %
O	49.47	63.22
Si	50.53	36.78
Total	100.00	100.00

Element	wt %	at %
C	57.12	75.70
Si	42.88	24.30
Total	100.00	100.00

Fig 2. FE-TEM images and SAED patterns of synthesized powder in Exp. 1, 2, and 3. Elemental composition of nanowire (Exp. 2) and nanoparticles (Exp. 3) by EDS analysis

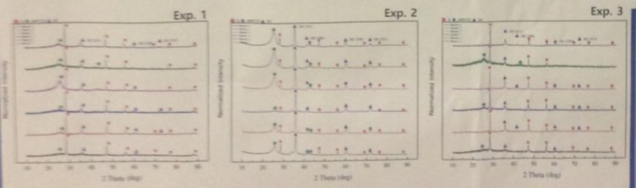

Fig 3. XRD patterns of synthesized product in Exp. 1, 2 and 3 according to the separated reactor.

Summary and future plan

- Si-MWCNT nanocomposite synthesis experiments were conducted according to the mass ratio of Si and MWCNT as raw material.
- For the high mass ratio of MWCNT (Exp. 3), the peak intensity of silicon carbide was strongest in the XRD and Si-MWCNT nanocomposite structure was observed relatively well in FE-SEM analysis.
- When the mass ratio of Silicon was high, large circular silicon particle and silicon nanowire structure are observed and the diameter of the silicon panicles was large. (Exp.1, 2).
- Silicon nanoparticles and MWCNT were mainly observed in FE-TEM analysis. Some MWCNT was sublimated by injection into high temperature and synthesized silicon carbide nanoparticles.
- In order to enhance the synthetic process for Si-MWCNT nanocomposite synthesis, two powder feeding system will be applied to separately introduce the Si and MWCNT powder. Si powder should be injected into the high temperature of plasma flame to evaporate and produce Si nanoparticles, MWCNT should be introduced into relatively low temperature region of plasma jet tail to prevent sublimation and provide active site to nucleate Si.

Pure Silicon Nanoparticle Synthesis using Tandem Type of Induction Thermal Plasmas with Simultaneous Controlled Modulation of Upper- and Lower-Coil Currents

P3-77
ID-57

ISPC24
June 13, 2019
Naples, Italy

[1]Kazuki Onda*, [1]Kotaro Shimizu, [1]Keita Akashi,
[1]Yasunori Tanaka, [1]Yoshihiko Uesugi, [1]Tatsuo Ishijima ([1]Kanazawa University, Japan)
[2]Shiori Sueyasu, [2]Shu Watanabe, [2]Keitaro Nakamura ([2]Nisshin Seifun Group Inc.), e-mail : tanaka@ec.kanazawa-u.ac.jp

1. Introduction

The Induction Thermal Plasma (ITP) is widely used in materials processing from the following advantages;

- Extremely high gas temperature (~10,000 K)
- High density of chemical active species
- Contamination-less process (No electrode discharge)

In addition to the above features, we have developed a pulse-modulated ITP (PMITP) system.

◆ Concept of the pulse-modulated ITP (PMITP)

The PMITP is sustained by amplitude-modulated coil-current.
It can provide a time-varying temperature field in the torch.

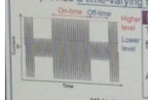

Nanoparticle synthesis
The PMITP was found effective for nanoparticle synthesis.
Our achievement
Al^{3+} doped TiO_2 NPs
~400 g/h@20 kW[1]

[1] N. Kodama, et al. J. Phys. D: Appl. Phys., 47, 195304(2014)

In order to increase production rate of NPs, more heavy load feeding of feedstock is necessary.
However, the PMITP is weak against a large disturbance.
To enhance the stability of the PMITP,

Tandem Type of Modulated Induction Thermal Plasma(tandem-MITP) has been developed

It has two separate coils and two RF power supply.

 # Advantages of the tandem-MITP

1. Complete evaporation of feedstock is expected from its axially long high temperature field.
2. Tempo-spatially varying temperature field can be offered by modulating upper- and lower-coil currents.
3. Stable processing is expected by the two coils:
   - The upper-coil is used to maintain the ITP.
   - The lower-coil is used to obtain a larger varying temperature field.

These advantages can offer more efficient and stable nanoparticle synthesis.

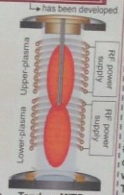

Tandem-MITP

Our previous work Our previous experimental work indicated that the lower-coil current modulation for the tandem-MITP was effective for decreasing the mean diam. of synthesized Si NPs.
Further, the tandem-MITP with two coils provided a higher production rate of NPs than the single MITP using one coil[2].

[2] K. Onda, et al., HTPP15, 5-1(2018)

In this work
Si NPs are expected as promising candidates for an anode of the lithium ion battery.

- Silicon(Si) NPs were synthesized using 'simultaneously' modulated upper- and lower-coil currents of the tandem-MITP.
- The effect of the upper-coil current modulation on diameter and composition of synthesized particles was investigated.

In conclusion
Increasing modulation degree for the upper-coil provides higher quenching of thermal plasma, which decreases the diameter of synthesized particles. Therefore, the 'simultaneous' current modulation of tandem-coils enhances the efficiency of NPs process.

2. Experimental setup

Tandem-ITP +TCFF method

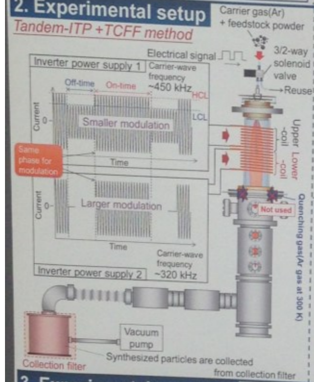

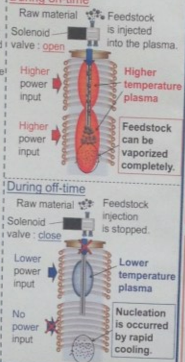

3. Experimental condition

Common conditions

-Time-averaged input power	upper: 10 kW; lower: 10 kW
-Pressure	300 torr
-Sheath gas flow rate	Ar : 90 L/min
-Carrier gas flow rate	Ar : 4 L/min
- Feedstock	Si(97%purity, *mean. diam.* $\bar{d}$ =26 μm)
- Valve open/ close	6 ms/ 9 ms

Modulation conditions

	Cond.(1)	Cond.(2)	Cond.(3)	Cond.(4)	Cond.(5)
Upper-coil current					
-SCL_{upper}	100%	100%	90%	80%	70%
-On/Off-time$_u$	10 ms/ 5 ms				
Lower-coil current					
-SCL_{lower}	100%	0%	0%	0%	0%
-On/Off-time$_l$	10 ms/ 5 ms				
Feeding rate(g/min)	2.80	1.51	2.99	2.93	2.64

Definition of modulation degree SCL

$$SCL[\%] = \frac{\text{Lower current level (LCL)[A]}}{\text{Higher current level (HCL)[A]}}$$

Note: 0%SCL is most high modulation degree, which corresponds to zero current amplitude during off-time.

The solenoid valve was controlled for feedstock to be synchronically supplied into the MITP just during on-time.

Quenching gas was *not used* for fundamental study.

Solenoid valve

4. Experimental results for nanoparticle synthesis

Responses of the active power of the upper- and lower-coils

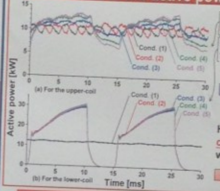

The upper-coil power was varied largely when the SCL_{upper} decreased.
Meanwhile, the active power for lower-coil was found that there were no difference in case of 0%SCL_{lower}

As decrease the value of SCL_{upper}, the maximum input power become higher, and, the minimum input power become lower.
Hence, temperature in the torch can increase during on-time, whereas it can decrease during off-time.

To increase modulation degree SCL_{upper}, *more efficient process is expected.*

SEM images of synthesized particles collected from the filter

These figures indicate that spherical nanoparticles were successfully fabricated using the tandem-MITP with current amplitude modulation.
These morphologies imply that the synthesized particles grew up in a vapor phase to have sphere shapes.

Particle size distribution (PSD)

Particle size distribution was evaluated by measuring 300 particles from SEM images.

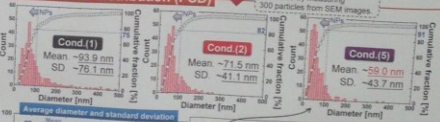

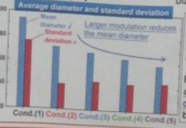

In case of cond. (5), a high yield ~91% for synthesized particles and a smaller diameter ~59 nm were obtained despite of no quenching gas condition.

From the PSDs estimated, *a high modulation degree of the upper-coil current was found to decrease the diameter of the synthesized particle* because the modulation offered high cooling-rate.

X-ray diffraction (XRD) analysis

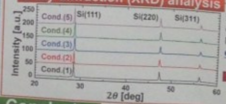

XRD results for synthesized particles indicate only Si peaks were observed for all conditions. Moreover, no strong peak was detected except Si crystalline peaks.

Si crystalline nanoparticles were found to be synthesized.

5. Discussion(*Temperature field from numerical simulation*)

A thermo-fluid field in a tandem-MITP was computed *without considering a powder injection.*

Numerical conditions were set to the same for the experiment.

- For cond. (1) and (2) simulation and comparison were done.
- Powder injection was neglected for simplicity.
- The power of only a lower-coil was modulated.

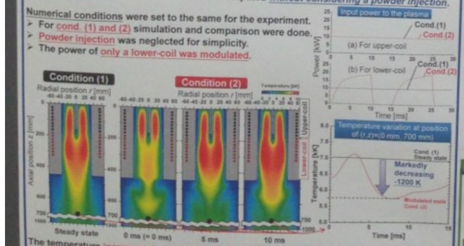

The temperature increases during the on-time, and decreases during the off-time effectively in the plasma torch and chamber.

The modulated plasma may provide completely evaporation during on-time and efficient cooling during off-time are expected.

It is found that a larger modulation of the tandem-MITP is effective for nanoparticles synthesis.

6. Conclusion

In this study, pure silicon nanoparticles were synthesized using tandem-MITP with 'simultaneous' modulation of a upper- and lower-coil currents.

1. The power variation of the modulation,
2. Morphologies and size distribution of the obtained particles
3. Compositions of the particles

were studied.

Result
1. Decreasing SCL_{upper} for upper-coil current raised a max. power and reduced a min. power.
2. Larger modulation with a 'simultaneous' modulation for both upper and lower-coil enhanced a yield of the fabricated particles.
3. Pure silicon nanoparticles were successfully obtained with ~70 g/h@20 kW even without quenching gas!

A 'simultaneous' modulation for both upper- and lower-coil currents provides a efficient nanoparticle synthesis.

Enhanced CO_2 Conversion by Atmospheric Pressure Microwave Plasma - Solar Processing

UMASS Lowell
University of Massachusetts Lowell

R·Eng Lab
Re-Engineered Energy Laboratory
University of Massachusetts Lowell

Sina Mohsenian, Dassou Nagassou, Saroj Bhatta, Rasool Elahi, Juan Pablo Trelles
Department of Mechanical Engineering, University of Massachusetts Lowell

Abstract

The conversion of CO_2 using renewable energy can help mitigate environmental emission and address global fuel needs. Solar thermochemical processes have the greatest sustainability potential, but are limited by the low reactivity of CO_2 and the intermittency of solar radiation. In contrast, plasma processes have the potential for high efficiency and continuous operation. The synergistic combination of microwave plasma and concentrated solar is investigated as a novel approach for greater viability CO_2 conversion.

1. Introduction

Solar Enhanced Microwave Plasma (SEMP)

- Microwave plasmas have potentially the highest energy efficiencies for molecular dissociation via effective step-wise vibrational excitation
- Solar thermochemical synthesis processes directly utilize the solar energy as a most abundant form of renewable energy.
- Solar enhanced microwave plasma (SEMP) is motivated by the potential for synergistic effects from the interaction between solar photons and plasma-generated species [1, 2]

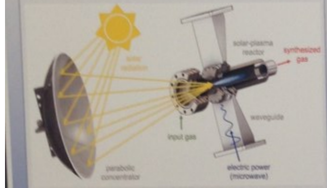

- Potential for synergism suggested by higher absorption of solar energy by CO_2 in non-Local Thermodynamic Equilibrium (NLTE) – potential for greater reactivity

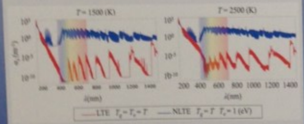

Absorption coefficient of CO_2 in LTE and NLTE computed with the SPARTAN code [3]

2. Reactor Design

SEMP reactor components

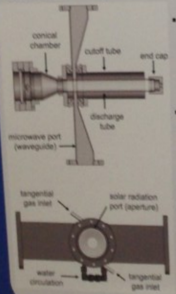

- Atmospheric pressure surface microwave in Transverse Electric (TE) mode
- Electromagnetic wave delivers power in the direction of propagation to the discharge tube
- Microwave power sustains a stable atmospheric pressure Ar-CO_2 plasma

Solar concentrator - SEMP reactor set-up

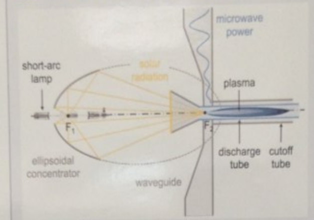

- High-flux solar simulator: 6.5 kW short-arc Xe lamp
- The center of the electric arc inside the short-arc lamp and the plasma generation point are located at the focal points F_1 and F_2, respectively

3. Experimental setup

SEMP reactor, Solar simulator, delivery and diagnostics systems

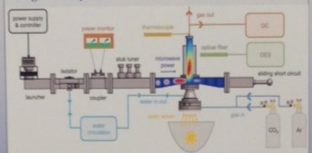

- Components: magnetron, waveguides, solar-plasma reactor, high-flux solar simulator, gas delivery system, water circulation, power monitoring, emission spectrometer, and gas chromatography

SEMP reactor under operation

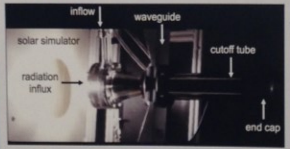

- Conical aperture – concentrated solar flux reception
- Vortex inflow – prevent deposition over aperture, enhanced stability of plasma
- Tapered waveguide – power concentration
- Cutoff tube – mitigate electromagnetic losses

Plasma emission spectra (off-solar characterization)

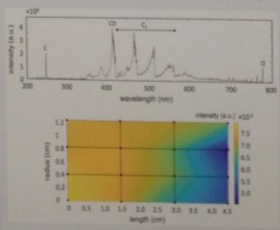

Atmospheric pressure operation with 100% CO_2 shows strong emission in the C_2 Swan bands - indicate of significant decomposition

4. Solar Radiation Absorption

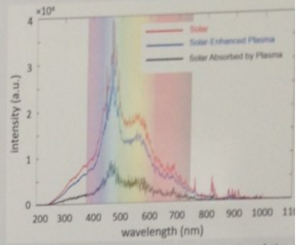

Lower intensity of solar radiation at the outlet of the reactor indicates the absorption by microwave plasma

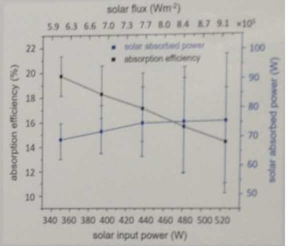

Higher absorption efficiency and less absorbed power for higher solar power input

5. CO_2 Decomposition

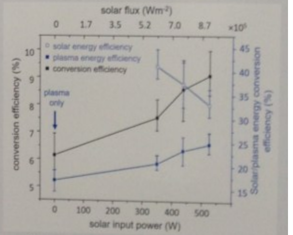

Higher conversion and plasma conversion energy efficiency of CO_2 for higher solar power input

6. Summary and Conclusions

- Enhancement of microwave plasma process by solar radiation: increased sustainability, efficiency and resiliency of chemical synthesis
- Absorption of up to 20% of incident concentrated solar radiation by the plasma at the lowest solar input power
- Conversion and plasma energy conversion efficiency increase with increasing solar power input, achieving up to 9% and 25%, respectively

Acknowledgements

Financial support provided by the U.S. National Science Foundation award CBET-1552037

References

[1] Mohsenian, S., Nagassou, D., Bhatta, S., Elahi, R., Trelles, J.P., 2019. Plasma Sources Science and Technology, 28, 065001

[2] Nagassou, D., Mohsenian, S., Bhatta, S., Elahi, R., Trelles, J.P., 2019. Solar Energy, 180, 678-689

[3] Lino da Silva, M., Lopez, B., Espinho S. (2013) SPARTAN 2.5

Max-Planck-Institut für Plasmaphysik

Investigation of an atmospheric pressure 2.45 GHz microwave CO_2 plasma source: comparison of pulsed and CW operation

F. A. D'Isa, E. Carbone, A. Hecimovic and U. Fantz

Max-Planck-Institut für Plasmaphysik, Boltzmannstr. 2, 85748 Gar

IPP

P1

Introduction

How to improve CO_2 conversion?

$$CO_2 + M \rightarrow CO + O \xrightarrow{+O} CO + \tfrac{1}{2} O_2 \quad (1) \qquad \text{Good: CO formation}$$

$$CO + O_{(2)} \xrightarrow{+M} CO_2 + M\,(+O) \quad (2) \qquad \text{Bad: CO loss}$$

Electron temperature, gas temperature, cooling rates and flow dynamics are believed to be the limiting processes to improve (1) and minimize (2).

→ Spectroscopic diagnostics used for probing T_{gas} and plasma emission volume.

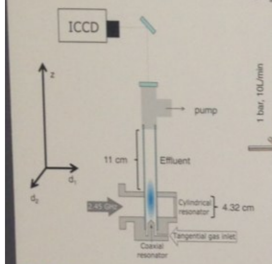

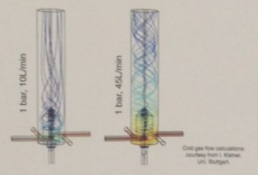

- Coaxial resonator used for plasma ignition directly at high pressure.
- Swirling flow stabilizes plasma in the center of the tube (26 mm inner diameter).

OES characterization of the plasma (T_{gas})

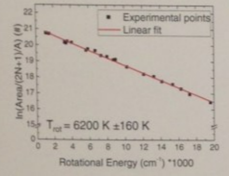

- Emission spectrum dominated by C_2 Swan Band $d^3\Pi_g \rightarrow a^3\Pi_u$.
- Rotational levels of $C_2(d^3\Pi_g)$ are Boltzmann distributed.
- Emission spectra fit with massiveOES [1] and line database [2] gives T_{rot} and T_{vib}.

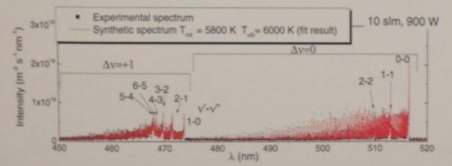

The rotational and vibrational levels of $C_2(d^3\Pi_g)$ are Boltzmann distributed within statistical errors. Rotational energy transfer rates of $C_2(d^3\Pi_g)$ are consistent with assumption that $T_{rot} \sim T_{gas}$.

Power deposition profile

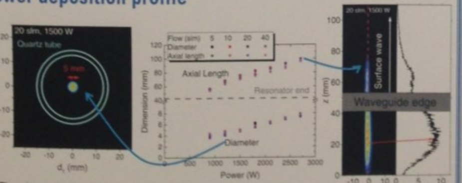

- The plasma region has been defined as the region where the light intensity is above 15% of the maximum intensity.
- Plasma extends in the effluent due to coupling of surface wave onto the plasma surface.

Cross section and axial length of plasma emission do not depend on CO_2 gas flow.

Thermal CO_2 conversion and flow dynamics

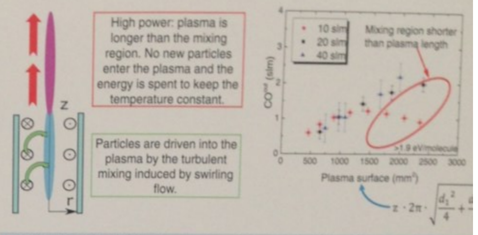

The influx of particles into the plasma region determines the CO out flux, that does not depe[nd] on the input flow (between 10 and 20 slm).

Does MW pulsing change something?

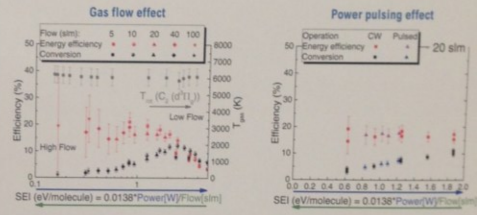

Conversion in pulsed operation is equivalent to the conversion in continuous mode (CW) with Power = duty cycle · Peak Power

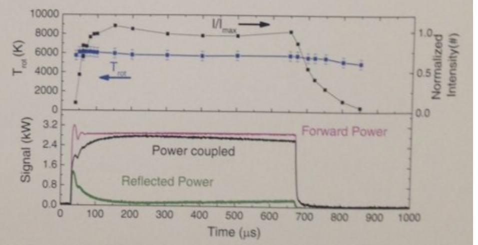

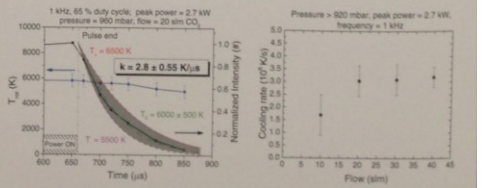

- Using a thermodynamic model (NASA-CEA code [3]) based on minimization of Gibbs free energy ($G(p,T) = H - TS$) → ***decay of C_2 state density*** can be described using the decay of T_{gas}.
- The cooling rate weakly depends on the CO_2 flow and saturates to a value of 3 K/µs for flow higher than 20 slm.

Conclusions and Outlook

- The CO_2 conversion is dominated by thermal conversion both in CW operation and in kHz pulsed plasma.
- The flow dynamic completely dominates the conversion of CO_2.
- The C_2 density behavior in the plasma afterglow can be described by temperature decay at thermal equilibrium.

[1] J. Voráč and P. Synek, "Batch processing of overlapping molecular spectra as a tool for spatio-temporal diagnostics of power modulated microwave plasma jet", Plasma Sources Science and Technology 2017, 26, 025010

[2] J. S. A. Brooke, "Line strengths and updated molecular constants for the C_2 Swan system", Journal of Quantitative Spectroscopy and Radiative Transfer 2013, 124, 11 - 20

[3] Gordon, Sanford and McBride, Bonnie J. Nasa reference publication, 1311 (1994).

Temperature determination in a MW plasma torch and on a deposition target by modelling and experiment

M Baeva[1,*], F Hempel[1], R-P Methling[1], R Foest[1], D Loffhagen[1], T Trautvetter[2], H Baierl[2]
[1]Leibniz Institute for Plasma Science and Technology (INP) / Felix-Hausdorff-Straße 2 / 17489 Greifswald, Germany
[2]Leibniz Institute of Photonic Technology / Albert-Einstein-Straße 9 / 07745 Jena, Germany
*baeva@inp-greifswald.de

MOTIVATION

A microwave (MW) plasma torch operated at atmospheric pressure at a frequency of 2.45 GHz is currently studied for multi-component doping of silica preforms.
The determination of the plasma parameters in the region of plasma-precursor interaction is of primary importance for the technological application since

- the plasma parameters in the plume depend on the conditions inside the plasma source
- the source is hardly accessible by diagnostics methods.

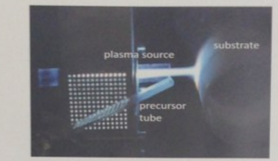

CONCLUSIONS AND OUTLOOK

The gas temperature was determined in the MW plasma source and in the plume by means of self-consistent modelling, emission spectroscopy and thermography.
Since gas temperatures are still not determined in oxygen-containing mixtures with the admixture of any precursor materials, future studies will be extended to such application-oriented plasmas. Additionally, the influence of the deposition target on the plasma and its temperatures will be investigated in more detail.

PHYSICAL BACKGROUND

Experimental arrangement

The plasma source consists of a standard waveguide R26 and a quartz tube traversing at the position of maximum electric field of the fundamental mode TE_{10}. Argon/oxygen mixtures are employed as working gas. The plasma jet is directed towards a rotating substrate

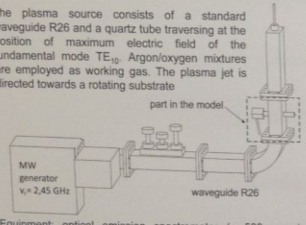

Equipment: optical emission spectrometer (a 500 mm imaging spectrograph SP-2556 by Roper Acton is combined with an intensified CCD camera PI-MAX4:1024i-RB by Princeton Instruments); thermographic camera VarioCAM by InfraTec.

Operation conditions

pressure: $1.01 \cdot 10^5$ Pa
working gas: Ar/O_2 – mixtures, flow rate 10-20 slm
frequency: 2.45 GHz,
power: 1-2 kW in continuous operation,
tube: made of quartz, inner radius 6.1 mm,
tube length outside the resonator: L_{out}=15-38 mm,
distance from the tube end to the target: 20-50 mm

Self-consistent modelling approach

The model is based on a hydrodynamic approach. Its equations describe self-consistently the gas flow, the plasma kinetics, the heat transfer, and the microwave field in the waveguide [1].

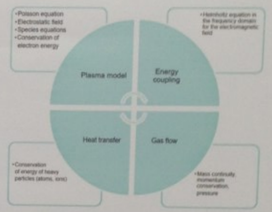

Example of measured and calculated OH-spectra in the argon jet without substrate

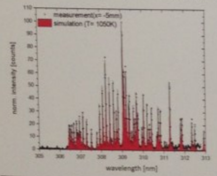

Thermography at the place of deposition

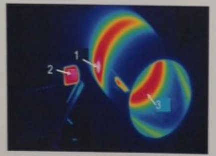

Schematics of the MW plasma source

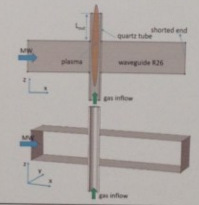

Energy and reaction scheme

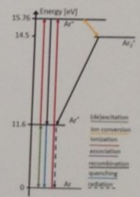

EXPERIMENTAL AND MODELLING RESULTS

Two-dimensional distribution of the gas temperature in the plasma source and in the plume (incident power 1 kW, flow rate 8 slm.

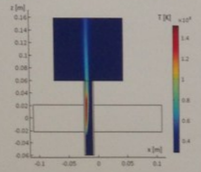

Computed gas temperature along a line-out 2.5 mm away from the tube wall (lines) and experimental results (symbols). The position of the tube end is zero. (1 kW, L_{out}= 38 mm).

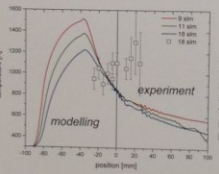

Gas temperature in Ar/O_2 mixtures along the gas flow (1kW, 18slm, L_{out}=38 mm).

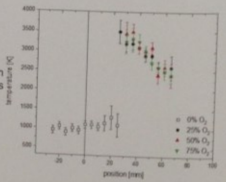

modelling

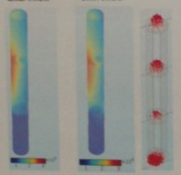

Temperature in [K] in the plasma source from 3D modelling with axial and swirling inflow.

experiment

Gas temperature for different tube diameters (1kW, 18slm, L_{out}=38 mm).

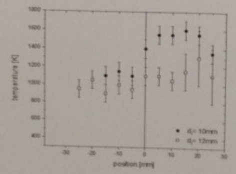

experiment

Surface temperature of the substrate for mixtures of 10 slm O_2 and Ar from the precursor tube (power 1 kW).

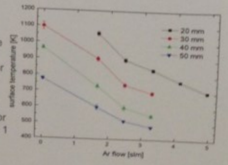

References:
[1] M Baeva, F Hempel, H Bairl, T Trautvetter, R Foest, D Loffhagen, J Phys D: Appl Phys 51 (2018) 385202

Acknowledgments
This work was supported by the Leibniz-Gemeinschaft: SAW-2017-IPHT-1.
The technical support by Daniel Köpp is greatly acknowledged.

Leibniz Association

INSTITUTO TECNOLÓGICO DA AERONÁUTICA
SÃO PAULO RESEARCH FOUNDATION

Measurements of OH in atmospheric pressure argon microwave plasmas

J. Amorim and M. A. Ridenti
Departamento de Física, Instituto Tecnológico de Aeronáutica, 12228-900, S.J. Campos, Brazil

Abstract: Hydroxyl radical is measured as function of distance, flux and microwave power in atmospheric pressure argon microwave plasma expanding in air. Employing mass spectrometry and optical emission spectroscopy the plasma jet was characterized and the conditions for maximum production of OH were determined. The kinetics of OH was discussed and its relationship with other radicals like as H_2O_2, H_2O, H_3O and NO, was addressed.

1. Introduction

In this work the production and loss channels of OH in an atmospheric pressure plasma jet generated by a Surfatron launcher expanding in air was studied. A microwave power generator of 2.45GHz was employed to feed a Surfatron surface-wave launcher. The power was varied between 30W and 100W, flux of 2.5 SLM and 5.0 SLM and the gas used to produce the discharges was argon. Employing mass spectrometry measurements, the main neutral and positive ions along the jet are measured as function of operating parameters of the plasma. Axial variation of plasma parameters n_e, T_e, and T_g in was measured by optical emission spectroscopy (OES).

2. Experimental apparatus

The experimental set-up used for OES diagnostics was detailed in a previous publication [1]. As shown in figure 1, the experimental apparatus includes the plasma source, the mass spectrometer and data acquisition system for measurements.

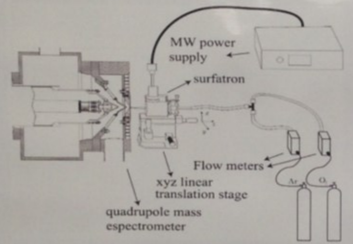

Figure 1. Arrangement employed in mass-spectrometer diagnostics.

3. Results

The understanding of the kinetics of the intermediate short-lived radical OH and the stable H_2O_2 depends not only on the knowledge of other species such as H_2O, but also on the subsequent chain and end reactions.

Figure 2 shows the density of OH, H_2O, H_2O_2, H_3O and NO as function of distance when the plasma is excited by 100W of microwave power. The OH intensity initially decreases after Surfatron exit until a minimum at 2.5 mm growing after to a maximum at ~11 mm corresponding the maximum density of electrons. As n_e maximum is at ~11 mm, electron-ion recombination should be the most important mechanism for OH production in this region, while at the Surfatron exit the electric power density is high and electron dissociation may also be an important reaction for production of hydroxyl radical.

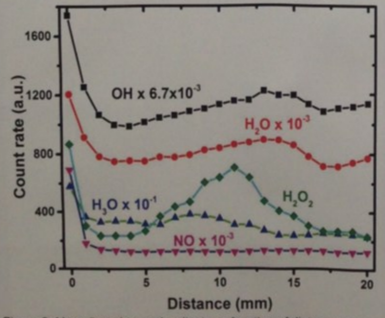

Figure 2. Mass flux of neutral radicals as function of distance; microwave power of 100 W and flux of 5.0 SLM. OH(filled square),H_2O (filled circle), H_2O_2(filled diamond), H_3O(up filled triangle) and NO(down filled triangle).

In figure 3 it can be seen that maximum of OH count rate for power of 100 W occurs at 5 mm from the Surfatron exit while for 150 W the intensity continuous grows until distance of 10 mm after which a small decrease is observed.

In figure 4 the flux was varied from 2.5 to 7.5 SLM. As the flux increases the maximum intensity of the OH moved to higher distances. This occurs because the point of turbulence development gets closer to the jet nozzle as the flux increases favoring the injection of the H_2O into the plasma.

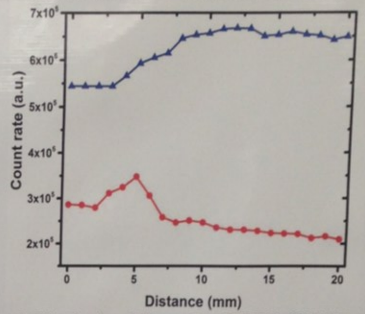

Figure 3. OH as function of distance; flux of 2.5 SLM, 100 W (filled circle) and 150 W (up filled triangle).

This effect improves the mixing of ambient air particles with the effluent plasma jet in the region near the nozzle forming H_2O^+ and H_3O^+ ions but the position of maximum electron density gets closer to the plasma tip as the flow increases. The resulting net balance of ionization and dissociative electron attachment is the profile presented in figure 4.

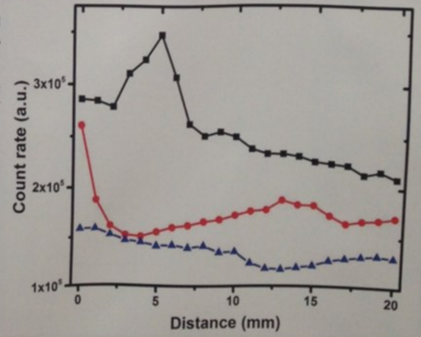

Figure 4. OH as function of distance; power of 100 W and flux of 2.5 SLM (filled square), 5.0 SLM (filled circle) and 7.5 SLM (up filled triangle).

4. Conclusion

It was shown that hydroxyl radical mass flux intensity initially decreases after Surfatron exit until a minimum at 3 mm growing after to a maximum at ~11 mm corresponding the maximum density of electrons. OH intensity tends to increase like the electron density and gas temperature, in the range of powers and fluxes investigated. Electron-ion recombination is the most important mechanism for OH production in this region.

References

[1] M. A. Ridenti, J. A. Souza-Corrêa and J. Amorim, J. Phys. D: Appl. Phys. 47 045204 (2014).

Physical study of a microwave plasma source for agricultural applications

A. Kais, T. Maho, L. Thérèse and Ph. Guillot

Laboratoire Diagnostics des Plasmas Hors Equilibre (DPHE)
Université de Toulouse, INU Champollion, Albi, France

Institut National Universitaire Champollion

Introduction

Low pressure and low temperature plasma is a non-thermal technology. The absence of toxics components and the large volume treatment capacity provide a good alternative to the conventional spices decontamination methods [1].

The process optimisation requires an excellent understanding and control of plasma characteristics. This includes the fundamentals plasma parameters (n_e, T_e, FDEE...), the type of created species (photons, reactive species...), the gas temperature, the substrate influence on the plasma for example.

In this work, the plasma chemistry has been investigated by optical emission spectroscopy. Probes measurements have been performed first, to study the plasma parameters in several sustained conditions, and next, to understand the heating process of the substrate by the ionized gas.

Experimental set-up

Set-up :

- Chamber volume : 40 L
- Gas : Ar, Ar-O_2 (2%), Air
- Source : Hi-Wave 2,45GHz (SAIREM [2])
- Microwave power supply : 1 < P_{MW} < 200 W
- Pressure : 10 < p < 60 Pa
- Radial axis : 0 < r < 18 cm
- Axial axis : Z = 3.5, 5.5, 8.5 cm

Plasma diagnosis :

- Optical Emission Spectroscopy (OES)
- Boltzmann Plot (BP)
- Langmuir Probe (LP)
- MicroWave Interferometry (MWI)

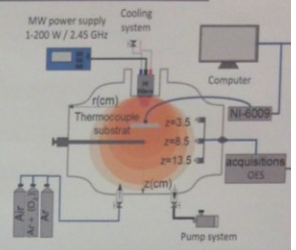

Determination of T_e by the Boltzmann Plot Method and Langmuir Probe

Boltzmann Plot (BP): Calculation of T_e by inverting the slope of the following logarithmic functions :

$$\ln\left(\frac{\lambda_{ij} I_{ij} \sum_{i>j} A_{ij}}{hc a_i A_{ij}}\right) = \frac{-E_i}{k_B T_e} + D$$

Requirements:

- Assuming the Corona model described by Fujimoto [3].
- Argon plasma characterization by Optical Emission Spectroscopy : λ_{ij} and I_{ij}. In our study λ_{ij} = 751.46 ; 750.38 ; 731.60 ; 731.17 ; 714.70 ; 706.87 ; 687.95 and 516.22 nm.
- Literature data (NIST or [4]) : A_{ij}, h, c, a_i, E_i and k_B.

Plasma conditions :

- Gas : argon
- Microwave power : 150 W
- Pressure : 15 Pa

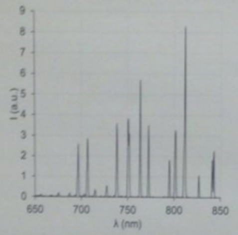

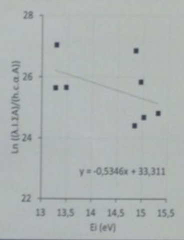

Langmuir probe (LP): Calculation of T_e from the I(V) curve measured with the probe at Z = 8.5 cm.

Plasma conditions :

- Gas : argon
- Microwave power : 150 W
- Pressure : 15 Pa

Diagnostics	T_e (eV)
Boltzmann plot	1,9 ± 0,5
Langmuir probe	1,4 ± 0,3

Determination of n_e by Langmuir Probe and MicroWave Interferometry

MicroWave Interferometry (MWI) : Determination of n_e from the microwave beam phase shift crossing the plasma area [5].

$$\langle n_e \rangle = \frac{n_c \lambda_0}{\pi L} |\Delta\varphi|$$

Requirements:

- Large reactor windows to avoid microwave reflexion (> 5 cm).
- Plasma length (> 6 cm).
- Homogeneous plasma.

Differences with Langmuir probe (LP) :

- Non-invasive diagnostic.
- Suitable for etching or depositing plasma applications.
- Give the average electron density in the line of sight.

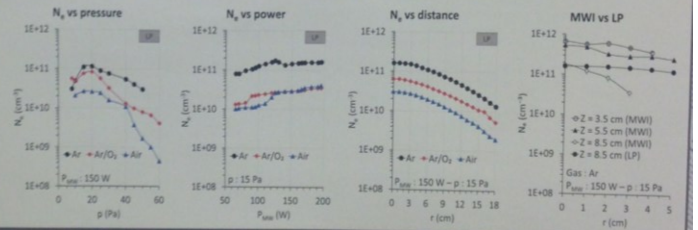

Substrate temperature measurements

P_{se} is the microwave power quantity transfered to the substrate.
Two methods have been used to calculate P_{se}:

A. By deducing P_{se} from temperature measurement
A.1. Establish the balance power provided by the generator.
A.2. Measure the substrat temperature variation in the plasma ON/OFF phase using a type K thermocouple.
A.3. Resolve the following equation :

$$P_{se} = P_s + P_{port} = C_s\left(\frac{dT_R}{dt} - \frac{dT_C}{dt}\right)_{T_{Mean}} \;[W]$$

B. By calculating P_{PLASMA}

$$P_{se} = P_{PLASMA} = P_e + P_i + P_{recomb}$$

Details are given in [4] and [6].

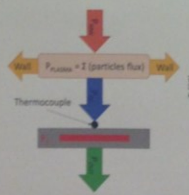

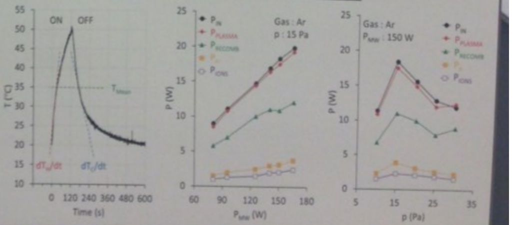

Conclusion

1.5 < T_e (eV) < 2.0 : Boltzmann plot method can be an alternative to Langmuir probe measurement but high resolution spectrometer is strongly recommended to minimize optical data deviation.

5.10^{10} < N_e (cm^{-3}) < 2.10^{11} : Microwave interferometry is complementary to probe measurement. It can reach plasma zone inaccessible to Langmuir probe.

P_{se} = 12% of P_{MW} at Z = 8.5 cm : Both methods show a good correlation. Others experiments would be done closer to the source.

References and acknowledgements

[1] B. A. Niemira, Annual review of food science and technology, **3** (2012).
[2] L. Latrasse, Journal of microwave power and electromagnetic energy, **51**, 4 (2017).
[3] T. Fujimoto, Journal of the physical society of Japan, **54**, 8 (1985).
[4] A. Kais, Physics of plasmas, **25**, 013504 (2018).
[5] T. Gries, Journal of vacuum science and technology B, **27**, 5 (2009).
[6] R. Piejak, Plasma sources science and technology, **7**, 4 (1999).